SISSA **ISAS**

SCUOLA INTERNAZIONALE SUPERIORE DI STUDI AVANZATI
INTERNATIONAL SCHOOL FOR ADVANCED STUDIES

Non-linear structure formation and cosmic radiation backgrounds

Thesis submitted for the degree of
Doctor Philosophiæ

CANDIDATE
Carmelita Carbone

SUPERVISORS
Prof. Carlo Baccigalupi
Prof. Sabino Matarrese

October 2007

To Gianfranco and my beloved family
who give so much energy to my life!

Contents

Published Papers

- **Papers on refereed journals:**
  - **C. Carbone**, and S. Matarrese, "Unified treatment of cosmological perturbations from super-horizon to small scales", Phys. Rev. D71 (2005) 043508
  - **C. Carbone**, C. Baccigalupi and S. Matarrese, "Stochastic gravitational wave background from cold dark matter halos", Phys. Rev. D73 (2006) 063503
- **Proceedings:**
  - **C. Carbone**, C. Baccigalupi and S. Matarrese, "The stochastic gravitational-wave background from cold dark matter halos", proceedings of the International Astrophysics Conference "Relativistic Astrophysics and Cosmology - Einstein's Legacy -", eds. B. Aschenbach, V. Burwitz, G. Hasinger, and B. Leibundgut, Springer-Verlag series "ESO Astrophysics Symposia", 2006

Introduction

Modern cosmology begins with Einstein's 1917 paper where he applies his General Relativity (GR) Theory to Cosmology.
After that day many discoveries have been performed and many successes in the theoretical knowledge have been achieved.

Nowadays, the opinion of many physicists is that the Universe is well-described by what Fred Hoyle termed a Big Bang Model, according to which the Universe expanded from a denser hotter stage to its current state, where the present energy budget is dominated for $\sim 76\%$ the by dark energy and for $\sim 20\%$ by dark matter (neither of which have never been detected in the laboratory), while the stuff which biological systems, planets, stars, and all visible matter are made of (the remaining 4% in baryons) represents a very small tracer on this dark sea, with the electromagnetic radiation being an even less significant contribution.

Observations indicate that the initial inhomogeneities, which have evolved generating the observed structures in the Universe, are more or less scale invariant, and that the simplest best-fitting Big Bang Model has a flat spatial geometry. These facts could be the consequence of a simple Inflationary Era of the Universe, a very early period of extremely rapid expansion, which stretched zero-point quantum-mechanical fluctuations to larger length scales and converted them into the needed classical inhomogeneities in the mass-energy distribution.

Given these initial inhomogeneities at an earlier time, the expansion of the Universe, the gravitational instability, the pressure gradients, and the microphysical processes give rise to the observed anisotropies in the Cosmic Microwave Background (CMB) and

to the current large-scale distribution of non-relativistic matter, such as galaxies, groups and clusters, which are locally distributed inhomogeneously in space, although, in a statistical sense and on large enough scales, their distribution approaches the isotropy. More specifically, in the early Universe, nuclear physics reactions between protons, neutrons, etc., resulted in the nucleosynthesis of the lighter elements (baryons), while the total temperature was decreasing with the expansion. As the temperature dropped down below $T \sim 3000$ K, neutral hydrogen atoms started to form via the "recombination process". The finite time required for the recombination resulted in a time-interval of non-zero thickness (the Last Scattering (LS) Surface) within which the decoupling of neutral baryons and photons occurred. The mean-free path grew so much to allow photons to travel almost freely and to form the today observed CMB. Indeed, just like a snapshot of the early Universe, the CMB carries the trace of cosmological perturbations at last scattering, in the form of anisotropies, both in total intensity and linear polarization, resulting from Thomson scattering of photons into electrons.

However, measurements of the CMB anisotropy indicate that fluctuations in the baryons at decoupling were too small to have grown alone via gravitational instability into the structures seen today in the galaxy distribution.

A solution to this puzzle is provided by the Cold Dark Matter (CDM), of the same type and quantity needed to explain gravitational interactions on galactic and cluster scales. Including this non/weakly interacting component with low primeval velocity dispersion, the Universe becomes matter dominated at a redshift comparable to, or even larger than, the LS redshift, and the low observed CMB anisotropy is reconciled with the observed large-scale structure. Consequently, measurements of the CMB anisotropy probe the CDM distribution and are an independent argument for its existence.

At the present, observations of type Ia supernovae, probing of the cosmic expansion history, give strong evidence that the Universe has recently started a period of accelerated expansion. In order to explain this phenomenon, the cosmologist community has introduced the concept of "dark energy" (DE) which was sub-dominant until recently, when it started slowing the rate of structure growth. The simplest interpretation in terms of a cosmological constant caused revival of the "cosmological constant problem", *i.e.* why the corresponding vacuum energy assumed to be of fundamental origin, is about 123 orders of magnitude less than the Planck scale. More specifically, the interpretation of the dark energy as a simple cosmological constant gives rise to a "fine–tuning" and "coincidence problem". The fine–tuning is required in the early Universe

to store a tiny fraction of energy in the vacuum, compared to the total one. The coincidence simply asks why that tiny fraction is such to be comparable to the matter one at the present epoch. The concept of dark energy generalizes the cosmological constant with a component which is generally dynamic and fluctuating in the attempt to alleviate the two problems mentioned above. In this field, progress in cosmology is likely to come from more and higher-quality observational and simulation data. A number of ground-based, space-based, and numerical experiments continue to collect data and new near-future particle physics, cosmology, astronomy, and numerical experiments are in project.

The several and different observations, concerning the CMB anisotropy and polarization, the large scale structure distribution, the baryon abundance, the late accelerated expansion, etc., suggest what is today called the "Concordance Cosmological Model", in the sense that there is quite a converging view of the numbers that form the Universe matter-energy content and the distribution of its perturbations. On this side, cosmology has now become a precision science, but unfortunately it is often limited by the sensitivity of the instruments and lacks, in some cases, a theoretical interpretation of experimental measurements.
For instance, there is not yet any proved explanation of what dark matter and dark energy are. Moreover, although the inflation era is by now quite commonly accepted by the scientific community, there is still the necessity of characterize its mechanism in detail.
The most promising method for observationally probing this early inflationary epoch is through the detection of primordial gravity waves (GW) predicted in a number of inflation models. Indeed, this detection (via, *e.g.*, CMB polarization measurements), would constrain different inflationary models, but the non-detection would not rule out inflation. On the other hand, there exist several phenomena which could generate effects similar and comparable to primordial GW ones.
Among these, there are secondary effects in the CMB polarization due to the lensing of CMB photons by matter structures, which in turn, being characterized by a non-linear evolution, may generate second order signals in competition with the primordial ones. However, these phenomena are important by their own, since they yeld information on the distribution and evolution of cosmic structures.

Indeed, my PhD project has been devoted to a systematic and detailed analysis of some of the most important secondary contributions focusing on the effects from

non-linear structure formation.

In the first chapter of this thesis I briefly sketch a picture of our current understanding of the Universe and describe the main features of the Concordance Cosmological Model.

In Chapter 2, I describe different perturbative approaches adopted for the solution of the Einstein equations in the case of matter sources only, focusing on what we call a "hybrid" formalism for the description of their non-linear evolution. Moreover, via the formulas obtained with the hybrid approximation, I estimate the stochastic GW background generated by the strongly non-linear evolution of CDM structures (modeled as collapsing ellipsoids), which has to be distinguished by other cosmological GW backgrounds.

Chapter 3 is dedicated to the description of the CMB, together with its primary and secondary anisotropies in temperature and polarization.

In Chapter 4, I describe the physics of the gravitational lensing by large scale structures, focusing on its effects on the CMB.

Chapter 5 is devoted to the project of carrying on all-sky simulated lensed CMB maps via the use of N-body simulations in order to include and evaluate the effect on the non-linear structure evolution on CMB anisotropy and polarization. In particular, we build up maps of the projected lensing potential and deflection angle, exploiting the evolving dark-matter distribution of the Millennium Simulation. In this Chapter the first results of this project are presented.

Finally, in the Conclusions, I briefly summarize the main results of my PhD work and discuss the future directions of my research.

Chapter 1

The Einstein's Equations and the Concordance Cosmological Model

When Einstein applied his GR theory to cosmology [1], he assumed that the Universe was spatially homogeneous and isotropic and this was formulated as the "Copernican" cosmological principle by Milne in 1933. Knowing that the stars in the Milky Way move rather slowly, Einstein decided, as everyone had done before him, that the Universe should not evolve in time. As we know, he came up with a static (unstable) solution of his equations by introducing a new form of energy, now called the cosmological constant.
Unbound by the desire to have a static Universe, in '22-'24 Friedmann found instead the evolving homogeneous solutions of the Einstein's equations, while, at the end of 1920's, Robertson initiated the study of metric tensors of spatially homogeneous and isotropic space-times, and in the mid 1930's, together with Walker, obtained the so-called "Robertson-Walker" form of the metric tensor for homogeneous world models.
In 1929, after a decade of observations, Edwin Hubble and Milton Humason formulated their law that galaxies move away with a velocity proportional to their distance from the observer. This was the first observational evidence in support of the expanding space paradigm and the Big Bang theory.

1.1 The Friedmann-Robertson-Walker metric

At the zero-order of approximation, on large scales and for fundamentals observers (the so-called *comoving observers*) defined to be at rest with respect to the expansion/contraction of the spatial geometry, the Universe results to be *spatially homogeneous*

and isotropic.

As anticipated, this statement represents the Copernican Cosmological Principle, philosophically formulated by Milne and pursued by Bondi, Hoyle and Gold.

Although primarily on scales $\leq$ 100 Mpc matter is systematically distributed in clumps and voids, this principle is generally accepted since the CMB observations, the Hubble-law, the counts of Radio Galaxies, and other experimental evidences give it an empirical validity.

The GR theory describes space-time as a four-dimensional variety whose *metric tensor* g_{ij} is considered as a dynamical field. The dynamics of the metric is governed by the Einstein's field equations:

$$G^i{}_j = \kappa^2 T^i{}_j \,, \tag{1.1}$$

(where $\kappa^2 = 8\pi G/c^4$) which relate the Einstein tensor $G^i{}_j$ to the stress-energy tensor $T^i{}_j$ of the space-time contents. Here Latin indices run over $0 \ldots 3$ and Greek indices run over the spatial indices $1 \ldots 3$ only.

The solutions to Eq.(1.1) which admit a sub-space with constant *spatial* curvature are called "maximally symmetric solutions", since they are characterized by a number $n(n+1)/2$ of isometries, represented, in our 3D-space ($n = 3$), by 3 spatial translations and 3 spatial rotations, *i.e.* a 3D-space maximally symmetric is homogeneous and isotropic.

Such kind of solutions therefore can well describe our Universe constrained by the cosmological principle.

Fixing the comoving spatial network of observers, we have the freedom to associate a particular time-coordinate to them: in the so-called *synchronous gauge*, characterized by $g_{00} = 1$, all the observers can synchronize their clocks with respect to the *cosmic time* since it coincides with the proper time as measured in the locally inertial frame of each observer.

Under these assumptions, a metric, describing a four-dimensional space-time with a three-dimensional sub-space of constant curvature, can be written:

$$ds^2 = -c^2\, dt^2 + a^2(t)\, dl^2 \,, \tag{1.2}$$

where dl is the line element of the homogeneous and isotropic 3D-space and $a(t)$ is the *scale factor* describing the actual expansion.
The spatial hypersurfaces whose geometry is described by dl^2 can either be a 3D-sphere, a 3D-hyperboloid or a 3D-plain.

Introducing polar coordinates, Eq. (1.2) can be written in the form of the Friedmann-Robertson-Walker (FRW) metric:

$$\begin{aligned} ds^2 &= -c^2\,dt^2 + a^2(t)\,d\mathbf{x}^2 \\ &\equiv -c^2\,dt^2 + a^2(t)\left[\frac{dr^2}{1-Kr^2} + r^2\left(\,d\vartheta^2 + sin^2\vartheta\,d\varphi^2\right)\right] \\ &\equiv -c^2\,dt^2 + a^2(t)\left[\,d\chi^2 + r^2(\chi)\,d\Omega^2\right]\,, \end{aligned} \tag{1.3}$$

where the radial function $r(\chi)$ is either a trigonometric, hyperbolic or linear function of χ, depending on whether the curvature K is positive, negative, or zero. Specifically:

$$r(\chi) = \begin{cases} K^{-1/2}\sin(K^{1/2}\chi) & (K>0) \\ \chi & (K=0) \\ (-K)^{-1/2}\sinh[(-K)^{1/2}\chi] & (K<0) \end{cases}\,. \tag{1.4}$$

Sometime, expecially when the Universe is spatially flat, it is useful to introduce a different time-coordinate, the so-called *conformal-time*: $\eta = \int_0^t dt'/a(t')$.
In the conformal gauge the FRW metric takes the form:

$$ds^2 = a^2(\eta)\left\{-c^2\,d\eta^2 + \left[\frac{dr^2}{1-Kr^2} + r^2\left(\,d\vartheta^2 + sin^2\vartheta\,d\varphi^2\right)\right]\right\}\,, \tag{1.5}$$

and, if $K=0$, it is called conformally flat.

Due to the highly symmetric form of the metric given by Eq. (1.3), the Einstein field equations imply that T_{ij} has to be the stress-energy tensor of a homogeneous perfect fluid, *i.e.* diagonal and characterized by its density $\rho(t) = \sum_i \rho_i(t)$ and its pressure $p(t) = \sum_i p_i(t)$, where each i-component is supposed to be non-interacting with the other species. The field equations then reduce to the two independent equations:

$$\left(\frac{\dot{a}}{a}\right)^2 = \frac{8\pi G}{3}\rho - \frac{Kc^2}{a^2} + \frac{\Lambda}{3}\,, \tag{1.6}$$

and

$$\frac{\ddot{a}}{a} = -\frac{4}{3}\pi G\left(\rho + \frac{3p}{c^2}\right) + \frac{\Lambda}{3}\,, \tag{1.7}$$

which represent the Friedmann and Rayachaudhuri equations, respectively, and the presence of the cosmological constant Λ has been made explicit. The scale factor $a(t)$ is determined once its value at one instant of time is fixed. We choose $a=1$ at the present epoch t_0.

Finally, Eqs. (1.6)-(1.7) can be combined to yield the *adiabatic equation*:

$$\frac{d}{dt}\left[a^3(t)\rho(t)c^2\right] + p(t)\frac{da^3(t)}{dt} = 0\,, \tag{1.8}$$

which has an intuitive interpretation: the change in the 'internal' energy of a volume element equals the pressure times the change in proper volume, *i.e.* it is the first law of thermodynamics in the cosmological context.

1.2 Properties of the Universe

The quantity $\dot{a}/a$ is crucial for the determination of the expansion rate of the Universe and is called the Hubble parameter $H(t)$; its value at the present epoch $t = t_0$ is the *Hubble constant* $H(t_0) \equiv H_0$ which has the dimension of an inverse time. The uncertainty in H_0 is commonly expressed as $H_0 = 100\,h\,\mathrm{km\ s^{-1}\ Mpc^{-1}}$, hence

$$H_0 \approx 3.2 \times 10^{-18}\,h\,\mathrm{s^{-1}} \approx 1.0 \times 10^{-10}\,h\,\mathrm{yr^{-1}}\,. \tag{1.9}$$

The time scale for the expansion of the Universe is simply the inverse of the Hubble constant, or $H_0^{-1} \approx 10^{10}\,h^{-1}$ years.

If we define the *critical density* $\rho_{cr} \equiv 3H^2/(8\pi G\rho) \approx 1.9 \times 10^{-29} h^2 g cm^{-3}$ as the density needed for the Universe to be exactly flat, and the density parameter for each component of the Universe $\Omega_i(t) \equiv \rho_i(t)/\rho_{cr}$, the Friedmann Eq. (1.6) can be rewritten as:

$$1 = \sum_i \Omega_i - \frac{K}{a^2H^2}\,, \tag{1.10}$$

where the last term is defined as the curvature density parameter $\Omega_K(t) \equiv -K/(a^2H^2) \equiv \Omega_{K,0}/a^2$. By definition $\Omega_\Lambda \equiv \Lambda/(3H_0^2)$ and the present total density parameter of the Universe is therefore $\Omega_0 \equiv \sum_i \Omega_{i,0}$.

The present state of the homogeneous Universe is specified by the present values of all the density parameters $\Omega_{i,0}$ and the present Hubble parameter h.

With these parameters the Eq. (1.10) takes the form:

$$H^2(t) = H_0^2\left[(1+z)^4\Omega_{r,0} + (1+z)^3\Omega_{m,0} + (1+z)^2\Omega_{K,0} + \Omega_\Lambda\right]\,, \tag{1.11}$$

where the subscripts r and m stand for radiation and matter respectively. Another fundamental quantity is the so-called *deceleration parameter* q_0 defined at $t = t_0$ by

$$q_0 = -\frac{\ddot{a}a}{\dot{a}^2}\,. \tag{1.12}$$

Due to the expansion of space, photons are redshifted while they propagate from the source to the observer. In fact, let us consider a comoving source emitting a light signal at t_e which reaches a comoving observer at the coordinate origin $r = 0$ at time t_0. Since $ds = 0$, a light geodesics propagates according to $|c\,dt| = (a dr)/(1 - Kr^2)^{1/2}$, and after integration the comoving distance of the source results to be:

$$\chi(r) = \int_0^r \frac{dr'}{(1 - Kr'^2)^{1/2}} = \int_{t_e}^{t_0} \frac{c\,dt}{a(t)} = \text{constant in time} \,, \tag{1.13}$$

from which follows:

$$\frac{dt_0}{dt_e} = \frac{a(t_0)}{a(t_e)} \,. \tag{1.14}$$

But, if ν and λ are respectively the frequency and wavelength of the source light, we can write:

$$\frac{dt_0}{dt_e} = \frac{\nu_e}{\nu_0} = \frac{\lambda_0}{\lambda_e} \,. \tag{1.15}$$

and finally, introducing the *redshift* z, defined as the relative change in wavelength or $1 + z = \lambda_0/\lambda_e$, Eqs. (1.14)-(1.15) lead to:

$$1 + z = \frac{a(t_0)}{a(t_e)} \,. \tag{1.16}$$

This shows that light is redshifted by the amount by which the Universe has expanded between emission and observation.

For a complete description of the expansion of the Universe, we need an equation of state for each non-interacting component of the Universe, $p = wc^2\rho$, relating the pressure to the energy density. Ordinary matter, which is frequently called *dust*, has $p \ll \rho c^2$, while $p = \rho c^2/3$ for radiation or other forms of relativistic matter, assumed at thermal equilibrium. Inserting these expressions into Eq. (1.8) gives

$$\rho(t) = a^{-n}(t)\,\rho_0 \,, \tag{1.17}$$

with

$$n = \begin{cases} 3 & \text{for dust: } p = 0 \\ 4 & \text{for relativistic matter: } p = \rho\, c^2/3 \end{cases} \,. \tag{1.18}$$

The energy density of relativistic matter (photons and neutrinos being the two obvious candidates) therefore drops more rapidly with time than that of ordinary matter.

1.3 The Concordance Cosmological Model

In the last decade rapid advances in observational cosmology have leaded to the establishment of the first precision cosmological model. According to this model galaxies and large-scale structures have grown gravitationally from tiny, nearly scale-invariant (as we specify later) adiabatic[1] Gaussian[2] fluctuations in a Universe spatially flat, homogeneous and isotropic on large scales, composed of radiation, ordinary matter (electrons, protons, neutrons and neutrinos), non-baryonic CDM[3], and dark energy, described in the Introduction.

This model of the Universe includes as well a statistical description of the deviations from homogeneity, which we formalize in the next chapter, giving here only the most important and intuitive details.In order to describe these perturbations, it is usually introduced the dimensionless quantity $\Delta^2(k) = k^3P(k)/(2\pi^2)$ where $P(k)$ is the power spectrum of the density fluctuations and k the Fourier wavenumber; if the perturbations obey the Gaussian statistics, the power spectrum provides a complete description of their properties: if $\delta(\mathbf{k})$ represents the Fourier transform of the density fluctuations at wavevector $\mathbf{k}$, Gaussianity means that $< \delta(\mathbf{k})\delta(\mathbf{k}') > \equiv (2\pi)^3P(k)\delta^3(\mathbf{k}-\mathbf{k}')$. Of particular interest is the Harrison–Zel'dovich or scale-invariant spectrum, which corresponds to a constant spectrum Δ^2, at the time in which a particular scale k crosses the Hubble horizon: $a/k = cH^{-1}$. More generally, one can approximate the spectrum by a power-law, writing $\Delta^2(k) = \Delta^2(k_*)(k/k_*)^{n_s-1}$, at horizon crossing, where n_s is known as the *scalar spectral index*, always defined so that $n_s = 1$ for the Harrison–Zel'dovich spectrum, and k_* is an arbitrarily chosen scale. The initial spectrum, defined at some early epoch of the Universe's history, is usually taken to have a simple form such as this power-law, while the subsequent fluctuations evolution modifies it.

As already mentioned, the simplest viable mechanism for generating the observed perturbations is the inflation, a period of accelerated expansion in the Universe's early

[1] Adiabaticity means that all types of material in the Universe share a common perturbation, so that if the space-time is foliated by constant-density hypersurfaces, then all fluids and fields are homogeneous on those slices, with the perturbations completely described by the variation of the spatial curvature of the slices.

[2] Gaussianity means that the initial perturbations obey Gaussian statistics, with the amplitudes of waves of different wavenumbers being randomly drawn from a Gaussian distribution of width given by the power spectrum. On the contrary, gravitational instability generates non-Gaussianity.

[3] CDM is made by massive particles, constituting the dark haloes around galaxies, and is characterized by negligible pressure with respect to the mass energy density

stages (*e.g.*[2, 3]). Inflation generates perturbations through the amplification of quantum fluctuations, which are stretched to astrophysical scales by the rapid expansion. The simplest models of inflation generate two types of fluctuations, density perturbations which come from fluctuations in the scalar field and its corresponding scalar metric perturbations, and gravitational waves (tensors) which are tensor metric fluctuations[4]. The former experience gravitational instability and lead to structure formation, while the latter propagate in the space-time and can influence the primary CMB anisotropies, as we will see in Chapter 3.

The Concordance Cosmological Model (also referred as the ΛCDM model) is essentially characterized by only six parameters: the matter physical density, $\Omega_{m,0}h^2$, the baryon physical density, $\Omega_{b,0}h^2$, the Hubble constant, H_0, the rms of the linear matter density fluctuations in a sphere 8 Mpc/h by radius, σ_8, the reionization optical depth, κ, which we define next, and the scalar-perturbation spectrum-slope, n_s.

This model assumes a cosmological constant with density $\rho = \Lambda c^2/(8\pi G)$, and pressure $p = wc^2\rho$, where $w = -1$, but it is quite common to see w kept as a free parameter, and even a function of time, to be added to the previous set of parameters in order to account for several dark energy models.

The reionization optical depth is defined as follows. The Universe is known to be highly ionized at low redshifts (otherwise radiation from distant quasars would be heavily absorbed in the ultra-violet), and the ionized electrons can scatter microwave photons altering the pattern of observed anisotropies. The most convenient parameter to describe this is the optical depth to scattering κ (*i.e.* the probability that a given photon scatters once); in the approximation of instantaneous and complete re-ionization, this could equivalently be described by the redshift of re-ionization $z_{\rm ion}$.

Finally, a very important quantity is the ratio of the power spectra associated to the scalar- and tensor-perturbations respectively [4]:

$$r \equiv \frac{\Delta_T^2(k_*)}{\Delta^2(k_*)}\,. \tag{1.19}$$

where k^* is usually the statistical centre of the data range.

[4]Technically, as we will see in detail in the next chapter, density perturbations are often referred to as scalar, corresponding to their Lorentz transformation properties under boosts and rotations. Since the metric has more complicated transformation properties vector and tensor fluctuations are also possible. Vector perturbations, also called vortex perturbations, decay as the universe expands unless they are constantly generated. Tensor perturbations persist and can have an important role in several respects, as we see in the following.

Several experiments prove that the concordance model succeeds in describing the evolution of the Universe and the astronomical observations on scales ranging from a few to thousands of Mpc. It is consistent with both CMB and large-scale structure measurements, as we explain now.

Indeed, as we will explain in Chapter 3, the physics of the CMB is very sensitive to the whole set of cosmological parameters: before recombination, the baryons and photons are tightly coupled, and the perturbations oscillate in the potential wells generated primarily by the dark matter perturbations. After decoupling, the baryons are free to collapse into those potential wells and the CMB carries a record of conditions at the time of decoupling, often called *primary anisotropies*. In addition, it is affected by various processes as it propagates towards us, including the effect of time-varying gravitational potentials, gravitational lensing, and scattering from ionized gas at low redshift. The result is that the detailed pattern of anisotropies (see Fig. 1.1), quantified, for instance, by the anisotropy power at different angles $\vartheta \sim \pi/\ell$ (where ℓ is the Legendre polynomial multipole coefficient), depends on all of the cosmological parameters. Some features can be closely related to specific parameters (for instance, as we see in Chapter 3, the location of the first peak in the power spectrum probes the spatial geometry, while the relative heights of the peaks probes the baryon density) but many other parameters combine to determine the overall shape.

From the three-year results of the Wilkinson Microwave Anisotropy Probe (WMAP–3) [6], the best fit values for the cited set of cosmological parameters in the case of a *flat* ΛCDM model are:

$$\Omega_{m,0}h^2 = 0.1277^{+0.0080}_{-0.0079} \;\; \Omega_{b,0}h^2 = 0.02229 \pm 0.00073 \;\; h = 0.732^{+0.031}_{-0.032}$$
$$n_s = 0.958 \pm 0.016 \;\; \kappa = 0.089 \pm 0.030 \;\; \sigma_8 = 0.761^{+0.049}_{-0.048}.$$

It is important to stress that the baryon abundance is consistent with the one estimated from the observed Deuterium abundance, predicted in the simplest nucleosynthesis scenario [7, 8, 9].

The photon density parameter $\Omega_{r,0}$ is accurately measured directly. The radiation density is dominated by the CMB energy, and the COBE Far Infrared Absolute Spectrophotometer (FIRAS) experiment has determined its temperature to be $T = 2.725 \pm 0.001$ K [10], corresponding to $\Omega_{r,0} = 2.47 \times 10^{-5} h^{-2}$. It typically does not need to be varied in fitting other data. The neutrino energy density instead is often not taken as an independent parameter since it can be related to the photon density using thermal physics

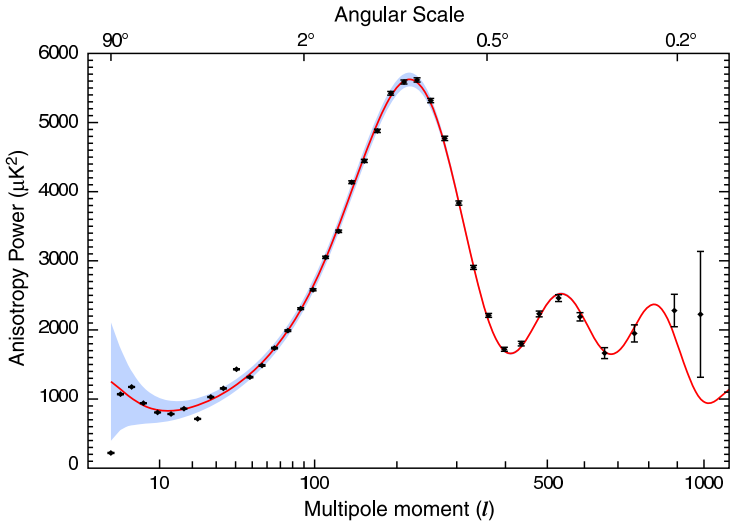

Figure 1.1: *The angular power spectrum of the cosmic microwave background temperature from WMAP–3. The solid line shows the prediction from the best-fitting ΛCDM model [6]. The error bars on the data points (which are tiny for most of them) indicate the observational errors, while the shaded region indicates the Gaussian statistical uncertainty from being able to observe only one microwave sky, known as cosmic variance, which is the dominant uncertainty on large angular scales. The oscillations are a record of the features described in the text. From Ref. [5].*

arguments.

As mentioned in the introduction, about a decade ago, two important studies, the 'Supernova Cosmology Project' and the 'High-z Supernova Search Team', have found evidence for an accelerating Universe [13, 14, 15], interpreted as due to a cosmological constant, or to a more general 'dark energy' component. Current results from the Supernova Cosmology Project [16] are shown in Fig. 1.2. The SNe Ia data alone can only constrain a combination of $\Omega_{m,0}$ and Ω_Λ and, when combined with the CMB data (which indicates flatness, *i.e.*, $\Omega_{m,0} + \Omega_\Lambda \approx 1$), the best-fit values are $\Omega_{m,0} \approx 0.3$ and $\Omega_\Lambda \approx 0.7$. Future experiments will aim to set constraints on the cosmic equation of state $w(z)$ [17].

In a flat universe, the combination of WMAP–3 and the Supernova Legacy Survey (SNLS) data [11] yields best-fits on the equation of state of the dark energy, $w = -0.967$, while, when assuming $w = -1$, the same combination implies $\Omega_{K,0} = -0.011$; moreover, the combination of WMAP–3 data plus the Hubble Space Telescope (HST) key project constraint on H_0 [12] implies $\Omega_{K,0} = -0.014$ and $\Omega_\Lambda = 0.716$. The errors on w and Ω_k are largely consistent with a cosmological constant ($w = -1$) and flatness

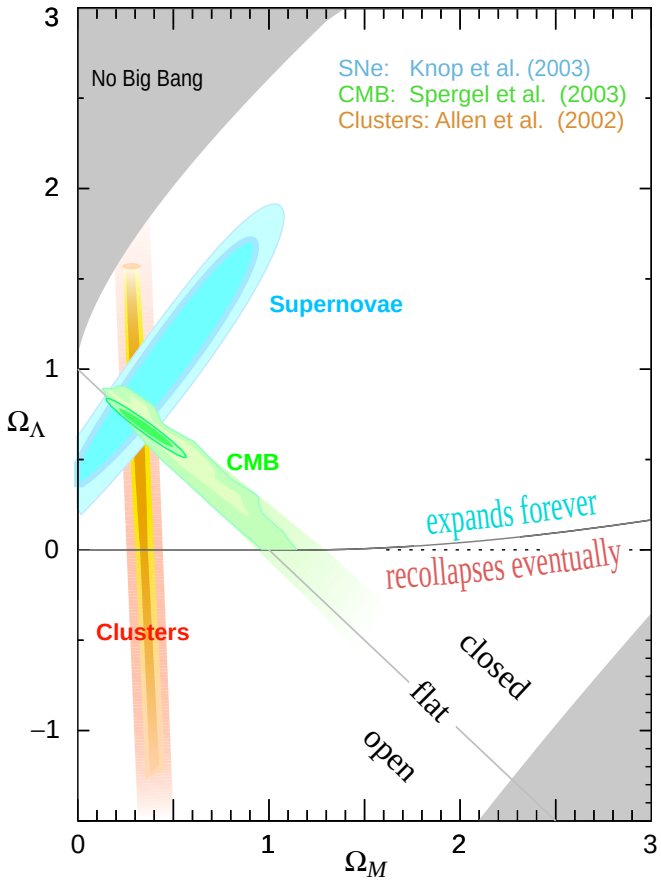

Figure 1.2: *This shows the preferred region in the $\Omega_{m,0}$–Ω_Λ plane from the compilation of supernovae data in [16], and also the complementary results coming from some other observations [18, 19]. From Ref. [4].*

($\Omega_k = 0$) at 1σ. In addition, without the flatness condition, by combining WMAP–3, large-scale structure and supernova data, the constraint on the dark energy equation of state is $w = -1.08 \pm 0.12$, assumed constant.

WMAP–3 provides also an excellent measurement of the location of the first acoustic peak of the CMB temperature spectrum, which directly probes the spatial geometry and yields a total density $\Omega_0 \equiv \sum \Omega_{i,0} + \Omega_\Lambda = 1.003^{+0.013}_{-0.017}$, consistent with spatial flatness and completely excluding significantly curved Universes. This result does however assume a fixed range on the Hubble parameter from other measurements; WMAP–3 alone constrains Ω_0 only weakly, and allows significantly closed Universes if h is small. This result also assumes that the dark energy is a cosmological constant [6]. WMAP–3 also gives a precision measurement of the age of the Universe: for a flat

Universe the position of the first peak is strongly correlated with the age of the Universe and the WMAP–3 result is therefore $13.7^{+0.1}_{-0.2}$ Gyr. This is in good agreement with the ages of the oldest globular clusters [20] and radioactive dating [21].

For what concerns the abundance of cosmological gravitational waves, WMAP–3 data alone puts an upper limit on the tensor to scalar ratio, $r < 0.65$ (95% CL) and the combination of WMAP–3 and the Sloan Digital Sky Survey (SDSS) [22, 23] (which maps the power spectrum of dark matter perturbations through the distribution of galaxies over hundred oh Mpc) implies $r < 0.30$ (95% CL).

Finally, on all but the very largest angular scales [5], the WMAP–3 data are consistent with the assumption that the CMB temperature anisotropy is well-described by a spatial Gaussian random process [26].
In addition to the cited minimal set of parameters, there is a range of other parameters which might prove important in future as the dataset further improves, but for which there is so far no direct evidence other than pure consistency with the ΛCDM model.

In any case, the concordance cosmological model seems now well established, and there is little room left for any dramatic revision of this paradigm.

Nonetheless, it is important not to lose sight of the motivation for developing such a model, which is to understand the underlying physical processes which govern the Universe's evolution. On that side, progress has been much less dramatic. For instance, there are many proposals for the nature of the dark matter, but no consensus on which is correct. The nature of the dark energy remains a mystery. Even the baryon density, now measured to an accuracy of a few percent, lacks an underlying theory able to predict it even within orders of magnitude. Precision cosmology may have arrived, but at present many key questions remain unanswered.

However, over the coming years, there is a wide range of new observations, which will hopefully address fundamental questions of physics well beyond just testing the 'concordance' ΛCDM model and minor variations.

The CMB observations will improve in several directions. The new frontier is the

[5] The few largest-scale angular modes ($l = 2$ mostly) exhibit a lack of power compared to what is expected in a ΛCDM, [24], resulting in some debate about the assumptions of large-scale Gaussianity and spatial isotropy. This feature was also seen in the COBE data [25]. The estimated large-angular-scale CMB temperature anisotropy power depends also on the model used to remove foreground Galactic emission contamination.

study of polarization (first detected from the ground by the Degree Angular Scale Interferometer (DASI) experiment at the South Pole [27]) whose WMAP–3 observations represent the current state of the art [28]. The ability of WMAP–3, and other probes, to measure the so-called "electric" mode of polarization (defined in Sec. 3.2 together with the "magnetic" mode) allows this experiment to probe the early epochs of non-linear structure formation, through sensitivity to the reionization optical depth κ. Dedicated ground-based and balloon-borne polarization experiments, such as the Cosmic Background Imager (CBI), the QUEST (Q and U Extragalactic Sub-mm Telescope) at DASI (QUaD[6]), the Clover Project[7] and the E and B Experiment (EBEX) [29] promise powerful measures of the polarization spectrum in the next few years, including also the magnetic mode. Another area of development is achieving accurate power spectrum measurements to smaller angular scales, typically achieved by interferometry, which should allow measurements of secondary anisotropy effects (see Sec. 3.4), such as the Sunyaev–Zel'dovich effect, whose detection has already been tentatively claimed by CBI[8].

The Planck satellite[9], due to launch in 2008, will make high-precision all-sky maps of temperature and polarization, utilizing a very wide frequency range for observations to improve understanding of foreground contaminants, and to compile a large sample of clusters via the Sunyaev–Zel'dovich effect.

Further information can be extracted by using probes that are sensitive to somewhat different redshift ranges, for example redshift and weak-lensing lensing surveys.

The 2-degree Field Galaxy Redshift Survey (2dFGRS or simply 2dF) is a major spectroscopic survey that has obtained spectra for 220,000 objects, mainly galaxies which cover an area of approximately 1500 square degrees. It is now complete and publicly available[10]. The power-spectrum analysis of the final 2dFGRS data set has been fitted to a ΛCDM model [30] and shows evidence for baryon acoustic oscillations (BAO)[11], with baryon fraction $\Omega_b/\Omega_m = 0.185 \pm 0.046$ (1-σ errors). The shape of the power spectrum is characterized by $\Omega_m h = 0.168 \pm 0.016$, and in combination with WMAP–3 data gives $\Omega_m = 0.231 \pm 0.021$. The 2dF power spectrum is compared with the Sloan Digital

[6] http://www.astro.cf.ac.uk/groups/instrumentation/projects/quad/

[7] http://www.astro.cf.ac.uk/groups/instrumentation/projects/clover/

[8] http://www.astro.caltech.edu

[9] http://www.rssd.esa.int/index.php?project=Planck

[10] http://www.mso.anu.edu.au/2dFGRS

[11] The same physics that leads to acoustic peaks in the CMB anisotropy causes oscillations in the galaxy power spectrum

Sky Survey (SDSS) [12] power spectrum [31] in Fig. 1.3. Ref. [32] reported the detection of baryon acoustic peak in the large-scale correlation function of the SDSS sample of nearly 47,000 Luminous Red Galaxies. By using the baryon acoustic peak as a 'standard ruler' they found, independently on WMAP, that $\Omega_m = 0.273 \pm 0.025$ for a flat ΛCDM model.

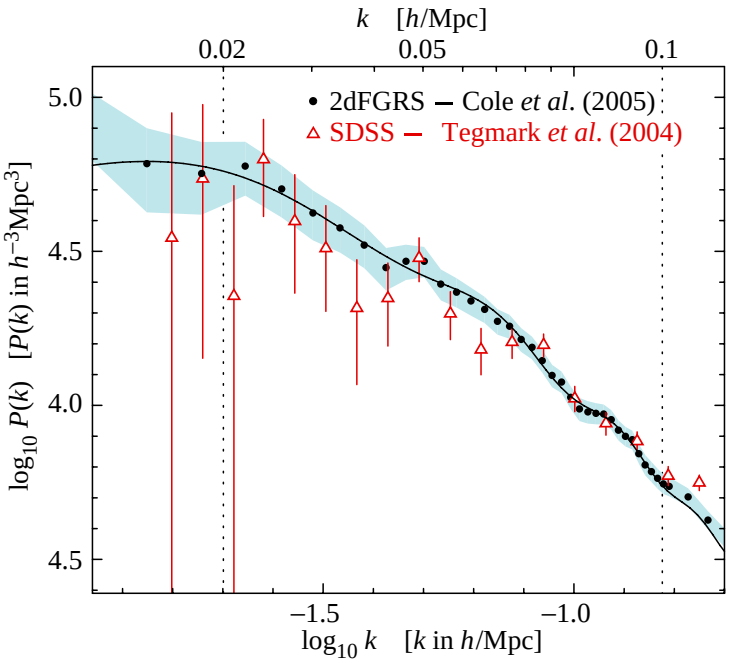

Figure 1.3: *The galaxy power spectrum from the 2dF galaxy redshift survey compared with that from SDSS, each corrected for its survey geometry. The 2dFGRS power spectrum is shown by solid circles with one-sigma errors shown by the shaded area. The triangles and error bars show the SDSS power spectrum. The solid curve shows a linear-theory ΛCDM model with $\Omega_m h = 0.168$, $\Omega_b/\Omega_m = 0.17$, $h = 0.72$, $n_s = 1$ and normalization matched to the 2dFGRS power spectrum. The dotted vertical lines indicate the range over which the best-fit model was evaluated. From Ref. [30].*

The SDSS collaboration has very recently presented cosmological results from the statistics of lensed quasars in the SDSS Quasar Lens Search (QLS) [33]. They derive constraints on the equation of state w as well as the dark energy abundance, Fig. 1.4. For a flat cosmological constant model ($w = -1$) they obtain $\Omega_\Lambda = 0.74^{+0.11}_{-0.15}(\text{stat.})^{+0.13}_{-0.06}(\text{syst.})$. Allowing w to be a free parameter they find $\Omega_m = 0.26^{+0.07}_{-0.06}(\text{stat.})^{+0.03}_{-0.05}(\text{syst.})$ and $w = -1.1 \pm 0.6(\text{stat.})^{+0.3}_{-0.5}(\text{syst.})$ when combined with

[12] http://www.sdss.org

the constraint from the measurement of baryon acoustic oscillations in the SDSS luminous red galaxy sample. Their results provide additional confirmation of the presence of dark energy consistent with a cosmological constant, derived independently of Type Ia supernovae.

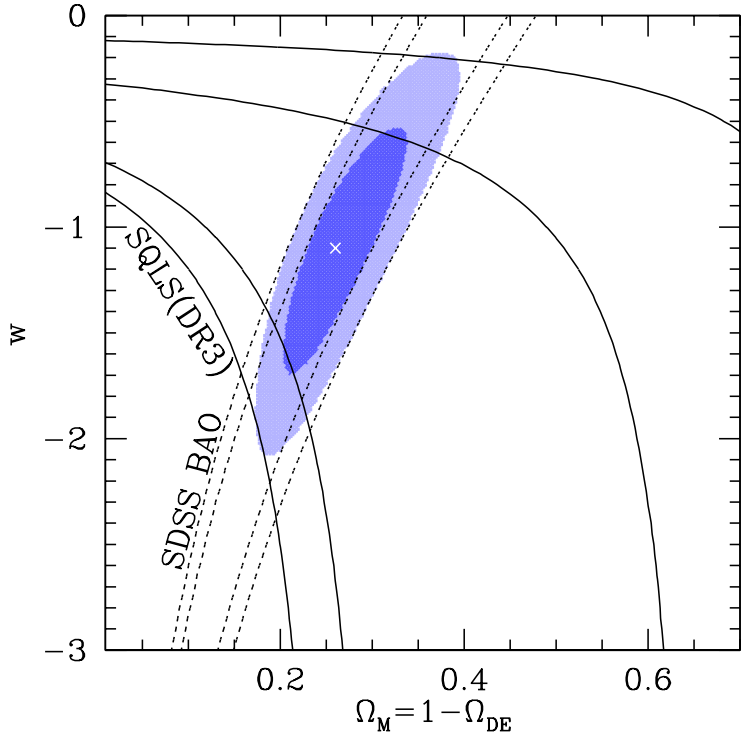

Figure 1.4: *Contours at 1σ and 2σ confidence levels are plotted in the Ω_m-w plane. Solid lines indicate the constraint from the SQLS DR3, whereas dotted lines are from the BAOs detected in the SDSS luminous red galaxy power spectrum [32]. The joint constraint from SQLS and BAO are shown by shaded regions: The best-fit model (Ω_m, w)=(0.26, −1.1) is indicated with a cross. From Ref. [33]*

In Chapter 4 we will illustrate the process of weak gravitational lensing, which is one of the most promising cosmological probes, and the subject of this work. Background light, coming from distant galaxies or CMB, gets weakly deflected by forming cosmological structures. Galaxies gain an extra-ellipticity because of this process, which is function of their redshift and the overall lensing efficiency, *i.e.* amount and statistics of cosmological structures. In addition, dividing background galaxies in redshift shells, the lenses can be probed in a sort of differential way in time, making an effective tomography of the structures formation process.
Un to now, lensing has been detected with great consistency by several groups, and

provide large agreement with the ΛCDM model [35, 36].

Several projects have been proposed for the future, in particular for constraining the onset of acceleration, *i.e.* trying to discriminate between different dark energy models.

Among them, the Dark Universe Explorer satellite (DUNE) [17] from the European Space Agency (ESA), aiming at a weak lensing survey of galaxies on 20000 squared degree, with a depth of about 0.5 in redshift.

Similar projects are being scrutinized by the National Aeronautic Space Administration[13] (NASA) such as the Supernova Acceleration Probe[14] (SNAP), focused on supernova but with outstanding lensing sensitivity. Other satellites are being conceived within the Joint Dark Energy Mission (JDEM). From the ground, the most ambitious is the Large Scale Synoptic Telescope[15].

[13] http://lambda.gsfc.nasa.gov

[14] http://snap.lbl.gov

[15] http://www.lssto.org

Chapter 2

Linear and non-linear cosmological perturbations

The important results obtained in Cosmology from the observations of CMB anisotropy, weak gravitational lensing and large-scale structure from galaxy redshift catalogs, the increasing precision that has been, and will be achieved by future experimental determinations, require comparable accuracy in the theoretical of the several contributions to these effects.

The primary driver for the formation of large-scale structure in the Universe is gravitational instability. The detailed growth of structure depends on the nature of the initial fluctuations, the background cosmology, and the constituents of the mass-energy density, as causal physics influences the rate at which structure may grow on different scales.

Jeans in 1902 studied the stability of a spherical distribution of gravitating gas particles in flat spacetime, motivated by possible relevance to the process of star formation. He discovered that gas pressure prevents gravitational collapse on small spatial scales and gives rise to acoustic oscillations in the mass density inhomogeneity, as pressure gradient and gravitational forces compete. On large scales the gravitational force dominates and mass density inhomogeneities grow exponentially with time. The length scale on which the two forces balance has come to be known as the Jeans length or the acoustic Hubble length c_s/H_0, where c_s is the speed of sound related to the pressure of the fluid under consideration.

On scales smaller than the Jeans length, adiabatic energy density perturbations oscillate as acoustic waves. On scales well below the Jeans length, dissipative fluid effects (e.g., viscosity and radiation diffusion) must be accounted for. These effects remove energy

from the acoustic waves, thus damping them. In an expanding Universe, damping is effective when the dissipation time scale is shorter than the expansion time scale, and the smallest length scale for which this is the case is called the damping length.

The study of gravitational instability in an evolving spacetime, appropriate for the expanding Universe, began with Lemaître in the early 1930's. He pioneered two approaches, both of which are still in use: a "nonperturbative" approach based on a spherically symmetric solution of the Einstein equations (further developed by Dingle, Tolman, Bondi, and others) and a "perturbative" approach in which one studies small departures from spatial homogeneity and isotropy evolving in homogeneous and isotropic background spacetimes.

Lifshitz in 1946 laid the foundations of the general-relativistic perturbative approach to structure formation. He linearized the Einstein and stress-energy conservation equations about a spatially homogeneous and isotropic FRW background and decomposed the departures from homogeneity and isotropy into independently evolving spatial harmonics, the so-called *scalar, vector, and tensor modes*.
Unlike the exponentially growing energy density irregularity that Jeans found in flat spacetime on large scales, Lifshitz found only a much slower power-law temporal growth, leading him to the incorrect conclusion that "gravitational instability is not the source of condensation of matter into separate nebulae". Two decades after, Novikov corrected this misunderstanding, noting that even with power-law growth there was more than enough time for inhomogeneities to grow, since they could do so even while they were on scales larger than the Hubble length $r_H = c/H_0$ at early times.
The approach to the theory of linear perturbations initiated by Lifshitz was performed in the synchronous gauge but, in 1980, Bardeen [37] recasted this analysis in a coordinate-independent form.

Different kinds of techniques have been developed in the last decades, depending on the specific range of scales under consideration.
For instance, on scales well inside the Hubble horizon, but still much larger than the Schwarzschild radius of collapsing bodies, the study of gravitational instability of collisionless matter is performed using the *Newtonian* approximation. It consists in inserting in the line-element of a FRW background Eq. (1.3) the lapse perturbation $2\varphi_N/c^2$, where φ_N plays the role of the Newtonian potential and is related to the matter density fluctuation $\delta\rho$ via the cosmological Poisson equation $\nabla^2\varphi_N = 4\pi G a^2 \delta\rho$. The dynamics of the system is then studied in Eulerian coordinates by accounting for the Newtonian mass

and momentum conservation equations (the so-called continuity and Euler equations), owing to the fact that the peculiar matter flow v never becomes relativistic [38].

The Newtonian limit, according to which the gravitational field φ is always much less than the square of the light speed, c^2, can be improved by a *post-Newtonian* (PN) approach to account for the moderately strong gravitational fields generated during collapse. In this case, by considering the expansion of the general relativistic equations in inverse powers of the speed of light, it is possible to neglect terms of order $(v/c)^4$ in the equations of motions, i.e. to perform a first post-Newtonian (1PN) approximation, which in Eulerian coordinates accounts for non vanishing shift components and for an extra perturbation term $-2\varphi_N/c^2$ in the spatial part of the line-element. Calculations using higher and higher orders of $1/c$ would generally lead to a more accurate description of the system, e.g. accounting for the generation of gravitational waves, and possibly allow for an extension of the range of scales to which the formalism can be applied. A PN approach to cosmological perturbations has been followed in Refs. [39, 40, 41], using Eulerian coordinates, while Ref. [42] uses Lagrangian coordinates.

On the other hand, the first-order perturbations for non-relativistic matter, obtained with the Newtonian treatment, coincide with the results of the general *relativistic linear perturbation* theory in the *longitudinal* (or *Eulerian Newtonian*) gauge [43]. The relativistic linear perturbative approach is the one applied to the study of the small inhomogeneities giving rise to large-scale anisotropies of the CMB. However, on small and intermediate scales, linear theory is no longer accurate and a general fully *relativistic second-order perturbative* technique is required. In fact, second-order metric perturbations determine new contributions to the CMB temperature anisotropy [44, 45] and polarization [46, 47]. In particular, second-order scalar, vector and tensor metric perturbations produce secondary anisotropies in the temperature and polarization of the CMB which are in competition with other non-linear effects, such as that due to weak gravitational lensing produced by matter inhomogeneities.

Moreover, accounting for second-order effects helps to follow the gravitational instability on a longer time scale and to include new non-linear and non-local phenomena. The pioneering work in this field is due to Tomita [48] who performed a synchronous-gauge calculation of the second-order terms produced by the mildly non-linear evolution of scalar perturbations in the Einstein-de Sitter Universe. An equivalent result, was obtained with a different technique in Ref. [49]. The inclusion of vectors and tensor modes at the linear level, acting as further seeds for the origin of second-order perturba-

tions of any kind was first considered in Ref. [50]; in Ref. [51] the evolution of relativistic perturbations in the Einstein-de Sitter cosmological model was considered and second-order effects were included in two different settings: the synchronous and the so-called *Poisson gauge* [52].

As we have stressed, the evolution of cosmological perturbations away from the linear level is rich of several effects as, in particular, mode-mixing which not only implies that different Fourier modes influence each other, but also that density perturbations act as a source for curl vector modes and gravitational waves.

The aim of this chapter is therefore to present a *unified treatment* able to follow the evolution of cosmological perturbations from the linear to the highly non-linear regime. As we will show hereafter, this goal is indeed possible on scales much larger than the Schwarzschild radius of collapsing bodies, by means of a *hybrid approximation* of Einstein's field equations, which mixes post-Newtonian (PN) and second-order perturbative techniques to deal with the perturbations of matter and geometry. In our study we adopt the Poisson gauge which, being the closest to the Eulerian Newtonian gauge, allows a simple physical interpretation of the various perturbation modes.

We derive a set of equations, which was presented for the first time in Ref. [53], and which holds on all the cosmologically relevant scales and allows to describe matter inhomogeneities during all the different stages of their evolution. The new approach gives a more accurate description of the metric perturbations generated by non-linear structures than the second-order perturbation theory, which can only account for small deviations from the linear regime. For example, on small scales our set of equations can be used to provide a PN description of metric perturbations generated by highly non-linear structures within dark matter haloes, while describing their motion by means of the standard Newtonian hydrodynamical equations. On large scales our equations converge to the first and second-order perturbative equations as obtained in Ref. [51] (see also Refs. [54, 55]), which implies that they can be applied to every kind of cosmological sources.

Among these sources, CDM haloes are noteworthy since the current knowledge of cosmological structure formation suggests they possess a non-spherical density profile, implying that cosmic structures can be potential sources of gravitational waves via power transfer from scalar perturbations to tensor metric modes in the non-linear regime.

Thus, as an application of our formalism, by means of a triaxial collapse model, we

numerically estimate the stochastic gravitational-wave background generated by CDM haloes during the fully non-linear stage of their evolution. Our results [56] suggest that the energy density associated with this background is comparable to that produced by primordial tensor modes at frequencies $\nu \approx 10^{-18} - 10^{-17}$Hz if the energy scale of inflation is $V^{1/4} \approx 1 - 2 \times 10^{15}$ GeV, and that these gravitational waves could give rise to several cosmological effects, including secondary CMB anisotropy and polarization.

This Chapter is organized as follows. In Sec. 2.1 we review the scalar, vector and tensor decomposition of metric perturbations. In Secs. 2.2-2.4 we describe the source of metric perturbations in the stress-energy tensor and complete the perturbative treatment. In Sec. 2.5 we review the sources of gravitational waves and in Secs. 2.6-2.9 we compute the spectrum of the gravitational radiation emitted by collapsing dark matter haloes in the non-linear regime.

2.1 Scalar, vector and tensor metric perturbation modes

Adopting the conformal time η and comoving coordinates x^α, the perturbed line-element around a spatially flat FRW background Eq. (1.3) in the Poisson gauge [43, 51] takes the form

$$ds^2 = a^2(\eta)\left[-(1+2\phi)d\eta^2 - 2V_\alpha d\eta dx^\alpha + ((1-2\psi)\,\delta_{\alpha\beta} + h_{\alpha\beta})\,dx^\alpha dx^\beta\right] . \tag{2.1}$$

In Eq. (2.1) the metric includes perturbative terms of any order around the FRW background. In this gauge, V_α are pure vectors, i.e. they have vanishing spatial divergence, $\partial^\alpha V_\alpha = 0$, while $h_{\alpha\beta}$ are traceless and transverse, i.e. pure tensor modes, $h^\alpha{}_\alpha = \partial^\alpha h_{\alpha\beta} = 0$. As already mentioned, Greek indices denote spatial components and are raised by the Kronecker symbol $\delta^\alpha{}_\beta$. Unless otherwise stated, we use units with $c = 1$. From the results of the post-Newtonian theory [57, 58, 59, 42], we deduce that vector and tensor metric modes, to the leading order in powers of $1/c$, are respectively of $\mathcal{O}(1/c^3)$ and $\mathcal{O}(1/c^4)$, since to the lowest order it is well known that the line-element (2.1) assumes the weak-field form $ds^2 = a^2[-(1+2\phi_1)\,d\eta^2 + (1-2\psi_1)\,\delta_{\alpha\beta}dx^\alpha dx^\beta]$, where the scalars ϕ_1 and ψ_1 are both of $\mathcal{O}(1/c^2)$ and $\phi_1 = \psi_1 \equiv \varphi$ [38].

Let us now write Einstein's equations $G^i{}_j = \kappa^2 T^i{}_j$ in the perturbed form

$${}^{(0)}G^i{}_j + \delta G^i{}_j = \kappa^2\left({}^{(0)}T^i{}_j + \delta T^i{}_j\right) , \tag{2.2}$$

where $\kappa^2 = 8\pi G/c^4$ and ${}^{(0)}G^i{}_j = \kappa^2\,{}^{(0)}T^i{}_j$ reduce to the background Friedmann equations. Hereafter, we assume that the Universe is filled with a cosmological con-

stant Λ and a pressureless fluid – made of Cold Dark Matter plus baryons – whose stress energy-tensor reads $T^i{}_j = \rho u^i u_j$ ($u^i u_j = -1$). In this case Eqs. (1.6)-(1.7) read $3\mathcal{H}^2 = a^2\,(8\pi G\bar{\rho} + \Lambda)$ and $\bar{\rho}\,' = -3\mathcal{H}\bar{\rho}$, where primes indicate differentiation with respect to η, $\mathcal{H} \equiv a'/a$, $\bar{\rho}$ is the mean matter energy density and a is the scale factor of the Universe which evolves according to the FRW background model.

Since the metric (2.1) can be expressed in an invariant form both in the PN and in the second-order perturbative approximations, we introduce a hybrid formalism that consists in evaluating Einstein's field equations up to the correct order in powers of $1/c$, while including some "hybrid" correction terms, which cannot be completely absorbed in a "rigid" PN approximation, but are required for consistency with a second-order general relativistic approximation.

Namely, writing $\psi = \psi_1 + \psi_2$ and $\phi = \phi_1 + \phi_2$ (where ψ_2 and ϕ_2 in principle contain all powers of $1/c$), and replacing the metric (2.1) in Eq. (2.2), the (0-0) and (0-α) components of the perturbed Einstein equations take the form

$$\delta G^0{}_0 = -\frac{1}{a^2}\,\Big[-6\mathcal{H}\,(\mathcal{H}\phi_1 + \psi_1') + 2\nabla^2\psi + 3\partial^\nu\psi_1\partial_\nu\psi_1 + 8\psi_1\nabla^2\psi_1 + \mathcal{S}_1\Big] = \kappa^2\delta T^0{}_0\,, \qquad (2.3)$$

where $\mathcal{S}_1 \equiv 12\mathcal{H}^2\phi_1^2 + 3\psi_1'^2 + 12\mathcal{H}\phi_1\psi_1' - 12\mathcal{H}\psi_1\psi_1'$, and

$$\delta G^0{}_\alpha = -\frac{2}{a^2}\left(\mathcal{H}\partial_\alpha\phi_1 + \partial_\alpha\psi_1' + \frac{1}{4}\nabla^2 V_\alpha + \mathcal{S}_{2\alpha}\right) = \kappa^2\,\delta T^0{}_\alpha\,, \qquad (2.4)$$

where $\mathcal{S}_{2\alpha} \equiv -4\mathcal{H}\phi_1\partial_\alpha\phi_1 - 2\phi_1\,\partial_\alpha\psi_1' - \psi_1'\partial_\alpha\,\phi_1 + 2\psi_1'\partial_\alpha\psi_1 + 2\psi_1\partial_\alpha\psi_1'$.

The traceless part of the (α-β) Einstein's equations $\delta G^\alpha{}_\beta = \kappa^2\,\delta T^\alpha{}_\beta$ reads

$$\begin{aligned}
&2a^2\kappa^2\Big(\delta T^\alpha{}_\beta - \frac{1}{3}\delta T^\nu{}_\nu\delta^\alpha{}_\beta\Big) = \delta^\alpha{}_\beta \\
&\times\left[\frac{2}{3}\,\nabla^2(\phi-\psi) - \frac{8}{3}\,\psi_1\nabla^2\psi_1 - \frac{4}{3}\,\phi_1\nabla^2\phi_1 + \frac{4}{3}\,\psi_1\nabla^2\phi_1 - \frac{2}{3}\,\partial^\nu\phi_1\partial_\nu\phi_1 + \frac{4}{3}\,\partial_\nu\phi_1\partial^\nu\psi_1 - 2\partial^\nu\psi_1\partial_\nu\psi_1\right] \\
&- 2\partial^\alpha\partial_\beta(\phi-\psi) + 8\psi_1\partial^\alpha\partial_\beta\psi_1 + 6\partial^\alpha\psi_1\partial_\beta\psi_1 - 2\partial^\alpha\phi_1\partial_\beta\psi_1 + 2\partial^\alpha\phi_1\partial_\beta\phi_1 - 2\partial^\alpha\psi_1\partial_\beta\phi_1 + 4\phi_1\partial^\alpha\partial_\beta\phi_1 \\
&- 4\psi_1\partial^\alpha\partial_\beta\phi_1 + \partial^\alpha(2\mathcal{H}\,V_\beta + V_\beta') + \partial_\beta(2\mathcal{H}\,V^\alpha + V'^\alpha) + h''^\alpha{}_\beta + 2\mathcal{H}h'^\alpha{}_\beta - \nabla^2 h^\alpha{}_\beta\,, \qquad (2.5)
\end{aligned}$$

while its trace becomes

$$\begin{aligned}
&2\nabla^2(\phi-\psi) + 6\mathcal{H}\phi_1' + 6(\mathcal{H}^2 + 2\mathcal{H}')\phi_1 + 6\psi_1'' + 12\mathcal{H}\psi_1' - 2\partial^\nu\phi_1\partial_\nu\phi_1 \\
&- 4\phi_1\nabla^2\phi_1 - 3\partial_\nu\psi_1\partial^\nu\psi_1 - 8\psi_1\nabla^2\psi_1 + 4\psi_1\nabla^2\phi_1 - 2\partial_\nu\phi_1\partial^\nu\psi_1 = a^2\kappa^2\delta T^\nu{}_\nu\,. \qquad (2.6)
\end{aligned}$$

The components of the perturbed stress-energy tensor $\delta T^i{}_j$ will be calculated later to the correct order in powers of $1/c$. Note that Eqs. (2.3), (2.5) and (2.6) are evaluated up to $\mathcal{O}(1/c^4)$, while Eq. (2.4) is evaluated up to $\mathcal{O}(1/c^3)$. However, the terms $\mathcal{S}_1$ and

$\mathcal{S}_{2\alpha}$ are at least of $\mathcal{O}(1/c^6)$ and $\mathcal{O}(1/c^5)$, respectively, and come out from our hybrid scheme, which mixes PN and second-order perturbative approaches. Moreover, since our purpose is to calculate the source of gravitational waves to the leading order in powers of $1/c$, in Eq. (2.5) we do not take into account contributions of order higher than $\mathcal{O}(1/c^4)$, though retaining time derivatives of $h^\alpha{}_\beta$.

Taking the divergence of Eq. (2.4), to solve for the combination $\mathcal{H}\phi_1 + \psi_1'$, and replacing it in Eq. (2.3), we obtain

$$\nabla^2(\mathcal{H}\phi_1 + \psi_1') = -\frac{a^2\kappa^2}{2}\partial^\nu \delta T^0{}_\nu - \partial^\nu \mathcal{S}_{2\nu}\,, \tag{2.7}$$

and

$$\begin{aligned}\nabla^2\nabla^2\psi = \nabla^2\nabla^2(\psi_1+\psi_2) = &-\frac{a^2\kappa^2}{2}\left[\nabla^2\delta T^0{}_0 + 3\mathcal{H}(\partial^\nu \delta T^0{}_\nu)\right] - 3\mathcal{H}\partial^\nu\mathcal{S}_{2\nu} - \frac{1}{2}\nabla^2\mathcal{S}_1 \\ &- \nabla^2\left(\frac{3}{2}\partial^\nu\psi_1\partial_\nu\psi_1 + 4\psi_1\nabla^2\psi_1\right)\,.\end{aligned} \tag{2.8}$$

The pure vector part V_α can be isolated by replacing $\nabla^2(\mathcal{H}\phi_1 + \psi_1')$ in Eq. (2.4), where we now neglect the term $\mathcal{S}_{2\alpha}$ since it is at least of $\mathcal{O}(1/c^5)$

$$\nabla^2\nabla^2 V_\alpha = 2a^2\kappa^2\left(\partial_\alpha\partial^\nu\delta T^0{}_\nu - \nabla^2\delta T^0{}_\alpha\right)\,. \tag{2.9}$$

Finally, applying the operator $\partial^\beta\partial_\alpha$ to Eq. (2.5), we can solve for the combination $\phi - \psi$ and write

$$\begin{aligned}\nabla^2\nabla^2(\phi-\psi) = &-\frac{3}{2}a^2\kappa^2\partial^\beta\partial_\alpha\left(\delta T^\alpha{}_\beta - \frac{1}{3}\delta T^\nu{}_\nu\delta^\alpha{}_\beta\right) \\ &+ \frac{3}{2}\partial_\alpha\partial^\beta\left(\partial_\beta\psi_1\partial^\alpha\phi_1 - \partial_\beta\phi_1\partial^\alpha\psi_1 - \partial_\beta\psi_1\partial^\alpha\psi_1 - \partial_\beta\phi_1\partial^\alpha\phi_1\right) \\ &+ \nabla^2\left(\frac{9}{2}\partial_\nu\psi_1\partial^\nu\psi_1 - 2\partial_\nu\psi_1\partial^\nu\phi_1 + \frac{5}{2}\partial_\nu\phi_1\partial^\nu\phi_1 + 4\psi_1\nabla^2\psi_1 + 2\phi_1\nabla^2\phi_1 - 2\psi_1\nabla^2\phi_1\right)\,.\end{aligned} \tag{2.10}$$

Replacing the latter expression in Eq. (2.5), together with the expression for the vector mode V_α obtained by taking the divergence of Eq. (2.5), we find

$$\begin{aligned}\nabla^2\nabla^2\left(h''^\alpha{}_\beta + 2\mathcal{H}h'^\alpha{}_\beta - \nabla^2 h^\alpha{}_\beta\right) = 2\kappa^2a^2\big[&\nabla^2\left(\nabla^2\mathcal{R}^\alpha{}_\beta - \partial^\alpha\partial_\nu\mathcal{R}^\nu{}_\beta - \partial_\beta\partial^\nu\mathcal{R}^\alpha{}_\nu\right) \\ &+ \frac{1}{2}\left(\nabla^2\partial^\mu\partial_\nu\mathcal{R}^\nu{}_\mu\,\delta^\alpha{}_\beta + \partial^\alpha\partial_\beta\partial^\mu\partial_\nu\mathcal{R}^\nu{}_\mu\right)\big]\,,\end{aligned} \tag{2.11}$$

where we have defined the traceless tensor

$$\begin{aligned}\mathcal{R}^\alpha{}_\beta = &\,\delta T^\alpha{}_\beta - \frac{1}{3}\delta T^\nu{}_\nu\delta^\alpha{}_\beta \\ &- \frac{1}{\kappa^2a^2}\left(\frac{2}{3}\psi_1\nabla^2\phi_1 + \frac{2}{3}\partial_\nu\phi_1\partial^\nu\psi_1 - \frac{4}{3}\psi_1\nabla^2\psi_1 - \frac{2}{3}\phi_1\nabla^2\phi_1 - \frac{1}{3}\partial^\nu\phi_1\partial_\nu\phi_1 - \partial^\nu\psi_1\partial_\nu\psi_1\right)\delta^\alpha{}_\beta \\ &- \frac{1}{\kappa^2a^2}\left(4\psi_1\partial^\alpha\partial_\beta\psi_1 + 3\partial^\alpha\psi_1\partial_\beta\psi_1 - \partial^\alpha\phi_1\partial_\beta\psi_1 + \partial^\alpha\phi_1\partial_\beta\phi_1 - \partial^\alpha\psi_1\partial_\beta\phi_1 + 2\phi_1\partial^\alpha\partial_\beta\phi_1 - 2\psi_1\partial^\alpha\partial_\beta\phi_1\right)\,.\end{aligned} \tag{2.12}$$

The form of Eq. (2.9) and Eq. (2.11) allows to directly check that vector sources are transverse while tensor sources are doubly transverse and traceless.

Actually, there is a very simple way of solving the perturbed Einstein equations $\delta G^0{}_\alpha = \kappa^2 a^2 \delta T^0{}_\alpha$ and $\delta G^\alpha{}_\beta = \kappa^2 a^2 \delta T^\alpha{}_\beta$ with respect to the vectors V_α and the tensors $h^\alpha{}_\beta$, respectively. In fact, after retaining only the metric terms which appear linearly on the LHS of Eq. (2.4) and Eq. (2.5) [1] and defining as $\mathcal{R}^\alpha{}_\beta$ the consequently obtained RHS, it is possible to apply to both sides the correct combinations of the direction-independent projection operator [60]

$$\mathcal{P}^\alpha{}_\beta = \delta^\alpha{}_\beta - \left(\nabla^2\right)^{-1} \partial^\alpha \partial_\beta \,, \tag{2.13}$$

and automatically obtain the vectors

$$\nabla^2 V_\alpha = -2a^2\kappa^2 \mathcal{P}^\nu{}_\alpha \left(\delta T^0{}_\nu - \frac{2}{a^2\kappa^2}\mathcal{S}_{2\nu}\right) \,, \tag{2.14}$$

and tensors

$$h''^\alpha{}_\beta + 2\mathcal{H} h'^\alpha{}_\beta - \nabla^2 h^\alpha{}_\beta = 2\kappa^2 a^2 \left(\mathcal{P}^\alpha{}_\nu \mathcal{P}^\mu{}_\beta - \frac{1}{2}\mathcal{P}^\alpha{}_\beta \mathcal{P}^\mu{}_\nu\right) \mathcal{R}^\nu{}_\mu \,. \tag{2.15}$$

After applying twice the Laplacian operator to Eq. (2.15) and neglecting as before the term $\mathcal{S}_{2\nu}$ in Eq. (2.14), we recover Eq. (2.9) and Eq. (2.11).

2.2 The stress-energy tensor and the source of metric perturbations

For the purpose of calculating the components of the perturbed stress-energy tensor $\delta T^i{}_j$ to the correct order in powers of $1/c$, it is convenient to restore the speed of light c in the time coordinate $dx^0 = cd\eta$. From Eq. (2.1) we obtain the four-velocity $u^i \equiv dx^i/ds$

$$u^0 \simeq \frac{1}{a}\left[1 - \frac{1}{2}\left(2\phi_1 - \frac{v^2}{c^2}\right)\right] + \mathcal{O}\left(\frac{1}{c^4}\right) \,, \tag{2.16}$$

$$u^\alpha = \frac{v^\alpha}{c} u^0 + \mathcal{O}\left(\frac{1}{c^5}\right) \,, \tag{2.17}$$

where $v^2 = v^\nu v_\nu$ and $v^\alpha \equiv dx^\alpha/d\eta$ is the coordinate three-velocity with respect to the FRW background.

[1] In this context we are using the traceless part of $\delta G^\alpha{}_\beta = \kappa^2 a^2 \delta T^\alpha{}_\beta$, but this is not strictly necessary; it is indeed sufficient to apply the projection operator to the whole equation $\delta G^\alpha{}_\beta = \kappa^2 a^2 \delta T^\alpha{}_\beta$.

The total energy-momentum tensor for our fluid of dust and cosmological constant reads

$$T^i{}_k = {}^{(0)}T^i{}_k + \delta T^i{}_k = \left[(\rho_\Lambda + \rho)c^2 + p_b\right] g_{kj}u^i u^j + p_b \delta^i{}_k \,, \tag{2.18}$$

where ${}^{(0)}T^i{}_k$ is the background stress-energy tensor and $\rho = \bar{\rho} + \delta\rho$ is the total mass-density. The background density $\rho_b = \bar{\rho} + \rho_\Lambda$ includes the contribution from the cosmological constant, $\rho_\Lambda = (\Lambda c^2)/(8\pi G)$, while the background pressure $p_b = p_\Lambda = -\rho_\Lambda c^2$ is only due to the latter.

Turning to the components of the perturbed energy-momentum tensor, in terms of the coefficients $\phi_1$and ψ_1 of the metric (2.1) and up to the correct orders in powers of $1/c$, we find

$$\delta T^0{}_0 = T^0{}_0 - {}^{(0)}T^0{}_0 = -c^2\delta\rho - v^2\rho + \mathcal{O}\left(\frac{1}{c^2}\right) , \tag{2.19}$$

$$\delta T^0{}_\alpha = T^0{}_\alpha - {}^{(0)}T^0{}_\alpha = v_\alpha \rho c \left(1 - 2\phi_1 - 2\psi_1\right) + \frac{v_\alpha}{c}\rho v^2 + \mathcal{O}\left(\frac{1}{c^3}\right) , \tag{2.20}$$

$$\delta T^\alpha{}_0 = T^\alpha{}_0 - {}^{(0)}T^\alpha{}_0 = -v^\alpha \rho c - \frac{v^\alpha}{c}\rho v^2 + \mathcal{O}\left(\frac{1}{c^3}\right) , \tag{2.21}$$

$$\delta T^\alpha{}_\beta = T^\alpha{}_\beta - {}^{(0)}T^\alpha{}_\beta = v^\alpha v_\beta \rho \left(1 - 2\phi_1 - 2\psi_1 + \frac{v^2}{c^2}\right) + \mathcal{O}\left(\frac{1}{c^4}\right) . \tag{2.22}$$

In the hybrid equations which we are about to derive we will keep step by step only the $\delta T^i{}_j$ components we need to let our set of equations hold in the first, second perturbative order and PN regimes.

By substituting $\delta T^\alpha{}_\beta$ in Eq. (2.10), we obtain up to $\mathcal{O}(1/c^2)$

$$\nabla^2\nabla^2(\phi_1 - \psi_1) = 0 \,, \tag{2.23}$$

and we can safely assume $\phi_1 = \psi_1 \equiv \varphi$.

This allows to further simplify Eqs. (2.6)-(2.10) and obtain our final set of hybrid equations for cosmological perturbations, namely

$$\nabla^2(\mathcal{H}\varphi + \varphi') = -\frac{a^2\kappa^2 c^2}{2}\partial^\nu(\rho v_\nu) \,, \tag{2.24}$$

$$\nabla^2\nabla^2\psi = -\frac{a^2\kappa^2}{2}\left[3\mathcal{H}\partial^\nu(\rho\, v_\nu(1-4\varphi)) - \nabla^2(c^2\delta\rho + \rho\, v^2)\right] + 3\frac{\mathcal{H}}{c}\partial^\nu\left(4\frac{\mathcal{H}}{c}\varphi\partial_\nu\varphi - \frac{1}{c}\varphi'\partial_\nu\varphi\right) - \nabla^2\left(\frac{3}{2}\partial^\nu\varphi\partial_\nu\varphi + 4\varphi\nabla^2\varphi + 6\frac{\mathcal{H}^2}{c^2}\varphi^2 + \frac{3}{2c^2}\varphi'^2\right) , \tag{2.25}$$

$$\nabla^2\nabla^2 V_\alpha = 2a^2\kappa^2\left[\partial_\alpha\partial^\nu(c\rho\, v_\nu) - \nabla^2(c\rho\, v_\alpha)\right] , \tag{2.26}$$

$$\nabla^2\nabla^2(\phi-\psi) = -\frac{3}{2}a^2\kappa^2\partial^\mu\partial_\nu\left(\rho\, v^\nu v_\mu - \frac{1}{3}\rho\, v^2\delta^\nu{}_\mu\right) + \nabla^2\left(5\partial_\nu\varphi\partial^\nu\varphi + 4\varphi\nabla^2\varphi\right) - 3\partial_\nu\partial^\mu\left(\partial_\mu\varphi\partial^\nu\varphi\right) , \tag{2.27}$$

$$\nabla^2\nabla^2\phi = -\frac{a^2\kappa^2}{2}\left[3\mathcal{H}\partial^\nu\left(\rho\, v_\nu(1-4\varphi)\right) + 3\partial^\mu\partial_\nu(\rho\, v^\nu v_\mu) - \nabla^2(c^2\delta\rho + 2\rho\, v^2)\right] + \frac{7}{2}\nabla^2(\partial_\nu\varphi\partial^\nu\varphi) - 3\partial_\nu\partial^\mu(\partial_\mu\varphi\partial^\nu\varphi) + 3\frac{\mathcal{H}}{c}\partial^\nu\left(4\frac{\mathcal{H}}{c}\varphi\partial_\nu\varphi - \frac{1}{c}\varphi'\partial_\nu\varphi\right) - \nabla^2\left(6\frac{\mathcal{H}^2}{c^2}\varphi^2 + \frac{3}{2c^2}\varphi'^2\right) , \tag{2.28}$$

$$\nabla^2\nabla^2\left(\frac{1}{c^2}h''^\alpha{}_\beta + \frac{2\mathcal{H}}{c^2}h'^\alpha{}_\beta - \nabla^2 h^\alpha{}_\beta\right) = 2\kappa^2a^2\left[\nabla^2\left(\nabla^2\mathcal{R}^\alpha{}_\beta - \partial^\alpha\partial_\nu\mathcal{R}^\nu{}_\beta - \partial_\beta\partial^\nu\mathcal{R}^\alpha{}_\nu\right) + \frac{1}{2}\left(\nabla^2\partial^\mu\partial_\nu\mathcal{R}^\nu{}_\mu\,\delta^\alpha{}_\beta + \partial^\alpha\partial_\beta\partial^\mu\partial_\nu\mathcal{R}^\nu{}_\mu\right)\right] , \tag{2.29}$$

where the traceless tensor $\mathcal{R}^\alpha{}_\beta$, Eq. (2.12), now reads

$$\mathcal{R}^\alpha{}_\beta = \rho\left(v^\alpha v_\beta - \frac{1}{3}v^2\,\delta^\alpha{}_\beta\right) - \frac{2}{\kappa^2a^2}\left(\partial^\alpha\varphi\,\partial_\beta\varphi - \frac{1}{3}\partial^\nu\varphi\,\partial_\nu\varphi\,\delta^\alpha{}_\beta\right) - \frac{4}{\kappa^2a^2}\left(\varphi\,\partial^\alpha\partial_\beta\varphi - \frac{1}{3}\varphi\,\nabla^2\varphi\,\delta^\alpha{}_\beta\right) , \tag{2.30}$$

while the trace part of the (α-β) component of Eq. (2.2) becomes

$$2\nabla^2(\phi-\psi) + 18\frac{\mathcal{H}}{c^2}\varphi' + 6\left(2\frac{\mathcal{H}'}{c^2} + \frac{\mathcal{H}^2}{c^2}\right)\varphi + \frac{6}{c^2}\varphi'' - 7\partial_\nu\varphi\partial^\nu\varphi - 8\varphi\nabla^2\varphi = \kappa^2a^2\rho\, v^2 . \tag{2.31}$$

Using Eqs. (2.19)-(2.22), and the expression $\phi_1 = \psi_1 = \varphi$, we can write the stress-energy tensor conservation equations $T^j_{i;j} = 0$ in a form that will give us the equations for our pressureless fluid in the first, second-order and PN regimes, respectively.

More specifically, the energy conservation equation reads

$$\rho' + 3\mathcal{H}\rho + \partial_\nu(\rho\, v^\nu) - \frac{3}{c}\rho\,\varphi' + \frac{1}{c^2}[(\rho\, v^2)' + \partial_\nu(v^\nu\rho\, v^2) + 4\mathcal{H}\rho\, v^2] - 2\rho\, v^\nu\partial_\nu\varphi - \frac{3}{c}\rho\,\psi_2' - \frac{6}{c}\rho\,\varphi\varphi' = 0 , \tag{2.32}$$

while the momentum conservation equation reads

$$(\rho v_\alpha)' + \partial_\nu (\rho v^\nu v_\alpha) + 4\mathcal{H} v_\alpha \rho + \rho c^2 \partial_\alpha \varphi - 16\mathcal{H}\rho v_\alpha \varphi + \frac{1}{c^2}\partial_\nu \left(\rho v^2 v^\nu v_\alpha\right) - 2\rho c^2 \varphi \partial_\alpha \varphi - \mathcal{H} c \rho V_\alpha$$
$$+ \rho c v_\nu \partial_\alpha V^\nu - 4\partial_\nu (\rho v^\nu v_\alpha \varphi) + \frac{4}{c^2}\mathcal{H}\rho v^2 v_\alpha - 4\rho' v_\alpha \varphi - 4\rho v'_\alpha \varphi - 6\rho v_\alpha \varphi' + \frac{1}{c^2}\left(v_\alpha \rho v^2\right)' - 2\rho v_\alpha v^\nu \partial_\nu \varphi$$
$$+ 2v^2 \rho \partial_\alpha \varphi + \rho c^2 \partial_\alpha \phi_2 = 0 \tag{2.33}$$

Eqs. (2.25), (2.26) and (2.28)-(2.29), together with Eqs. (2.24), (2.32) and (2.33), are the main result of this computation and represent a new set of equations which allow to describe the evolution of metric perturbation from the linear to the strongly non-linear stage in terms of the gravitational field φ, the matter density ρ and the peculiar velocity v^α.

2.3 Limiting forms of the hybrid approximation in different regimes

We now show how our approach accounts for known approximation schemes in different regimes.

2.3.1 The linear perturbative regime

Linearly perturbing Eqs. (2.24), (2.25) and (2.28) with respect to the FRW background we deduce that ϕ and ψ coincide and we obtain the linear scalar potential φ in terms of first-order density and velocity fluctuations,

$$\nabla^2 \nabla^2 \varphi = 4a^2 \pi G \left[\nabla^2 \delta\rho - 3\mathcal{H}\bar{\rho}\, \partial^\nu v_\nu\right] , \tag{2.34}$$

$$\nabla^2 (\mathcal{H}\varphi + \varphi') = -4a^2 \pi G \bar{\rho}\, \partial^\nu v_\nu . \tag{2.35}$$

Moreover, linearizing Eqs. (2.26), (2.29) and (2.31), using the linearized expressions for $\delta T^i{}_j$ we obtain

$$\varphi'' + 3\mathcal{H}\varphi' + (2\mathcal{H}' + \mathcal{H}^2)\varphi = 0 , \tag{2.36}$$

$$\nabla^2\nabla^2 V_\alpha = 0 \tag{2.37}$$

$$h''^{\alpha}_{\beta} + 2\mathcal{H}h'^{\alpha}_{\beta} - \nabla^2 h^{\alpha}{}_{\beta} = 0\ . \tag{2.38}$$

Perturbing to first order Eqs. (2.32) and (2.33), we recover also the linear continuity and momentum equations which read respectively:

$$\delta\rho' + 3\mathcal{H}\delta\rho + \bar{\rho}\,\partial_\nu v^\nu - 3\bar{\rho}\,\varphi' = 0\ , \tag{2.39}$$

$$v'^{\alpha} + \mathcal{H}v^\alpha + \partial^\alpha\varphi = 0. \tag{2.40}$$

In other words, we obtain all the results of linear perturbation theory (see e.g. Ref. [61, 62]), if we interpret φ as the linear scalar potential.

2.3.2 The second-order perturbative regime

On the other hand, selecting only the growing-mode solution of Eq. (2.36) and perturbing up to second order Eqs. (2.25)-(2.29), in the limit of a pressureless and irrotational fluid, we recover all the results of second-order perturbation theory [51, 46, 63].

More specifically, the first-order vector metric perturbations vanish, while the linear tensor metric perturbations are negligible for every kind of cosmological sources, thus we can safely neglect terms which can be expressed as products of first-order scalar and tensor metric perturbations. Writing $\varphi(\mathbf{x},\eta) = \varphi_0(\mathbf{x})g(\eta)$, where φ_0 is the peculiar gravitational potential linearly extrapolated to the present time and $g \equiv D_+/a$ is the so-called growth-suppression factor, where $D_+(\eta)$ is the linear growing-mode of density fluctuations in the Newtonian limit, and using the results of the previous sub-Section we obtain

$$\begin{aligned}\nabla^2\nabla^2\psi_s = -4\pi G a^2 \Big[3\mathcal{H}\left(\bar{\rho}\,\partial^\nu v_{s\,\nu} + \delta\rho\partial^\nu v_\nu + v_\nu\partial^\nu\delta\rho - 4\bar{\rho}\,\partial^\nu(\varphi v_\nu)\right) - 3\bar{\rho}\,\partial^\nu(\varphi' v_\nu) - \nabla^2(\delta\rho_s + \bar{\rho}v^2)\Big] \\ - \nabla^2\left(\frac{3}{2}\partial^\nu\varphi\partial_\nu\varphi + 4\varphi\nabla^2\varphi\right)\ ,\end{aligned} \tag{2.41}$$

$$\begin{aligned}\nabla^2\nabla^2\phi_s = -4\pi G a^2 \Big[3\mathcal{H}\left(\bar{\rho}\,\partial^\nu v_{s\,\nu} + \delta\rho\partial^\nu v_\nu + v_\nu\partial^\nu\delta\rho - 4\bar{\rho}\,\partial^\nu(\varphi v_\nu)\right) - 3\bar{\rho}\,\partial^\nu(\varphi' v_\nu) - \nabla^2(\delta\rho_s + 2\bar{\rho}\,v^2) \\ + 3\bar{\rho}\,\partial^\mu\partial_\nu(v^\nu v_\mu)\Big] + \frac{7}{2}\nabla^2(\partial_\nu\varphi\partial^\nu\varphi) - 3\partial_\nu\partial^\mu(\partial_\mu\varphi\partial^\nu\varphi)\ ,\end{aligned} \tag{2.42}$$

$$\nabla^2\nabla^2 V_\alpha = 16\pi G a^2 \partial^\nu \left(v_\nu \partial_\alpha \delta\rho - v_\alpha \partial_\nu \delta\rho\right) \ , \tag{2.43}$$

$$\nabla^2\nabla^2 \left(h''^{\,\alpha}{}_\beta + 2\mathcal{H} h'^{\,\alpha}{}_\beta - \nabla^2 h^\alpha{}_\beta\right) = 16\pi G a^2 \left[\nabla^2\left(\nabla^2 \mathcal{R}^\alpha{}_\beta - \partial^\alpha \partial_\nu \mathcal{R}^\nu{}_\beta - \partial_\beta \partial^\nu \mathcal{R}^\alpha{}_\nu\right) + \frac{1}{2}\left(\nabla^2 \partial^\mu \partial_\nu \mathcal{R}^\nu{}_\mu\, \delta^\alpha{}_\beta + \partial^\alpha \partial_\beta \partial^\mu \partial_\nu \mathcal{R}^\nu{}_\mu\right)\right] \ , \tag{2.44}$$

where $R^\alpha{}_\beta$ has the same analytic form of Eq. (2.30), that is

$$\mathcal{R}^\alpha{}_\beta = \rho\left(v^\alpha v_\beta - \frac{1}{3} v^2\, \delta^\alpha{}_\beta\right) - \frac{1}{4\pi G a^2}\left(\partial^\alpha\varphi\, \partial_\beta\varphi - \frac{1}{3}\partial^\nu\varphi\, \partial_\nu\varphi\, \delta^\alpha{}_\beta\right) - \frac{1}{2\pi G a^2}\left(\varphi\, \partial^\alpha\partial_\beta\varphi - \frac{1}{3}\varphi\, \nabla^2\varphi\, \delta^\alpha{}_\beta\right) \ , \tag{2.45}$$

The subscript s indicates quantities evaluated at the second perturbative order, v_s^α is the velocity $dx^\alpha/d\eta$ perturbed at the second-order and is related to the second-order spatial part $v^\alpha_{(2)}/a$ of the 4-velocity by the relation $v^\alpha_{(2)} = v_s^\alpha - \varphi v^\alpha$ [2].

We can also find the equations that describe the evolution of $\delta\rho_s$ and v_s^α by perturbing up to second order Eqs. (2.32)-(2.33) and taking the divergence of the latter. In this way we recover also the second-order energy continuity equation

$$\delta\rho_s' + 3\mathcal{H}\delta\rho_s + \bar\rho\partial_\nu v_s^\nu + \delta\rho\partial_\nu v^\nu + v^\nu\partial_\nu\delta\rho + \mathcal{H}\bar\rho v^2 + \bar\rho(v^2)' - 3\delta\rho\varphi' - 3\bar\rho\psi_s' - 6\bar\rho\varphi\varphi' - 2\bar\rho v^\mu\partial_\mu\varphi = 0 \ , \tag{2.46}$$

and the divergence of the second-order momentum conservation equation

$$\mathcal{H}\bar\rho\,\partial^\alpha v_{s\alpha} + \bar\rho\,\partial^\alpha v'_{s\alpha} + \bar\rho\,\nabla^2\phi_s + \partial^\alpha\big[4\mathcal{H}\delta\rho v_\alpha - 4\mathcal{H}\bar\rho\,\varphi v_\alpha + \delta\rho' v_\alpha + \delta\rho v'_\alpha - 4\bar\rho\,\varphi v'_\alpha - 6\bar\rho\,\varphi' v_\alpha + \delta\rho\partial_\alpha\varphi - 2\bar\rho\,\varphi\partial_\alpha\varphi + \bar\rho\,\partial_\nu(v^\nu v_\alpha)\big] = 0 \ . \tag{2.47}$$

2.3.3 The Newtonian approximation

From Eqs. (2.23) and (2.25) up to $\mathcal{O}(1/c^2)$ we deduce

$$\nabla^2\psi_1 = \nabla^2\phi_1 = \nabla^2\varphi = \frac{4\pi G a^2}{c^2}\delta\rho \ , \tag{2.48}$$

[2] It is worth noting that the traceless tensor $\mathcal{R}^\alpha{}_\beta$ in Eq. (2.45) differs from the correspondent tensor in Eq. (13) of [46]. Besides the global $4\pi G a^2$ factor, the terms containing the gravitational potential φ are not the same in the two cases. Actually, what is important is the transverse and traceless part of the gravitational wave sources, and they happen to be the same, since, as we will show later, our Eq. (2.45) can be written in the form of Eq. (13) in [46] plus other terms which do not contribute to the relevant component of the source (see Eq. (2.67) and (2.68)).

and writing $\varphi \equiv \varphi_N/c^2$, we recover the Poisson equation $\nabla^2\varphi_N = 4\pi G a^2 \delta\rho$, where the subscript N stands for *Newtonian*.

Analogously, to leading order in $1/c$, Eqs. (2.32) and (2.33) respectively become the usual continuity and Euler equations of Newtonian cosmology which apply in the limit of weak fields and non-relativistic velocities [43]

$$\rho' + 3\mathcal{H}\rho + \partial_\nu(\rho\, v^\nu) = 0 \,, \tag{2.49}$$

$$v'_\alpha + \mathcal{H} v_\alpha + v_\nu \partial^\nu v_\alpha = -\partial_\alpha \varphi_N \,. \tag{2.50}$$

The latter equation was obtained taking Eq. (2.33) up to $\mathcal{O}(1/c^0)$ and inserting Eq. (2.49).

In the linear limit Eqs. (2.48)-(2.50) become

$$\nabla^2\varphi = 4\pi G a^2 \delta\rho \,, \tag{2.51}$$

$$\delta\rho' + 3\mathcal{H}\delta\rho + \bar{\rho}\partial_\nu v^\nu = 0 \,, \tag{2.52}$$

$$v'_\alpha + \mathcal{H} v_\alpha = -\partial_\alpha \varphi_N \,. \tag{2.53}$$

As we can observe, the equations which characterize the linearized Newtonian theory, differ from the linearized relativistic ones. In particular, while the momentum conservation Eqs. (2.40) and (2.53) are identical, the linear energy density conservation Eq. (2.39) differs from the Newtonian one, Eq. (2.52), by the extra term $-3\bar{\rho}\varphi'$ which does not vanish, even for the pure growing-mode solution of Eq. (2.36), owing to the presence of a cosmological constant contribution to the FRW background.

Moreover, Eq. (2.34) represents the linear relativistic generalization of the Poisson equation, since it includes the contribution of the so-called *longitudinal momentum density* φ_f ($\partial_\nu\varphi_f = -4a^2\pi G\bar{\rho}v_\nu$) which acts as a source term for the linear potential φ. Thus, the Poisson gauge gives the *relativistic* cosmological generalization of *Newtonian* gravity [43].

2.3.4 The highly non-linear regime in the PN approximation

Finally, we consider the case of cosmic structures, in the highly non-linear regime, whose size is much larger than their Schwarzschild radius (in order to avoid non-Newtonian terms in the expressions of the sources).

Our sources can generate vector and tensor metric perturbations by mode-mixing in the non-linear regime. In particular, this mechanism applies to dark-matter haloes around galaxies and galaxy clusters or, more specifically, to the highly condensed sub-structures by which these haloes are characterized.

We obtain the continuity and momentum equations up to $\mathcal{O}(1/c^2)$, the equation describing the evolution of the (0-0) component of the metric (2.1) up to $\mathcal{O}(1/c^4)$, and the equation for the vector modes V_α up to $\mathcal{O}(1/c^3)$, i.e. their 1PN approximation. Moreover, we describe the scalar mode of the (α-β) component of the metric (2.1) up to $\mathcal{O}(1/c^4)$, i.e. we consider its second post-Newtonian (2PN) approximation, while we obtain the leading-order terms in powers of $1/c$ for the source of the tensor modes $h^\alpha{}_\beta$.

Eqs. (2.25)-(2.29) in this limit become

$$\nabla^2\nabla^2\psi = \frac{4\pi G a^2}{c^2}\nabla^2\delta\rho + \frac{4\pi G a^2}{c^4}\left[\nabla^2(\rho\, v^2) - 3\mathcal{H}\partial^\nu(v_\nu\rho)\right] - \frac{1}{c^4}\nabla^2\left(\frac{3}{2}\partial^\nu\varphi_N\partial_\nu\varphi_N + 4\varphi_N\nabla^2\varphi_N\right) , \tag{2.54}$$

$$\nabla^2\nabla^2\phi = \frac{4\pi G a^2}{c^2}\nabla^2\delta\rho + \frac{4\pi G a^2}{c^4}\left[2\nabla^2(\rho\, v^2) - 3\mathcal{H}\partial^\nu(v_\nu\rho) - 3\partial^\mu\partial_\nu(\rho\, v^\nu v_\mu)\right] + \frac{7}{2c^4}\nabla^2(\partial_\nu\varphi_N\partial^\nu\varphi_N) - \frac{3}{c^4}\partial_\nu\partial^\mu(\partial_\mu\varphi_N\partial^\nu\varphi_N) , \tag{2.55}$$

$$\nabla^2\nabla^2 V_\alpha = \frac{16\pi G a^2}{c^3}\left[\partial_\alpha\partial^\nu(v_\nu\rho) - \nabla^2(v_\alpha\rho)\right] , \tag{2.56}$$

$$\nabla^2\nabla^2\left(\frac{1}{c^2}h'^{\prime\,\alpha}{}_\beta + \frac{2\mathcal{H}}{c^2}h'^{\,\alpha}{}_\beta - \nabla^2 h^\alpha{}_\beta\right) = \frac{16\pi G a^2}{c^4}\left[\nabla^2\left(\nabla^2\mathcal{R}^\alpha{}_\beta - \partial^\alpha\partial_\nu\mathcal{R}^\nu{}_\beta - \partial_\beta\partial^\nu\mathcal{R}^\alpha{}_\nu\right) + \frac{1}{2}\left(\nabla^2\partial^\mu\partial_\nu\mathcal{R}^\nu{}_\mu\,\delta^\alpha{}_\beta + \partial^\alpha\partial_\beta\partial^\mu\partial_\nu\mathcal{R}^\nu{}_\mu\right)\right] , \tag{2.57}$$

where the post-Newtonian limit of the traceless tensor $\mathcal{R}^\alpha{}_\beta$ is

$$\mathcal{R}^\alpha{}_\beta = \rho\left(v^\alpha v_\beta - \frac{1}{3}v^2\,\delta^\alpha{}_\beta\right) - \frac{1}{4\pi G a^2}\left(\partial^\alpha\varphi_N\,\partial_\beta\varphi_N - \frac{1}{3}\partial^\nu\varphi_N\,\partial_\nu\varphi_N\,\delta^\alpha{}_\beta\right) - \frac{1}{2\pi G a^2}\left(\varphi_N\,\partial^\alpha\partial_\beta\varphi_N - \frac{4\pi G a^2}{3}\varphi_N\,\delta\rho\,\delta^\alpha{}_\beta\right) . \tag{2.58}$$

Since, in order to compute the metric coefficients up to the PN approximation, we only need the terms in $\delta T^{i}{}_{j}$ which satisfy the Newtonian equations of motions, in Eq (2.58) we have inserted the Poisson equation. The 1PN extensions of the Newtonian continuity and Euler equations respectively read

$$\rho' + 3\mathcal{H}\rho + \partial_\nu(\rho v^\nu) + \frac{1}{c^2}\left[(\rho v^2)' + \partial_\nu(v^\nu \rho v^2) + 4\mathcal{H}\rho v^2 - 2\rho v^\nu \partial_\nu \varphi_N\right] = 0\,, \tag{2.59}$$

$$\begin{aligned}
&\rho\,(v_\alpha' + \mathcal{H}v_\alpha + v_\nu \partial^\nu v_\alpha + \partial_\alpha \varphi_N) + \frac{1}{c^2}\Big[-4\rho' v_\alpha \varphi_N - 4\rho\, v_\alpha' \varphi_N - 6\rho\, v_\alpha \varphi_N' + \left(v_\alpha \rho v^2\right)' - 2\rho\, v_\alpha v^\nu \partial_\nu \varphi_N \\
&+ 2v^2 \rho\, \partial_\alpha \varphi_N + \rho\, \partial_\alpha \phi_{PN} - 2\rho\, \varphi_N \partial_\alpha \varphi_N - \mathcal{H}\rho\, V_\alpha + \rho\, v_\nu \partial_\alpha V_\nu - 16\mathcal{H}\rho\, v_\alpha \varphi_N - 4\partial_\nu\left(\rho\, v^\nu v_\alpha \varphi_N\right) \\
&+ \partial_\nu\left(\rho\, v^2 v^\nu v_\alpha\right) + 4\mathcal{H}\rho\, v^2 v_\alpha\Big] = 0\,,
\end{aligned} \tag{2.60}$$

where ϕ_{PN} is given by the 1PN part of Eq. (2.55). It can be worth noting that the sources of the metric coefficients involve only quantities of Newtonian origin, i.e. they do not contain terms defined in higher-order approximations.

To conclude this sub-Section, let us stress that all the PN expressions derived here were presented for the first time in [53], as they are derived in a different gauge than the usual post-Newtonian [39, 40, 57, 64], or synchronous and comoving one [42].

2.4 Vector and tensor modes

It can be worth to observe that, in the linear limit, Eq. (2.31) becomes

$$\varphi_N'' + 3\mathcal{H}\varphi_N' + (2\mathcal{H}' + \mathcal{H}^2)\varphi_N = 0\,. \tag{2.61}$$

This result is extremely important since it implies that the Newtonian potential φ_N and the linear potential φ evolve in the same way with time. Eq. (2.61) can be also obtained by mixing together the Newtonian continuity, Euler and Poisson equations perturbed at first order. This means that, starting from the same initial conditions, i.e. from the same primordial potential as given e.g. by inflation, the two linear potentials φ_N/c^2 and φ will assume the same values in each point and at each time. In other words, Eq. (2.61) implies that, in the case of first-order matter perturbations, it is sufficient to use Newtonian gravity on all scales, provided that we define a "Newtonian" linear density perturbation $\delta\rho_N$ via the Poisson equation applied to the linear relativistic potential φ, even if $\delta\rho_N$ differs from the relativistic density $\delta\rho$, as given by Eq. (2.34). The previous considerations allow to conclude that, for pure growing-mode solutions of Eq. (2.61), in

the case of an irrotational and pressureless fluid, Eqs. (2.56)-(2.58) apply to all cosmologically relevant scales, i.e. from super-horizon to the smallest ones, even if the density ρ, the velocity v^α and the potential φ are required to follow the usual Newtonian hydrodynamical equations. In the equations that follow, therefore, we will drop the subscript N on the various quantities and write

$$\nabla^2\varphi = 4\pi G a^2 \delta\rho \,, \tag{2.62}$$

$$\rho' + 3\mathcal{H}\rho + \partial_\nu(\rho\, v^\nu) = 0 \,, \tag{2.63}$$

$$v'_\alpha + \mathcal{H} v_\alpha + v_\nu \partial^\nu v_\alpha = -\partial_\alpha \varphi \,. \tag{2.64}$$

Thus, for the vector modes we have

$$\nabla^2\nabla^2 V_\alpha = \frac{16\pi G a^2}{c^3}\left[\partial_\alpha\partial^\nu(v_\nu\rho) - \nabla^2(v_\alpha\rho)\right] \,, \tag{2.65}$$

and, for the tensor modes,

$$\begin{aligned}\nabla^2\nabla^2\left(\frac{1}{c^2}h''^{\,\alpha}{}_\beta + \frac{2\mathcal{H}}{c^2}h'^{\,\alpha}{}_\beta - \nabla^2 h^\alpha{}_\beta\right) &= \frac{16\pi G a^2}{c^4}\big[\nabla^2\big(\nabla^2\mathcal{R}^\alpha{}_\beta - \partial^\alpha\partial_\nu\mathcal{R}^\nu{}_\beta - \partial_\beta\partial^\nu\mathcal{R}^\alpha{}_\nu\big) \\ &+ \frac{1}{2}\left(\nabla^2\partial^\mu\partial_\nu\mathcal{R}^\nu{}_\mu\,\delta^\alpha{}_\beta + \partial^\alpha\partial_\beta\partial^\mu\partial_\nu\mathcal{R}^\nu{}_\mu\right)\big] = \frac{16\pi G a^2}{c^4}\nabla^2\nabla^2\left(\mathcal{P}^\alpha{}_\nu\mathcal{P}^\mu{}_\beta - \frac{1}{2}\mathcal{P}^\alpha{}_\beta\mathcal{P}^\mu{}_\nu\right)\mathcal{R}^\nu{}_\mu \,,\end{aligned} \tag{2.66}$$

where

$$\begin{aligned}&\mathcal{R}^\alpha{}_\beta = \\ &\rho\left(v^\alpha v_\beta - \frac{1}{3}v^2\,\delta^\alpha{}_\beta\right) - \frac{1}{4\pi G a^2}\left(\partial^\alpha\varphi\,\partial_\beta\varphi - \frac{1}{3}\partial^\nu\varphi\,\partial_\nu\varphi\,\delta^\alpha{}_\beta\right) - \frac{1}{2\pi G a^2}\left(\varphi\,\partial^\alpha\partial_\beta\varphi - \frac{4\pi G a^2}{3}\varphi\,\delta\rho\,\delta^\alpha{}_\beta\right) = \\ &\rho\left(v^\alpha v_\beta - \frac{1}{3}v^2\,\delta^\alpha{}_\beta\right) + \frac{1}{4\pi G a^2}\left(\partial^\alpha\varphi\,\partial_\beta\varphi - \frac{1}{3}\partial^\nu\varphi\,\partial_\nu\varphi\,\delta^\alpha{}_\beta\right) - \frac{1}{2\pi G a^2}\left[\partial^\alpha(\varphi\partial_\beta\varphi) - \frac{1}{3}\partial^\nu(\varphi\partial_\nu\varphi)\,\delta^\alpha{}_\beta\right] \,,\end{aligned} \tag{2.67}$$

which represent a very important result, since these equations imply that, in the case of matter perturbations, the Newtonian description of the sources of vector and tensor metric fluctuations can take into account all the effects of the relativistic second-order perturbation theory.

It is important to stress that the third term on the last line of Eq. (2.67) does not contribute to the source of gravitational waves since it vanishes after applying the projection operation in Eq. (2.13); thus we are allowed to drop it and define as effective source of the gravitational wave $h^{\alpha}{}_{\beta}$ the traceless tensor

$$\mathcal{R}^{\alpha}_{\mathrm{eff}\,\beta} = \rho\left(v^{\alpha}v_{\beta} - \frac{1}{3}v^2\,\delta^{\alpha}{}_{\beta}\right) + \frac{1}{4\pi G a^2}\left(\partial^{\alpha}\varphi\,\partial_{\beta}\varphi - \frac{1}{3}\partial^{\nu}\varphi\,\partial_{\nu}\varphi\,\delta^{\alpha}{}_{\beta}\right) . \tag{2.68}$$

Actually from a post-Newtonian point of view, these equations hold true also for a pressureless fluid with a vorticity contribution to the peculiar velocity v^{α}, but the reader should not be surprised if curl terms can be produced even by a pressureless and irrotational perfect fluid. In fact, the curl of the quantity ρv^{α} is still non-vanishing, even if v^{α} is derived from a scalar potential.

2.4.1 Comparison with the quadrupole radiation

We want to show how the gravitational wave source $\mathcal{R}^{\alpha}_{\mathrm{eff}\,\beta}$ in Eq. (2.68) includes the contribution by the reduced quadrupole moment [60] of the matter distribution expressed via comoving coordinates:

$$\mathcal{Q}^{\alpha}{}_{\beta} = \int d^3\tilde{x}\,\rho\left(\tilde{x}^{\alpha}\tilde{x}_{\beta} - \frac{1}{3}\tilde{x}^{\nu}\tilde{x}_{\nu}\,\delta^{\alpha}{}_{\beta}\right) . \tag{2.69}$$

First of all, let us choose the origin of our coordinates O inside the mass-energy distribution described by the stress-energy tensor $\delta T^{i}{}_{j}$. Let $\mathbf{x}$ be the vector from O to the observation point P and $\tilde{\mathbf{x}}$ the vector from O to the volume element $d^3\tilde{x}$. On scales well inside the Hubble horizon, the solution of Eq. (2.66), augmented by an outgoing-wave boundary condition, is

$$h^{\alpha}{}_{\beta}(\eta,\mathbf{x}) = \frac{4G}{ac^4}\mathcal{P}^{\alpha}{}_{\nu}{}^{\mu}{}_{\beta}\int d^3\tilde{x}\frac{(a^3\mathcal{R}^{\nu}_{\mathrm{eff}\,\mu})_{ret}}{|\mathbf{x}-\tilde{\mathbf{x}}|} , \tag{2.70}$$

where the transverse-traceless operator is $\mathcal{P}^{\alpha}{}_{\nu}{}^{\mu}{}_{\beta} \equiv \mathcal{P}^{\alpha}{}_{\nu}\mathcal{P}^{\mu}{}_{\beta} - \frac{1}{2}\mathcal{P}^{\alpha}{}_{\beta}\mathcal{P}^{\mu}{}_{\nu}$, with $\mathcal{P}^{\alpha}{}_{\beta}$ given by Eq. (2.13) and $\mathcal{R}^{\alpha}_{\mathrm{eff}\,\beta}$ by Eq. (2.68). The subscript "ret" means the quantity is to be evaluated at the retarded space-time point $(\eta - |\mathbf{x}-\tilde{\mathbf{x}}|/c, \tilde{\mathbf{x}})$.

Our purpose is to evaluate $h^{\alpha}{}_{\beta}$ in the wave-zone, that is far outside the source region: $|\mathbf{x}| \equiv r \gg |\tilde{\mathbf{x}}|$, thus we expand the retarded integral Eq. (2.70) in powers of $\tilde{\mathbf{x}}/r$ and take only the first term of the multipole expansion

$$h^{\alpha}{}_{\beta}(\eta,\mathbf{x}) = \frac{4G}{c^4}\frac{1}{ar}\mathcal{P}^{\alpha}{}_{\nu}{}^{\mu}{}_{\beta}\left[a^3\int d^3\tilde{x}\,\mathcal{R}^{\nu}_{\mathrm{eff}\,\mu}\right]_{ret} , \tag{2.71}$$

where for radially travelling waves $\mathcal{P}^{\alpha}{}_{\beta} = \delta^{\alpha}{}_{\beta} - x^{\alpha}x_{\beta}/r^2$. Eq. (2.71) expresses the gravitational waves $h^{\alpha}{}_{\beta}$ in terms of integrals over the "stress distribution" $\mathcal{R}^{\alpha}_{\mathrm{eff}\,\beta}$, while Eq. (2.69) represents an integral over the source "energy distribution". In order to make the comparison between these two equations, we need to convert the spatial components $T^{\alpha}{}_{\beta}$ of the stress-energy tensor in terms of the time components by means of the conservation equations $T^{j}_{i;j} = 0$. Since $\mathcal{Q}^{\alpha}{}_{\beta}$ in Eq. (2.69) is the Newtonian quadrupole and the dynamics of the tensor source is also Newtonian, we only need the continuity and Euler Eq. (2.63)-(2.64), by which, after some mathematical manipulations, we obtain

$$\int d^3\tilde{x}\,(\rho\, v^{\alpha}v_{\beta}) = \frac{1}{2}\frac{\partial}{\partial\eta}\int d^3\tilde{x}\,\rho\,(\tilde{x}^{\alpha}v_{\beta} + \tilde{x}_{\beta}v^{\alpha}) + 2\mathcal{H}\int d^3\tilde{x}\,\rho\,(\tilde{x}^{\alpha}v_{\beta} + \tilde{x}_{\beta}v^{\alpha}) + \frac{1}{2}\int d^3\tilde{x}\,\rho\,(\tilde{x}^{\alpha}\partial_{\beta}\varphi + \tilde{x}_{\beta}\partial^{\alpha}\varphi)\ , \tag{2.72}$$

and

$$\int d^3\tilde{x}\,\rho\,(\tilde{x}^{\alpha}v_{\beta} + \tilde{x}_{\beta}v^{\alpha}) = \frac{\partial}{\partial\eta}\int d^3\tilde{x}\,(\rho\,\tilde{x}^{\alpha}\tilde{x}_{\beta}) + 3\mathcal{H}\int d^3\tilde{x}\,(\rho\,\tilde{x}^{\alpha}\tilde{x}_{\beta})\ , \tag{2.73}$$

where we have dropped surface terms at infinity.

By substituting Eq. (2.73) into Eq. (2.72), we finally find

$$\int d^3\tilde{x}\,(\rho\, v^{\alpha}v_{\beta}) = \frac{1}{2}\frac{\partial^2}{\partial\eta^2}\int d^3\tilde{x}\,(\rho\,\tilde{x}^{\alpha}\tilde{x}_{\beta}) + \frac{3}{2}\frac{\partial}{\partial\eta}\int d^3\tilde{x}\,\mathcal{H}(\rho\,\tilde{x}^{\alpha}\tilde{x}_{\beta}) + 2\mathcal{H}\int d^3\tilde{x}\,\rho\,(\tilde{x}^{\alpha}v_{\beta} + \tilde{x}_{\beta}v^{\alpha}) - \frac{1}{2}\int d^3\tilde{x}\,\rho\,(\tilde{x}^{\alpha}\partial_{\beta}\varphi + \tilde{x}_{\beta}\partial^{\alpha}\varphi)\ . \tag{2.74}$$

After substituting Eq. (2.74) into Eq. (2.68) and using again the continuity equation, in the wave zone the gravitational wave $h^{\alpha}{}_{\beta}$, to leading order in powers of $1/c$ and $\tilde{\mathbf{x}}/r$, reads

$$h^{\alpha}{}_{\beta}(\eta,\mathbf{x}) = \frac{2G}{ar\,c^4}\mathcal{P}^{\alpha}{}_{\nu}{}^{\mu}{}_{\beta}\left\{a^3\left[\frac{\partial^2\mathcal{Q}^{\nu}{}_{\mu}}{\partial\eta^2} + 7\mathcal{H}\frac{\partial\mathcal{Q}^{\nu}{}_{\mu}}{\partial\eta} + \left(3\mathcal{H}' + 12\mathcal{H}^2\right)\mathcal{Q}^{\nu}{}_{\mu}\right.\right. \\ \left.\left. - \int d^3\tilde{x}\,\rho\left(\tilde{x}^{\nu}\partial_{\mu}\varphi + \tilde{x}_{\mu}\partial^{\nu}\varphi - \frac{2}{3}\tilde{x}^{\sigma}\partial_{\sigma}\varphi\,\delta^{\nu}{}_{\mu}\right) + \frac{1}{2\pi Ga^2}\int d^3\tilde{x}\,\left(\partial^{\nu}\varphi\,\partial_{\mu}\varphi - \frac{1}{3}\partial^{\sigma}\varphi\,\partial_{\sigma}\varphi\,\delta^{\nu}{}_{\mu}\right)\right]\right\}_{ret}\ . \tag{2.75}$$

Let us observe that the first line of Eq. (2.75) recovers the known expression of the quadrupole radiation in the limit of a flat and static Universe [60, 65], while contributions on the second line derive from the back-reaction of the gravitational potential φ which can act as a source of gravitational waves. Moreover, on scales much smaller than the Hubble horizon, the last two terms on the first line in Eq. (2.75) can be neglected

in comparison to the first one. In fact, the typical free fall-time of a mass distribution is proportional to $\rho^{-1/2}$, while the Hubble time goes as $\rho_b^{-1/2}$, where "b" stands for background; thus, on small scales, where the density contrasts can be very high, the characteristic rate of the structure collapse is much larger than the expansion rate. This allows to drop the contributions proportional to $\mathcal{H}$ in Eq. (2.75) and recover the results expected well inside the horizon.

The main results of this Chapter so far are represented by the set of equations (2.25), (2.26), (2.28)-(2.30) and (2.68) , expressing metric perturbation in terms of the gravitational field φ, where the matter density ρ and the peculiar velocity v^α, satisfy Eqs. (2.24), (2.32) and (2.33). These equations, when applied in a cosmological setting characterized by a pressureless and irrotational fluid and a cosmological constant, provide a unified description of cosmological perturbations during their evolution from the linear to the highly non-linear regime. On large scales, these equations reduce to the equations of the first and second-order perturbation theory developed in the Poisson gauge, while, on very small scales, where the perturbative approach is no longer applicable, they describe the evolution of cosmological perturbations by a PN approximation. Indeed, we calculate the (0-0) and (0-α) components of the metric (2.1) up to the 1PN order, the (α-β) scalar-type component up to the 2PN order, while we find for the (α-β) tensor-type component the leading-order source terms in powers of $1/c$.

We also derived the generalization of the standard Euler-Poisson system of equations of Newtonian hydrodynamics, that consistently accounts for all the effects up to order $1/c^2$. The curl term and anisotropic stress, that produce vectors and tensor metric perturbations, arise already at the second perturbative order and at the strongly non-linear level they are dominated by the contribution of the high-density contrast and the high peculiar velocity typical of small-scale structures. It can be worth to stress that the quantities which source vector and tensor modes are of Newtonian origin on all scales, in the sense that they involve only terms that satisfy the Newtonian Euler-Poisson system. This result is of extreme importance in view of a possible numerical implementation of our set of equations, as it implies that one can compute directly vector and tensor modes starting from the outputs of N-body simulations.

Finally, it should be stressed that the set of equations, exposed here and in Ref. [53], has many possible cosmological applications such as, for example, the evaluation of the stochastic gravitational-wave backgrounds produced by CDM haloes [66, 67, 68, 56] and substructures within haloes. As we show in Sec. 2.6 and following, it can be also used

to improve the estimate of gravitational lensing effects and gravity-induced secondary CMB temperature/polarization anisotropies generated by small-scale structures [44, 45, 46].

2.5 Sources of gravitational radiation

Sources of gravitational waves (GW) are commonly separated in two types: astrophysical and cosmological.

The first kind can produce a stochastic background which provides interesting information on the distribution of compact objects at relatively low redshifts, such as star formation and supernova rates, black-hole growth mechanisms and other important phenomena. Such a background is generated by neutron stars, black holes and the associated binary systems, which emit in the frequency range $\nu_e \approx 10^2 - 10^4$Hz. (e.g [69, 73]), or by galactic merging of unresolved binary white dwarfs with frequencies in the range $\nu_e \approx 10^{-4} - 10^{-2}$Hz [74, 75, 76, 77, 78].

Besides binary systems of super-massive black holes in the galaxy center, which could emit at $\nu_e \approx 10^{-4}$Hz, hence detectable by LISA (*e.g.* Ref. [79]), the principal example of gravitational waves of cosmological origin is represented by the relic radiation which has been generated by quantum fluctuations of the metric tensor during the inflationary era. The detection of this relic background would shed light on the physics of the very early Universe, since its strain amplitude is proportional to the square of the inflation energy scale. Primordial backgrounds can be generated by various mechanisms and are characterized by a large frequency interval which extends from a few 10^{-18} Hz to a few GHz, allowing their detection by markedly different ways of observation [69] (see Fig 2.1).

One of the best strategies for detecting the relic gravitational radiation is to exploit the imprints it leaves on the Cosmic Microwave Background (CMB) temperature anisotropy and polarization [80, 81, 82]. More specifically, the CMB photons are very sensitive to primordial GWs with frequencies $\approx 10^{-17}$Hz, which correspond to the comoving size of the Hubble radius at last scattering, when tensor metric modes, being damped by the horizon entering, produce the largest amount of temperature quadrupole anisotropy and, consequently, by Thomson scattering, the largest amount of polarization [83]. As will be shown in Chatper 3, the primary B-mode component in the polarization pattern is excited by vector and tensor cosmological perturbations

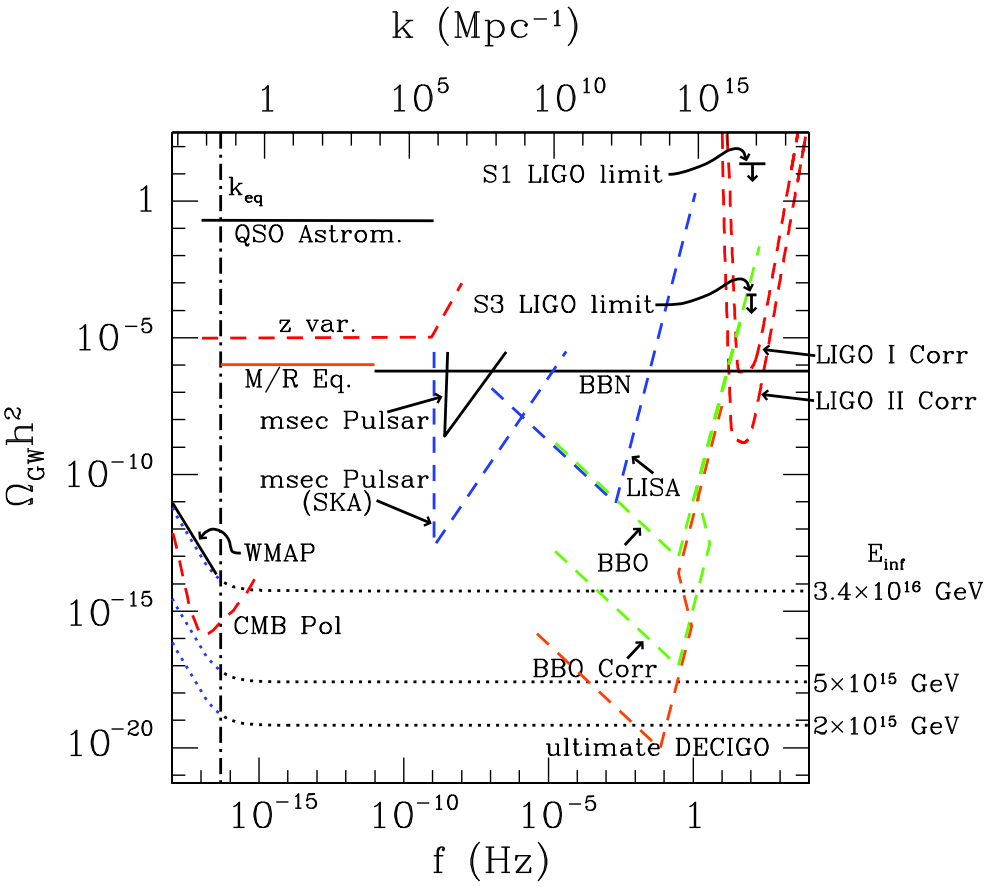

Figure 2.1: *Current limits and projected sensitivities to the energy density $h^2\Omega_g w$ (see Eq. 2.101) of a stochastic gravitational-wave background versus the gravitational-wave frequency. The solid curves all indicate current upper limits, while the various broken curves indicate projected sensitivities. The "M/R" line comes from CMB constraints to the epoch of matter-radiation equality [70]. Curves corresponding to scale-invariant gravitational-wave backgrounds are shown (dotted curves), labeled by the associated inflationary energy scales. The amplitude of CMB temperature fluctuations currently constrains this value to be below 3.36×10^{16} GeV, but only at frequencies $f < 10^{-16}$ Hz. Future CMB measurements may be able to reach energy scales near 10^{15} GeV at these frequencies. The "QSO Astrom" curve is a limit from quasar astrometry, and the "z var" is a forecast for future redshift measurements. The S1 and S3 points are upper limits from the Laser Interferometric Gravitational Wave Observatory (LIGO) [71] and the other curves are forecasts for future LIGO sensitivities. The LISA curve shows forecasts for the future NASA/ESO Laser Interferometric Space Observatory and the BBO and DECIGO curves show forecasts for sensitivities for two space-based observatories now under study (the "Corr" designation is for a configuration in which the signals from two detectors or detector arrays are correlated against one another—e.g., for LIGO, if the signals from the Hanford and Louisiana sites are correlated). The two "pulsar" curves show current and future (from the Square Kilometer Array; SKA) sensitivities from pulsar timing. The WMAP and "CMB Pol" curves show the current upper limit from WMAP and the sensitivity forecast for CMBPol, a satellite mission now under study. From Ref. [72].*

only; therefore, if initial fluctuations are created very early, *e.g.* during inflation so that the vector growth is damped, *primary* B-modes can be produced only by tensor perturbations and, therefore, a possible detection will represent the incontrovertible proof of their existence [84, 85, 86].

Unfortunately, there are mechanisms that can produce *secondary* B-modes, the principal one being represented by the Cosmic Shear (CS) [181], which distorts the primary CMB pattern, in particular converting E- into B-modes [87] (see Chapter 4). Luckily, although comparable, B-modes from primordial GW exhibit their peak at multipoles $l \approx 100$, corresponding to the degree scale, while, for lensed B-modes, the peak is at $l \approx 1000$, corresponding to the arcminute scale. Nonetheless, if the energy scale of inflation is $V^{1/4} \leq 2 - 4 \times 10^{15}$GeV, the CS-induced curl is a foreground for the $l \approx 50 - 100$ primordial GW-induced B-polarization. This important contamination has to be removed in order to detect relic gravitational waves [88, 89].

Actually, besides gravitational lensing, for cosmological models which constantly seed fluctuations in the geometry, *e.g.* topological defects, vector metric perturbations can be huge and can produce non-negligible effects on the CMB photons as, in particular, B-mode polarization, unlike to what happens in inflationary models [90]. On the other hand, no relevant contribution from these objects is indicated by the modern cosmological probes.

In what follows, we will be interested in the cosmological stochastic GW background produced by CDM haloes via power transfer from scalar and possible vector perturbations to tensor metric modes, during the strongly non-linear stage of their evolution [53]. It differs from other cosmological backgrounds, as that produced during the mildly non-linear stage [68], since density and velocity fields can be, in this case, highly non-linear.

Since the non-linear evolution of CDM haloes occurs on a cosmological timescale, the produced gravitational radiation may be relevant at frequencies comparable to those of the primordial GW which affect the CMB photons and, therefore, can produce secondary CMB anisotropy and polarization, expecially B-modes, that could represent a foreground for the detection of the relic radiation.

Moreover, as for the case of black holes and neutron stars, the analysis of the stochastic background produced by highly non-linear cosmic structures, could bring information on their distribution, evolution, shape and composition, shedding light on many open issues.

2.6 CDM Halo-induced Gravitational Radiation: basic equations

Adopting the mathematical formalism developed in Sec.2.4, in the following part of this Chapter we estimate the amount and frequency distribution of gravitational waves from cosmic structures, following their evolution from the linear to the highly non-linear level. More specifically, the evaluation of this gravitational radiation is possible on scales much larger than the Schwarzschild radius of collapsing bodies, by means of the "hybrid approximation" [53] of the Einstein field equations, which mixes post-Newtonian (PN) and second-order perturbative techniques (*e.g.* to deal with the perturbations of matter and geometry. This approach gives a more accurate description of gravitational waves generated by non-linear CDM structures than the standard second-order perturbation theory [68], which can only account for small deviations from the linear regime, or the Newtonian quadrupole radiation [60, 65]; indeed, it upgrades the weak-field limit of Einstein equations to account for PN scalar and vector metric perturbations and for leading-order source terms of metric tensor modes. It provides, on small scales, a PN approximation to the source of gravitational radiation, and, on large scales, it converges to the first and second-order perturbative equations, but still describing, on all the cosmologically relevant scales, the dynamics of the involved CDM structures by means of the standard Newtonian Poisson, Euler and continuity equations (*e.g.* [38])

$$\nabla^2\varphi = 4\pi G a^2 \delta\rho \,, \tag{2.76}$$

$$\rho' + 3\mathcal{H}\rho + \partial_\nu(\rho v^\nu) = 0 \,, \tag{2.77}$$

$$v'_\alpha + \mathcal{H}v_\alpha + v_\nu\partial^\nu v_\alpha = -\partial_\alpha\varphi \,, \tag{2.78}$$

where φ is the gravitational potential associated with the density perturbation, $\rho = \bar{\rho} + \delta\rho$ is the total matter density composed by the background matter density, $\bar{\rho}$, and the matter density perturbation, $\delta\rho$, and, finally, $\mathbf{v}$ is the peculiar velocity field associated to the CDM haloes.

As the background cosmology, we have adopted a flat ΛCDM model with present baryon density given by $\Omega_{0\mathrm{b}} = 4.318 \times 10^{-2}$, dark and CDM energy density $\Omega_{0\Lambda} = 0.7434$, $\Omega_{0\mathrm{CDM}} = 0.2134$, Hubble constant $H_0 = 100h$ km/sec/Mpc where $h = 0.7199$

and three massless neutrino species; the primordial perturbation spectrum is made by scalars only, normalized by $\sigma_8 = \sigma(R = 8\,h^{-1}\,\mathrm{Mpc}) = 0.9$, with spectral index $n_s = 0.96$ [91, 92].

In order to evaluate the stochastic background of gravitational radiation generated by CDM haloes, we will exploit the Eq. (2.71) expressing the solution of the inhomogeneous GW equation on scales well inside the Hubble horizon and in the so-called wave zone, which is

$$h^{\alpha}{}_{\beta}(\eta, \mathbf{x}) = \frac{4G}{c^4}\frac{1}{ar}\mathcal{P}^{\alpha}{}_{\nu}{}^{\mu}{}_{\beta}\left[a^3 \int d^3\tilde{x}\, \mathcal{R}^{\nu}_{\mathrm{eff}\,\mu}\right]_{ret} , \tag{2.79}$$

where r is the comoving distance between source and observer while the projection operator is given by $\mathcal{P}^{\alpha}{}_{\beta} \equiv \delta^{\alpha}{}_{\beta} - x^{\alpha}x_{\beta}/r^2$. Eq. (2.79) expresses the GW output $h^{\alpha}{}_{\beta}$ in terms of integrals over the source "stress distribution" $\mathcal{R}^{\alpha}_{\mathrm{eff}\,\beta}$, given by

$$\begin{aligned}\mathcal{R}^{\alpha}_{\mathrm{eff}\,\beta} = \rho\left(v^{\alpha}v_{\beta} - \frac{1}{3}v^2\,\delta^{\alpha}{}_{\beta}\right) + \\ + \frac{1}{4\pi G a^2}\left(\partial^{\alpha}\varphi\,\partial_{\beta}\varphi - \frac{1}{3}\partial^{\nu}\varphi\,\partial_{\nu}\varphi\,\delta^{\alpha}{}_{\beta}\right) .\end{aligned} \tag{2.80}$$

The subscript "*ret*" in Eq. (2.79) means that the quantity has to be evaluated at the retarded space-time point $(\eta - r/c, \tilde{\mathbf{x}})$, *i.e.* at the source and at the emission time.

2.7 The ellipsoidal collapse model

Recently, N-body simulations in CDM models have shown departure of the halo density profile from the spherical symmetry (*e.g.* [93]) and suggest a triaxial shape which seems to be confirmed by optical, X-ray and lensing observations of galaxy clusters (*e.g.* [94, 95]).

Consequently, according to the arguments in the previous Section, CDM haloes are potential sources of gravitational radiation through power injection from the gravitational potential and peculiar velocity, especially during the highly non-linear stage of their evolution, when density contrasts and velocity fields can be strongly non-linear. Since the aim of this Section is to evaluate the stochastic GW background generated by a distribution of cosmic structures, we will hereafter describe the model adopted to approximate their dynamics and virialization.

2.7.1 The homogeneous ellipsoid dynamics

We will use the gravitational collapse of homogeneous ellipsoids as described in Ref. [96], which developed a picture of cosmic structure formation that identifies virialized cosmological objects with peak patches in the initial Lagrangian space. These peaks represent overdensities in the initial Gaussian density field whose evolution is approximated by a homogeneous ellipsoid dynamics. Each perturbation evolves under the influence of its own gravity and under the external tidal field (generated by the surrounding matter) which, together with initial conditions, is chosen to reproduce the Zel'dovich approximation in the linear regime. Virialization is defined as the time when the third axis collapses and, following Ref. [96], each axis is frozen once it has reached a freeze-out radius, chosen so that the density contrast at virialization, in the limit of spherical collapse, is the same as prescribed by the top-hat model.

The peculiar velocity field is conveniently described in the system identified by the three principal axes, characterized by three different scale factors R_α ($\alpha = 1, 2, 3$); thus, inside the homogeneous ellipsoid, peculiar velocities may be written as

$$v_\alpha = \left(a\frac{\dot{R}_\alpha}{R_\alpha} - \dot{a} \right) x_\alpha \,, \tag{2.81}$$

where we are still adopting comoving coordinates but now time derivatives are with respect to the proper time $dt = a\, d\eta$.

The internal peculiar gravitational potential, still with respect to the principal-axis system, is given by (see Ref. [96] for details)

$$\varphi = \pi G a^2 \bar{\rho} \left[\sum_{\alpha=1}^{3} (\delta b_\alpha + 2\lambda'_\alpha) x_\alpha^2 \right] \,, \tag{2.82}$$

where $\delta \equiv \delta\rho/\bar{\rho}$ is the matter density contrast while the factors b_α are given by (see *e.g.* Refs. [97, 98])

$$b_\alpha = R_1 R_2 R_3 \int_0^\infty \frac{ds}{(R_\alpha^2 + s)\sqrt{(R_1^2 + s)\,(R_2^2 + s)\,(R_3^2 + s)}} \,, \tag{2.83}$$

and the coefficients $4\pi G a^2 \bar{\rho} \lambda'_\alpha$ are the eigenvalues of the traceless external tidal tensor (proportional to the traceless part of the peak strain) for which a linear approximation is assumed [96], imposing that it evolves through the same equations satisfied by the linear growth-factor of density fluctuations in the considered cosmological background.

After imposing the Zel'dovich approximation to fix the initial conditions on the proper ellipsoid axis lengths and their time derivatives, the evolution of an ellipsoidal

perturbation is specified through the equations [96]

$$\frac{d^2R_\alpha}{dt^2} = \frac{\Lambda c^2}{3}R_\alpha - 4\pi G\bar{\rho}R_\alpha\left(\frac{1}{3}+\frac{\delta}{3}+\frac{b'_\alpha}{2}\delta+\lambda'_\alpha\right) , \tag{2.84}$$

$$\frac{d^2a}{dt^2} = \left(-\frac{4\pi G}{3}\bar{\rho}+\frac{\Lambda c^2}{3}\right)a , \tag{2.85}$$

$$\rho R_1 R_2 R_3 = \text{const} , \tag{2.86}$$

$$\bar{\rho}a^3 = \text{const} , \tag{2.87}$$

where, in Eq. (2.84), $b'_\alpha = b_\alpha - 2/3$.

Eqs. (2.84)-(2.87) have been numerically integrated using a fourth-order Runge-Kutta scheme and the integrals (2.83) have been evaluated by means of the so-called Carlson's elliptic function of the third kind.

Fig. 2.2 shows the axis evolution versus time of a homogeneous ellipsoid of mass $M = 5\times10^{15}M_\odot$ and initial overdensity $\delta(z_i = 40) = 6.4\times10^{-2}$ at comoving distance $D = 100$ Mpc from the observer. The shape of the ellipsoid is the most probable in terms of the distribution of ellipticity and prolateness, to be defined in the next sub-Section. The evolution follows Eqs. (2.84-2.87) and the axis freezing out method suggested in Ref. [96]. Let us stress that, contrary to other ellipsoidal collapse schemes (*e.g.* [99]), this model implies that virialization is reached when the third and not the first axis collapses, while the freezing out method avoids $\delta \longrightarrow \infty$.

In order to estimate the GW output by CDM cosmic structures, we insert Eqs. (2.81)-(2.82) in Eqs. (2.79)-(2.80) during the collapse of each homogeneous ellipsoid which represents, in our simulation, a CDM halo evolving towards virialization.

In Fig. 2.3 we show two of the three non-vanishing traceless source components generated by the halo collapse of Fig. 2.2. These components are evaluated with respect to the eigenframe of the ellipsoid principal axes at rest with respect to the expanding cosmological background; by performing a transverse projection, the gravitational waves in the observer frame are obtained. Actually, Fig. 2.3 represents these two components divided by $1+z = 1/a(t)$, in order to separate the effects of the background expansion, included in Eq. (2.79), from the halo evolution itself.

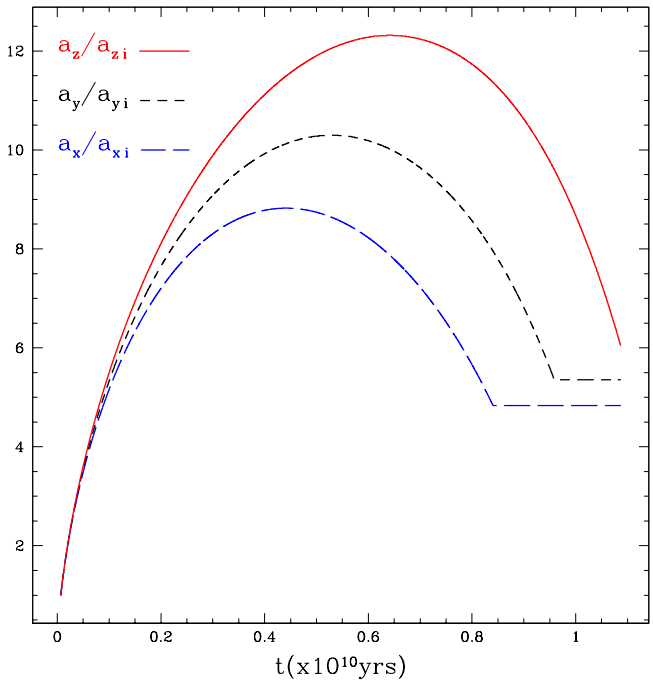

Figure 2.2: *Evolution of the principal axis scale factors for the most probable ellipsoid of mass* $M = 5 \times 10^{15} M_\odot$ *and initial overdensity* $\delta(z_i = 40) = 6.4 \times 10^{-2}$*, embedded in a flat* Λ*CDM universe, at distance* $D = 100$ Mpc *from the observer.*

2.7.2 The most probable ellipsoid and the halo mass function

Once the cosmological background model is fixed, the evolution of an ellipsoidal perturbation is determined by three parameters given by the three initial eigenvalues of what, in the Zel'dovich approximation, is called the deformation tensor, $d_{\alpha\beta} = (1/a^2)\nabla^2_\alpha \nabla^2_\beta \varphi$; the latter are related to the initial ellipticity e, prolateness p and linear density contrast δ of the perturbation; those relations read [100]

$$e = \frac{\lambda_1 - \lambda_3}{2\delta} \,, \tag{2.88}$$

$$p = \frac{\lambda_1 + \lambda_3 - 2\lambda_2}{2\delta} \,, \tag{2.89}$$

$$\delta = \lambda_1 + \lambda_2 + \lambda_3 \,, \tag{2.90}$$

where the λ_α are the eigenvalues of $d_{\alpha\beta}$ with $\lambda_1 \geq \lambda_2 \geq \lambda_3$, which, if $\delta \geq 0$, implies $e \geq 0$ and $-e \leq p \leq e$.

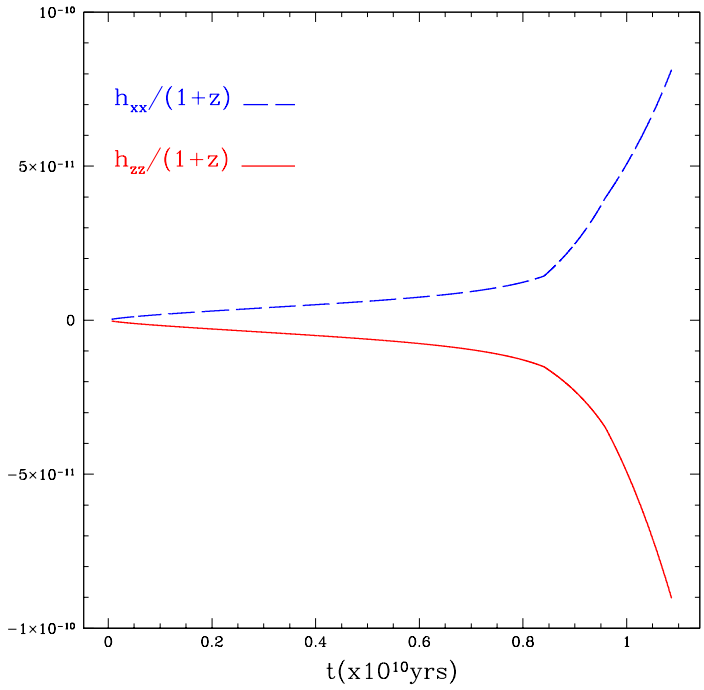

Figure 2.3: *Two of the three non-vanishing traceless source components generated by the halo collapse of Fig. 2.2*

For a Gaussian random density field, smoothed in real space with a top-hat filter of size $V = 4\pi R^3/3$ and mass $M = 4\pi\bar{\rho}R^3/3$, on average and for a given δ the prolateness is $p = 0$; consequently, the most probable ellipticity is $e_{mp} = (\sigma/\delta)/\sqrt{5}$. Here $\sigma = \sigma(R)$ represents the linear rms value of the δ distribution [100].

From these considerations and from the homogeneous ellipsoid collapse model as described in Ref. [96], the authors of Ref. [100] have determined the shape of the moving barrier, *i.e.* the critical overdensity required for CDM structure virialization at redshift z; that is

$$B(\sigma^2, z) = \sqrt{q}\delta_{sc}(z)\left[1 + \beta(\alpha\nu)^{-\alpha}\right] , \tag{2.91}$$

where $\nu \equiv [\delta_{sc}(z)/\sigma(M)]^2$, $\delta_{sc}(z)$ is the critical overdensity required for spherical collapse at z extrapolated using linear theory to the present time, and σ is the linear rms value of the initial density fluctuation field also extrapolated to the present time. The parameters $\beta \approx 0.485$ and $\alpha \approx 0.615$ come from ellipsoidal dynamics and the value $q \approx 0.75$ comes from normalizing the model to simulations [101].

Using Eq. (2.91) in the excursion set approach in order to obtain the distribution of the first crossings of the barrier by independent random walks, the authors of Refs. [100,

102] have derived the average comoving number density of haloes of mass M, *i.e.* the so-called unconditional halo mass function

$$n(M,z)dM = \sqrt{\frac{2qA^2}{\pi}}\,\frac{\rho_0}{M^2}\,\frac{\delta_{sc}(z)}{\sigma(M)}\,\left[1+\left(\frac{\sigma(M)}{\sqrt{q}\delta_{sc}(z)}\right)^{2p}\right] \times \left|\frac{d\ln\sigma}{d\ln M}\right|\,\exp\left(-\frac{q\delta_{sc}^2(z)}{2\sigma(M)^2}\right)dM\,, \tag{2.92}$$

where ρ_0 is the mean comoving cosmological mass density, while $p = 0.3$ and $A = 0.32218$. The Press-Schechter mass function is recovered for $q = 1$, $p = 0$ and $A = 0.5$ [103].

In what follows, $\sigma(M)$ and $\delta_{sc}(z)$ are computed according to the formulas [104, 105, 106]

$$\sigma \propto (1 + 2.208m^d - 0.7668m^{2d} + 0.7949m^{3d})^{-2/(9d)}\,, \tag{2.93}$$

where $d = 0.0873$, $m \equiv M(\Gamma h)^2/(10^{12}M_\odot)$ and

$$\Gamma = \Omega_{0\mathrm{m}}h\exp\left[-\Omega_{0\mathrm{b}}\left(1+\sqrt{2h}/\Omega_{0\mathrm{m}}\right)\right]\,. \tag{2.94}$$

The quantities related to the density contrast are

$$\delta_{sc}(z) = \frac{\delta_c\,D_+(z=0)}{D_+(z)}\,, \tag{2.95}$$

$$\delta_c \approx \frac{3\,(12\pi)^{2/3}}{20}(1 + 0.0123\log_{10}\Omega_{\mathrm{m}})\,. \tag{2.96}$$

The linear growth factor of density fluctuations, normalized to unity at present, may be approximated as [107]

$$D_+(z) = \frac{5\Omega_{\mathrm{m}}}{2(1+z)}\left[\Omega_{\mathrm{m}}^{4/7} - \Omega_\Lambda + \left(1+\frac{\Omega_{\mathrm{m}}}{2}\right)\left(1+\frac{\Omega_\Lambda}{70}\right)\right]^{-1}\,, \tag{2.97}$$

where $\Omega_{\mathrm{m}} = \Omega_{0\mathrm{m}}(1+z)^3/E^2(z)$, $\Omega_\Lambda = \Omega_{0\Lambda}/E^2(z)$, and

$$E(z) = H(z)/H_0 = \left[\Omega_{0\mathrm{m}}(1+z)^3 + \Omega_{0\Lambda}\right]^{1/2}\,. \tag{2.98}$$

2.8 The stochastic GW background from collapsing dark matter haloes

In order to evaluate the GW output generated by a spatial distribution of CDM haloes we will exploit Eq. (2.92) which provides a good fit to the N-body simulations of struc-

ture clustering in a variety of cosmological models, at least over the redshift range $z = 0 - 4$ [100, 101, 102, 108, 109].

For theoretical consistency, we have chosen to follow the same strategy adopted by Ref. [100] as described in the previous section. Therefore, in our numerical computation, we consider CDM structures over a mass range $M = 5 \times 10^9 M_\odot - 5 \times 10^{15} M_\odot$, which virialize at redshifts from $z = 0$ to 4. Each of these structures is approximated by a homogeneous ellipsoidal perturbation with mass M, linear mass variance $\sigma^2(M)$ and critical linear density contrast $\delta(M, z) = B(\sigma^2, z)$; in other words, every perturbation represents the most probable ellipsoid ($p = 0$ and $e = e_{mp}$) of mass M which collapses at redshift z.

Given the density contrast, the ellipticity and the prolateness, we then calculate the eigenvalues of the external tidal tensor, using Eqs.(2.88)-(2.90) and the relation $\lambda'_\alpha = \lambda_\alpha - \delta/3$. Next, we linearly rescale all quantities to the initial redshift $z_i = 40$, at which the ellipsoidal evolution of the density perturbation starts, following Eqs. (2.84)-(2.87). In fact, while the mass function provides the number of haloes virializing at a given redshift (in our case $z = 0 - 4$), the evolution of matter density perturbations, giving rise to these virialized objects, begins much before, *i.e.* at very high redshifts (in our case $z_i = 40$). The initial conditions on the scale factor are given by the relation $a(z_i) = 1/(1 + z_i)$ and by the well-known Friedmann equations, while, as we have already anticipated, the initial conditions on the axis lengths and their time derivatives are specified by the Zel'dovich approximation setup

$$R_\alpha(z_i) = a(z_i)(1 - \lambda_\alpha) \tag{2.99}$$

and

$$\dot{R}_\alpha(z_i) = H(z_i) \left[R_\alpha(z_i) - a(z_i) f(z_i) \lambda_\alpha \right] , \tag{2.100}$$

where $f(z) \approx \Omega_{\rm m}^{0.6} + (1/70) \left[1 - 1/2\Omega_{\rm m} \left(1 + \Omega_{\rm m} \right) \right]$ is the growth rate of density fluctuations (*e.g.* Ref. [110]).

For each M and z, using Eq. (2.79) and switching to the proper time t, we evaluate the two independent components of the gravitational radiation produced by a CDM halo, assuming that it is casually oriented and placed at a comoving distance $r(z)$ from the observer, where z is the collapse redshift. In this way, we observe today the radiation emitted at the virialization time when, according to our ellipsoidal model, the GW output has the maximum value. Actually, adopting this strategy, we slightly underestimate the total GW background, since we do not take into account those CDM haloes which

are still away from virialization. Moreover it is noteworthy here that, in our approach, we have extrapolated Eq. (2.79) outside its range of validity. In fact, this formula holds on scales well inside the Hubble horizon and in the wave zone (*i.e.* at distances larger than both the characteristic wavelengths and the characteristic size of the source), while, as we previously noticed, CDM haloes generate gravitational waves whose frequency is comparable with the inverse of the Hubble time. Nonetheless, as shown in the next Section, our results agree with several analytic approximations and previous works.

To account for all the directions of observation, we convert the two independent states $h^{\alpha}_{e\,\beta}(t)$ of tensor polarization from the frame associated with the ellipsoid principal axes to the observer frame, assuming that CDM structures emit in all directions and are uniformly distributed all around the observer. For this purpose, we use the relation $h^{\alpha}{}_{\beta}(t,\Omega) = R^{T\,\alpha}{}_{\nu}(\Omega)\, h^{\nu}_{e\,\mu}(t)\, R^{\mu}{}_{\beta}(\Omega)$ where $R^{\alpha}{}_{\beta}(\Omega)$ is the general form of the rotation matrix with $\psi = 0$ [111]

$$R^{\alpha}{}_{\beta}(\Omega) \equiv \begin{pmatrix} \cos\phi & \sin\phi & 0 \\ -\cos\theta\sin\phi & \cos\theta\cos\phi & \sin\theta \\ \sin\theta\sin\phi & -\sin\theta\cos\phi & \cos\theta \end{pmatrix} ,$$

and the solid angle $\Omega \equiv (\theta, \phi)$ is defined following the conventions of Ref. [112].

Since our aim is to estimate the energy density

$$\Omega_{\rm GW}(\nu) \approx \frac{2\pi^2}{3H_0^2}\nu^3 {\rm PSD}(\nu) , \tag{2.101}$$

associated with the stochastic GW background at the observer (*e.g.* Ref. [69]), we need to know the power spectral density ${\rm PSD}(\nu)$, which one can obtain from the Parseval's theorem as

$$\langle h^{\alpha}{}_{\nu}(t) h^{\nu}{}_{\beta}(t)\rangle = \int_{-\infty}^{\infty} d\nu {\rm PSD}(\nu) . \tag{2.102}$$

That depends on the redshifted proper frequency $\nu = \nu_e/(1+z)$, where ν_e is the proper frequency at the emission time. In Eq. (2.102) angle brackets denote time averaging at a given spatial point.

Thus, we first numerically evaluate the ${\rm PSD}(\nu, z, M, \Omega)$ of each individual component of $h^{\alpha}{}_{\beta}(t,\Omega)$ at each fixed value of M, z and Ω, then we average the calculated PSDs over all directions by integrating over the solid angle and dividing by 4π and, finally, we sum over the components in order to get a mean power spectral density ${\rm PSD}(\nu, z, M)$ for every z and M.

Since in our model each CDM halo is approximated by a most probable ellipsoid of mass M which collapses at redshift z, we multiply each ${\rm PSD}(\nu, z, M)$ by

the number $dN(z,M) = n(z,M)dMdV$ of haloes in the comoving volume $dV(z) = 4c\,\pi r^2(z)dz/\left(a_0 H(z)\right)$ where c is the speed of light and $a_0 \equiv 1$ is the present value of the scale factor. Finally, we insert the resulting quantity in the definition of the GW energy density Eq. (2.101) and integrate over all redshifts and masses to obtain the total $\Omega_{\rm GW}(\nu)$.

All the results are presented in the next section.

2.9 Results

Our result concerning the GW output of each CDM halo, an example of which is given in Fig. 2.3, is consistent with previous works in this field [113, 114]. Moreover it is comparable to analytic approximations (*e.g.* [60, 115]) as

$$h \approx \frac{3\times 10^{-11}}{D/100{\rm Mpc}} \times \frac{GM\left(10^{15}\right)^{2/7}}{c^2 L} \times \frac{M}{10^{15}M_\odot}, \tag{2.103}$$

where h represents the amplitude of a GW signal coming from a non-spherically symmetric collapsing object with characteristic size L at distance D from the observer.

It is worth noting that the produced gravitational radiation has a very long characteristic period, approximately given by the inverse of the halo evolution time, which, according to the ellipsoidal model, corresponds to frequencies of the order of $\nu \approx 10^{-18}$Hz. This excludes, therefore, any direct detection of a complete pulse, but still allows for the possibility of GW detection via secondary CMB anisotropy and polarization and via the "secular effect" discussed in Refs. [113, 114]. The latter takes place when a gravitational-wave crosses two testing particles; this induces a variation in their relative distance which increases in time, since this effect lasts for many years.

Actually, besides what stressed in the previous Section, there are other reasons for which the ellipsoidal collapse approximation to CDM halo virialization underestimates amplitude and frequency characterizing the GW background. In fact, using this approach, the evolution of cosmic structures is regarded as a continuous phenomenon which neglects merging effects and any possible features of variability that, according to Ref. [113], should be characterized by a dynamical frequency of the order of $\nu \approx 10^{-17}$Hz.

In Fig. 2.4 the main result of this work is shown, *i.e.* the total energy density $\Omega_{\rm GW}(\nu) \approx 10^{-20}$, associated with the stochastic halo-induced GW background, as a function of the proper frequency ν at the observation. The total spectrum of the sig-

nal is composed by many single peaks which represent the contribution to the total background from each most probable halo weighted via the mass function at different redshifts. On the other hand, as the following discussion shows, these peaks are caused by the subset of structures leading to a non-negligible GW signal. In fact Eq. (2.79) shows that the GW amplitude is proportional to the inverse of the comoving distance, while, from the expression of the efficiency $\epsilon = GM/(c^2 L)$ and the total radiated energy $E_{GW} = \epsilon M c^2$, where L represents the characteristic halo size at virialization, it follows that more massive objects give rise to higher values of the GW strain. This effect is also confirmed by numerical estimates of the power spectral density for different objects in the redshift range $0 \leq z \leq 4$. In fact, masses of the order of $10^8 - 10^9 M_\odot$, although weighted via the mass function in Eq. (2.92), contribute to $\Omega_{\rm GW}(\nu)$ by only a factor of orders of $10^{-30} - 10^{-28}$; since the amplitude of the gravitational waves decreases with distance, the greater is the redshift z, the lower is their contribution. Thus only a few peaks are visible in Fig. 2.4 since the energy density produced by less massive structures is completely negligible with respect to the effect (of orders of $10^{-21} - 10^{-20}$) of far more massive objects ($10^{14} - 10^{15} M_\odot$) at low redshifts, $z \leq 1$.

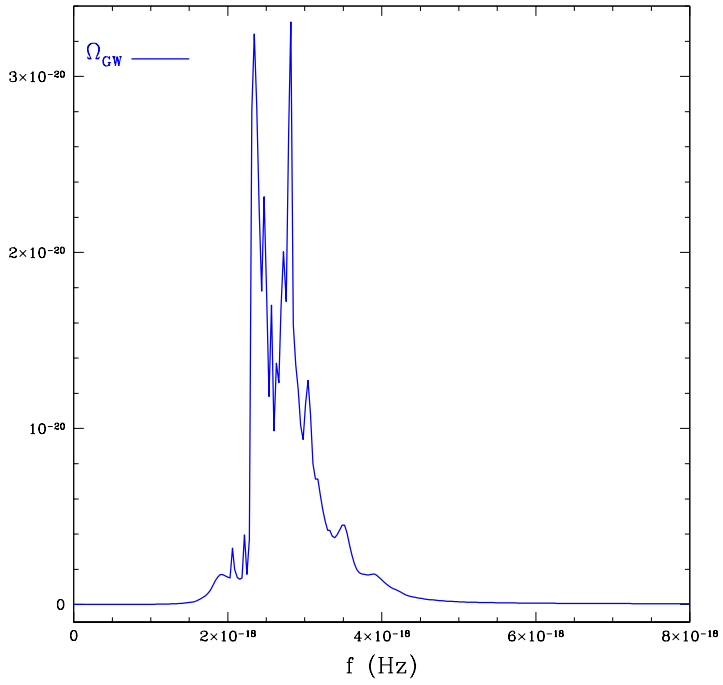

Figure 2.4: *The total energy density $\Omega_{\rm GW}(\nu)$ associated with the stochastic GW background induced by CDM haloes as a function of the proper frequency ν at observation.*

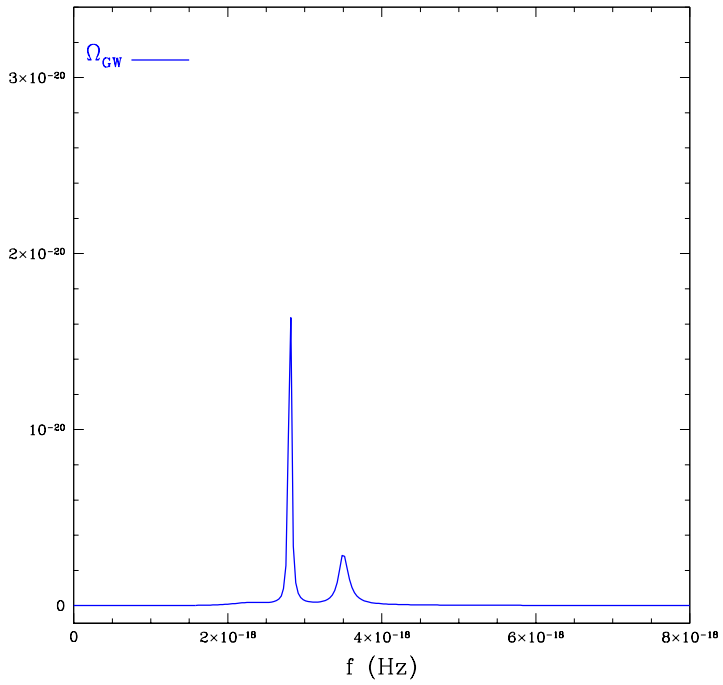

Figure 2.5: *Contribution to the total energy density* $\Omega_{\rm GW}(\nu)$ *by two most probable CDM haloes of mass* $5 \times 10^{15} M_\odot$ *placed at redshifts* $z = 0.025$ *and* 0.075.

Consequently, the dominant contribution to the stochastic GW background is likely to be produced by CDM haloes corresponding to nearby galaxies and galaxy clusters which contribute by several orders of magnitudes more than their substructures, although the latter are far more numerous. Indeed, in Fig. 2.5 we may look at the contribution to the total $\Omega_{\rm GW}(\nu)$ (see Fig. 2.4) by two most probable haloes of mass $5 \times 10^{15} M_\odot$, placed at redshifts $z = 0.025$ and 0.075. In its maximum height, the signal reaches about half of the corresponding value in Fig. 2.4. The remaining part of the signal is caused by many haloes of comparable mass, as well as by those about one order of magnitude lighter, for which the mass decrease is compensated by the increase in the number. It is worth noting that the ellipsoidal collapse model introduces a three-peak pattern due to the freezing out method used to stop the axis collapse, which as a zero-th order approximation imposes stability at virialization, ignoring any residual dynamics. In the case of the specific geometrical configuration of the most probable ellipsoid considered in Fig. 2.5, this translates in two prominent peaks and a third negligible one. Actually, the residual dynamics at virialization would most probably imply a broadening of the spikes, decreasing the frequency splitting, possibly converging to a single peak for

configurations close to sphericity.

Finally and most importantly, the quantity $h^2\Omega_{\rm GW}(\nu) \approx 10^{-20}$ is comparable to the energy density associated with the stochastic background induced by primordial GWs. In fact, if the energy scale of inflation is $V^{1/4} \approx 1 - 2 \times 10^{15}$GeV, the energy density associated with the primordial stochastic GW background, with a tensor spectral index $n_T \approx 0$, is $\approx 10^{-21} - 10^{-17}$ for frequencies of the order of $10^{-18} - 10^{-17}$ Hz (*e.g* Ref. [69]).

Summarizing, we have estimated the GW background from cosmological tensor modes produced by the highly non-linear collapse of CDM density perturbations, *i.e.* generated during the strongly non-linear stage of CDM halo evolution.

We found that the signal is significant at very low frequencies, $\nu \approx 10^{-18}$ Hz, as a consequence of the cosmological time scales involved in the collapse of CDM haloes. This signal appears as a broad peak made by the superposition of many impulses, all centered around frequencies of the order of 10^{-18} Hz. Most importantly, our results suggest that the signal is likely to be comparable to the primordial tensor power if inflation occurred at the GUT scale.

We want to stress that the homogeneous ellipsoidal collapse model, adopted to simulate CDM halo evolution and virialization, underestimates the frequency and amplitude of the emitted gravitational waves, since, at each redshift z, it does not take into account non-virialized objects and neglects variability features and merging effects that could enhance the anisotropic stress sourcing tensor modes, which are more sensible to the velocity field rather than to the peculiar gravitational potential. Consequently, the total energy density $\Omega_{\rm GW}(\nu)$ generated by cosmic structures could even be of one or two order of magnitudes greater and overcome the stochastic background associated with primordial gravitational waves at the same frequencies (see also results in Ref. [114]).

The CDM halo GW background could also produce a non-negligible contribution when considering the cosmological tensor-to-scalar ratio.

Due to the cosmological scales involved, and to the amplitude of the signal, it is reasonable to expect that these gravitational waves could affect the primary CMB anisotropies, contributing to the Integrated Sachs Wolfe (ISW) effect caused by the time evolution of cosmological perturbations between us and the last scattering surface. The stochastic GW background from CDM haloes might boost the temperature anisotropies

on large angular scales, where however the contribution from density fluctuations dominates. On the other hand, the produced temperature quadrupole can be scattered off by the free electrons of the intra-cluster and intra-galactic media, giving rise to secondary anisotropies similarly to what happens for the primordial temperature quadrupole as described in Ref. [116]. These contributions have to be taken into account when performing a precise evaluation of the level of CMB polarization anisotropy expected for the forthcoming polarization oriented CMB probes.

Most of these issues deserve a careful investigation in future works. Here we conclude stressing again our main results, suggesting that the amplitude of the stochastic GW background generated by CDM haloes in their non-linear evolutionary phase is comparable or larger than the signal expected from the early universe in the inflationary scenario. We also remark that our findings are consistent with existing analytical approximations. The forthcoming steps are the improvement of the calculation of the source of the signal, making use of cosmological N-body simulations, as well as the computation of the induced CMB anisotropy in total intensity and polarization.

In Chapter 2.6 we will consider another major contribution to CMB anisotropies from structure formation, represented by gravitational lensing.

Chapter 3

The Cosmic Microwave Background

The CMB radiation contributes of order a percent to the static "snow" seen when switching between channels on a television with a conventional VHF antenna; it has therefore been detected a number of times before its discovery/identification by Penzias and Wilson in 1965 [117]. For instance, in 1941 McKellar [118] deduced a CMB temperature of 2.3 K at a wavelength of 2.6 mm by estimating the ratio of populations in the first excited rotational and ground states of the interstellar cyanogen (CN) molecule. In addition, it is now known that the discrepancy of 3.3 K found in 1961 by Ohm [119], between the measured and expected temperature of the Bell Labs horn antenna at a wavelength of 12.5 cm, is due to the CMB. Unfortunately, McKellar had the misfortune of performing his analyses well before that in 1948 Gamow and his collaborators [120, 121] laid the nucleosynthesis foundations that would have eventually explained the CN measurements and allowed the CMB interpretation.

Even Ohm himself properly did not overly stress the 3.3 K discrepancy beyond its weak statistical significance, and also Doroshkevich and Novikov in 1964, and Zel'dovich in 1965, referred to Ohm measurement but did not notice the 3.3 K discrepancy. On the contrary Zel'dovich even incorrectly argued that Ohm constrained the temperature to be less than 1 K (and not 3.3 K) and that, given the observed helium abundance, such fact should rule out the hot Big Bang Model!

Three years later, working with the same antenna as Ohm, and paying very careful attention to possible systematic effects, Penzias and Wilson [117] measured the excess temperature to be 3.5 ± 1 K at 7.35 cm wavelength; Dicke et al. [122] then identified that as the CMB radiation left over from the hot Big Bang.

To date there is no observational indication of any deviation of the CMB spectrum from

a Planckian blackbody of primordial origin. A definitive observation of the CMB spectrum was made by COBE in 1992 [123] which measured a temperature of 2.725 ± 0.002 K (95 % confidence), and first detected the CMB anisotropies which reveals important features of the formation and evolution of structures in the Universe Fig. (3.1).

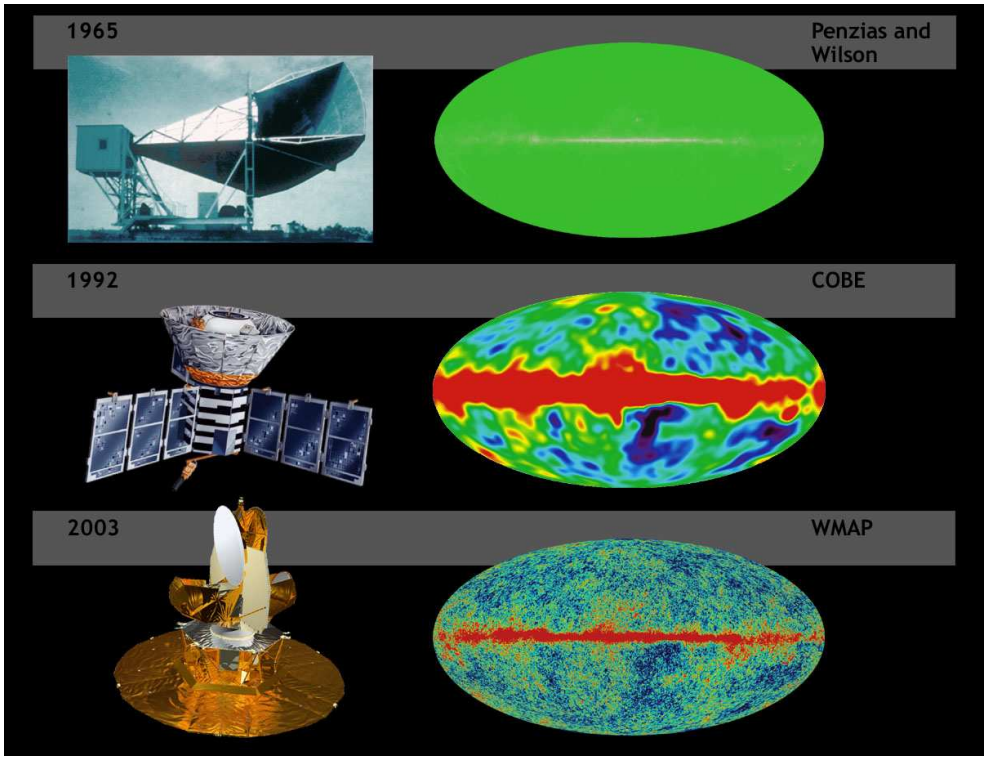

Figure 3.1: *Top-left: Penzias&Wilson microwave receiver. Top-right: A view of the sky as would have been seen by the Penzias&Wilson receiver if it could have surveyed the whole sky. Middle-left: COBE Spacecraft 1992. Middle-right: COBE's 4-year sky map. It is a low resolution image, but CMB temperature anisotropies are apparent as cold and hot spots in the image. The large red band is the microwave emission from our galaxy. Bottom-left: WMAP spacecraft. Bottom-right: Simulated WMAP all-sky map of the CMB temperature. From http://map.gsfc.nasa.gov/.*

3.1 CMB anisotropies

CMB anisotropies have their origin very back in time, beyond a point when distances in the universe were only 0.1% of their current size. At that time, the temperature was high enough to ionize the universe, which was filled with a plasma of protons, electrons, and photons plus a few He nuclei and traces of other species.

Before the transition from an ionized to a neutral medium the universe could be modeled as a smooth gas of photons, baryons (protons and electrons) and dark matter. Since the number density of free electrons was very high, the universe was opaque to the microwave background photons: the mean free path for photons to Thomson scatter off electrons was extremely short. Consequently, the photons and baryons could be considered as a single "tightly coupled" fluid in which the baryons provide the weight, while the photons provide the pressure.
As the universe expanded, the wavelengths of photons were stretched out, lowering their energy and eventually, when the universe had cooled to $T \sim 4,000$K, the photon energies became too small to ionize hydrogen. At this point the protons and electrons recombined to form neutral hydrogen and the photon mean free path increased to essentially the size of the observable universe.

These photons, which constitute the cosmic microwave background, continued to lose energy with the expansion of the universe, and now form a black body with a temperature of 2.73 K.

The CMB temperature is conventionally expressed as an expansion in spherical harmonic multipoles on the sky, and for a Gaussian random process the angular power spectrum completely characterizes the CMB temperature anisotropy.

As a result of the gravitational growth of inhomogeneities in the matter distribution, when the photons decouple from the baryons at LS at a redshift $z \sim 10^3$, the photon temperature distribution is spatially anisotropic. Moreover, in the presence of a CMB temperature quadrupole anisotropy, Thomson-Compton scattering of CMB photons off electrons prior to decoupling generates a linear polarization anisotropy of the CMB Fig. (3.2).

After decoupling the CMB photons propagate almost freely, influenced only by gravitational perturbations and late-time reionization.
The largest anisotropy is a fluctuation of about $1/1000$; it forms a dipole pattern across the sky. It is due to the fact that the earth is not at rest with respect to the CMB, and we see a Doppler shift in the CMB temperature owing to our relative motion. Since this changes as the earth orbits the sun, this dipole is modulated throughout the year.
If we take the mass distribution observed around us and compute from this a gravitational acceleration, then multiply this acceleration by the age of the universe, we obtain a good match to both the direction and the amplitude of our velocity vector in the CMB rest frame [124]. However this dipole is clearly of local rather than primordial origin,

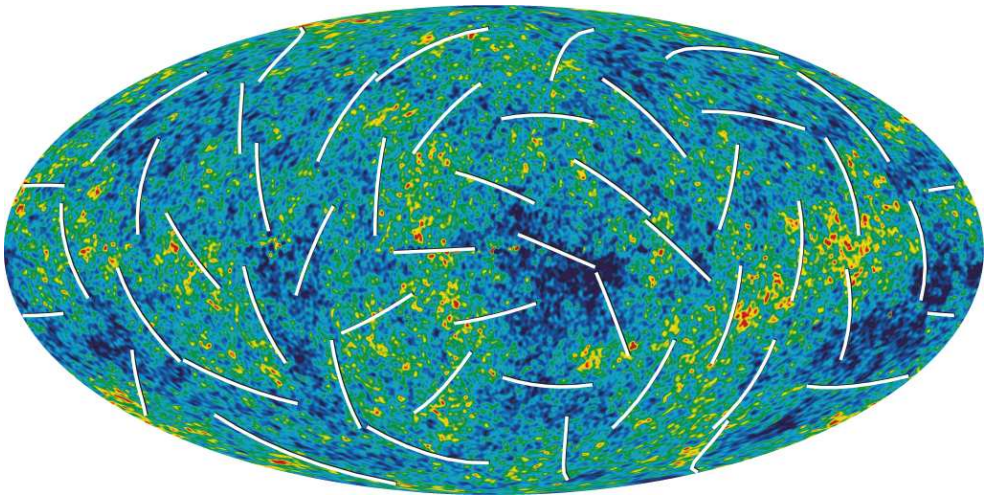

Figure 3.2: *WMAP–3 all-sky map of the CMB temperature and polarization. Blue and red spots represent colder and hotter temperatures with respect to the average. The lines represent the polarization direction on large scales. From http://map.gsfc.nasa.gov/.*

and so it is generally subtracted (plus the mean or "monopole") before dealing with the CMB anisotropies; doing that the size of the fluctuations decreases to $\sim 1/100.000$.

3.2 Mathematical description of CMB anisotropy and polarization

As the ordinary electromagnetic radiation, the CMB radiation field is characterized by a 2×2 intensity tensor I_{ij}. The Stokes parameters Q and U are defined as $Q = (I_{11} - I_{22})/2$ and $U = (I_{12} + I_{21})/2$, while the temperature anisotropy is given by $T = (I_{11} + I_{22})/2$. In principle the fourth Stokes parameter $V = (I_{21} + I_{12})/(2i)$ that describes circular polarization would also be needed, but in cosmology it can be ignored because it cannot be generated through Thomson scattering and consequently is vanishing in the damping of primordial vorticity already discussed. While the temperature is invariant under a right handed rotation in the plane perpendicular to direction $\hat{\boldsymbol{n}}$, Q and U transform under rotation by an angle ψ as (*e.g.* [125])

$$\begin{aligned} Q' &= Q\cos 2\psi + U \sin 2\psi \,, \\ U' &= -Q\sin 2\psi + U \cos 2\psi \,, \end{aligned} \tag{3.1}$$

where $\hat{\mathbf{e_1}}' = \cos\psi\hat{\mathbf{e_1}} + \sin\psi\hat{\mathbf{e_2}}$ and $\hat{\mathbf{e_2}}' = -\sin\psi\hat{\mathbf{e_1}} + \cos\psi\hat{\mathbf{e_2}}$. This means it is possible to construct two quantities from the Stokes Q and U parameters that have a definite value of spin

$$(Q \pm iU)'(\hat{\boldsymbol{n}}) = e^{\mp 2i\psi}(Q \pm iU)(\hat{\boldsymbol{n}}). \tag{3.2}$$

These quantities can be expanded in the appropriate spin-weighted basis

$$\begin{aligned} T(\hat{\boldsymbol{n}}) &= \sum_{lm} a_{T,lm} Y_{lm}(\hat{\boldsymbol{n}}) \\ (Q+iU)(\hat{\boldsymbol{n}}) &= \sum_{lm} a_{2,lm}\ {}_2Y_{lm}(\hat{\boldsymbol{n}}) \\ (Q-iU)(\hat{\boldsymbol{n}}) &= \sum_{lm} a_{-2,lm}\ {}_{-2}Y_{lm}(\hat{\boldsymbol{n}}). \end{aligned} \tag{3.3}$$

Q and U are defined at a given direction $\boldsymbol{n}$ with respect to the spherical coordinate system $(\hat{\mathbf{e}}_\theta, \hat{\mathbf{e}}_\phi)$. The expansion coefficients for the polarization variables satisfy $a^*_{-2,lm} = a_{2,l-m}$, and for temperature the relation is $a^*_{T,lm} = a_{T,l-m}$.

The Stokes parameters are not invariant under rotations in the plane perpendicular to $\hat{\boldsymbol{n}}$, but, by means of the so-called spin raising and lowering operators $\eth$ and $\bar{\eth}$ [126], it is possible to obtain spin zero quantities which have the advantage of being *rotationally invariant* like the temperature. Acting twice with $\eth$, $\bar{\eth}$ on $Q \pm iU$ in Eq. (3.3) leads to

$$\begin{aligned} \bar{\eth}^{\,2}(Q+iU)(\hat{\boldsymbol{n}}) &= \sum_{lm}\left[\frac{(l+2)!}{(l-2)!}\right]^{1/2} a_{2,lm} Y_{lm}(\hat{\boldsymbol{n}}) \\ \eth^{\,2}(Q-iU)(\hat{\boldsymbol{n}}) &= \sum_{lm}\left[\frac{(l+2)!}{(l-2)!}\right]^{1/2} a_{-2,lm} Y_{lm}(\hat{\boldsymbol{n}}). \end{aligned} \tag{3.4}$$

The expressions for the expansion coefficients are

$$\begin{aligned} a_{T,lm} &= \int d\Omega\ Y^*_{lm}(\hat{\boldsymbol{n}}) T(\hat{\boldsymbol{n}}) \\ a_{2,lm} &= \int d\Omega\ {}_2Y^*_{lm}(\hat{\boldsymbol{n}})(Q+iU)(\hat{\boldsymbol{n}}) \\ &= \left[\frac{(l+2)!}{(l-2)!}\right]^{-1/2} \int d\Omega\ Y^*_{lm}(\hat{\boldsymbol{n}})\bar{\eth}^{\,2}(Q+iU)(\hat{\boldsymbol{n}}) \\ a_{-2,lm} &= \int d\Omega\ {}_{-2}Y^*_{lm}(\hat{\boldsymbol{n}})(Q-iU)(\hat{\boldsymbol{n}}) \\ &= \left[\frac{(l+2)!}{(l-2)!}\right]^{-1/2} \int d\Omega\ Y^*_{lm}(\hat{\boldsymbol{n}})\eth^{\,2}(Q-iU)(\hat{\boldsymbol{n}}). \end{aligned} \tag{3.5}$$

Instead of $a_{2,lm}$, $a_{-2,lm}$ it is convenient to introduce their linear combinations [127]

$$\begin{aligned} a_{E,lm} &= -(a_{2,lm} + a_{-2,lm})/2 \\ a_{B,lm} &= i(a_{2,lm} - a_{-2,lm})/2. \end{aligned} \tag{3.6}$$

These two combinations behave differently under parity transformation: while the E electric (or gradient) mode remains unchanged, the B magnetic (or curl) mode changes the sign, in analogy with electric and magnetic fields [87, 84].

To characterize the statistics of the CMB perturbations only four power spectra are needed, those for T, E, B and the cross correlation between T and E. The cross correlation between B and E or B and T vanishes because B has the opposite parity of T and E.

The power spectra are defined as the rotationally invariant quantities

$$\begin{aligned} C_{Tl} &= \frac{1}{2l+1}\sum_m \langle a^*_{T,lm} a_{T,lm}\rangle \\ C_{El} &= \frac{1}{2l+1}\sum_m \langle a^*_{E,lm} a_{E,lm}\rangle \\ C_{Bl} &= \frac{1}{2l+1}\sum_m \langle a^*_{B,lm} a_{B,lm}\rangle \\ C_{Cl} &= \frac{1}{2l+1}\sum_m \langle a^*_{T,lm} a_{E,lm}\rangle \end{aligned} \tag{3.7}$$

in terms of which, assuming Gaussianity, one has

$$\begin{aligned} \langle a^*_{T,l'm'} a_{T,lm}\rangle &= C_{Tl}\delta_{l'l}\delta_{m'm} \\ \langle a^*_{E,l'm'} a_{E,lm}\rangle &= C_{El}\delta_{l'l}\delta_{m'm} \\ \langle a^*_{B,l'm'} a_{B,lm}\rangle &= C_{Bl}\delta_{l'l}\delta_{m'm} \\ \langle a^*_{T,l'm'} a_{E,lm}\rangle &= C_{Cl}\delta_{l'l}\delta_{m'm} \\ \langle a^*_{B,l'm'} a_{E,lm}\rangle &= \langle a^*_{B,l'm'} a_{T,lm}\rangle = 0. \end{aligned} \tag{3.8}$$

Introducing the linear temperature perturbation $\Delta_T \equiv \Delta T/T$, and the photon density matrix $\vec{\mathcal{T}} \equiv (\Delta_T, Q+iU, Q-iU)$, the Stokes parameters satisfy the linearized Boltzmann equation

$$\frac{d}{d\eta}\vec{\mathcal{T}}(\eta,\vec{x},\hat{n}) = \vec{C}[\vec{\mathcal{T}}] + \vec{G}\left[h_{\mu\nu}\right] \ , \tag{3.9}$$

which describes the evolution of the vector $\vec{\mathcal{T}}$ under the Thomson collisional term $\vec{C}[\vec{\mathcal{T}}]$ and gravitational redshift in the perturbed metric $\vec{G}\left[h_{\mu\nu}\right]$ [129].

The temperature anisotropy at position $\vec{x}$ in the direction $\vec{n}$ is denoted with $\Delta_T(\vec{x},\vec{n})$. In principle it depends both on the direction and on the frequency, but, because spectral distortions are only introduced at the second order, the frequency dependence can in the lowest order be integrated out. Anisotropy $\Delta_T(\vec{x},\vec{n})$ can be expanded in terms of

Fourier modes $\Delta_T(\vec{k},\vec{n})$, which in linear perturbation theory evolve independently of one another. Assuming perturbations are axially-symmetric around $\vec{k}$, we may further Legendre expand the anisotropy in the angle $\mu = \vec{k}\cdot\vec{n}/k$,

$$\Delta_T(\vec{k},\vec{n}) = \sum_l (2l+1)(-i)^l \Delta_{Tl} P_l(\mu), \tag{3.10}$$

where $P_l(\mu)$ is the Legendre polynomial of order l and Δ_{Tl} is the associated multipole moment. A similar decomposition also applies to the amplitude of polarization anisotropy $\Delta_P(\vec{k},\vec{n})$ where $\Delta_P \equiv \sqrt{Q^2+U^2}$ [130].

In what follows the longitudinal gauge will be used, in which the first-order perturbations to the metric tensor g_{ij} are specified with two scalar potentials ϕ and ψ and a gauge-invariant tensor perturbation h (vector perturbations can be neglected at the linear level). The corresponding temperature and polarization anisotropies are denoted as $\Delta_T^{(S)}$, $\Delta_P^{(S)}$ for scalar and $\Delta_T^{(T)}$, $\Delta_P^{(T)}$ for tensor components. In linear perturbation theory the scalar and tensor perturbations evolve independently and the total power is given by the sum of the two contributions. After the Fourier expansion and making the Thomson and gravitational scattering terms explicit, the Boltzmann evolution Eq. (3.9) for scalar perturbations can be written as [131],

$$\begin{aligned}
\dot{\Delta}_T^{(S)} + ik\mu\Delta_T^{(S)} &= \dot{\phi} - ik\mu\psi + \dot{\kappa}\{-\Delta_T^{(S)} + \Delta_{T0}^{(S)} + i\mu v_b + \frac{1}{2}P_2(\mu)\Pi\} \\
\dot{\Delta}_P^{(S)} + ik\mu\Delta_P^{(S)} &= \dot{\kappa}\{-\Delta_P^{(S)} + \frac{1}{2}[1-P_2(\mu)]\Pi\} \\
\Pi &= \Delta_{T2}^{(S)} + \Delta_{P2}^{(S)} + \Delta_{P0}^{(S)}.
\end{aligned} \tag{3.11}$$

Here the derivatives are taken with respect to the conformal time η, and v_b is the linear velocity of baryons. Differential optical depth for Thomson scattering is denoted as $\dot{\kappa} = an_e x_e \sigma_T$, where $a(\eta)$ is the expansion factor normalized to unity today, n_e is the electron density, x_e is the ionization fraction and σ_T is the Thomson cross section. The total optical depth at time η is obtained by integrating $\dot{\kappa}$, $\kappa(\eta) = \int_\eta^{\eta_0} \dot{\kappa}(\eta)d\eta$. A useful variable is the visibility function $g(\eta) = \dot{\kappa}\exp(-\kappa)$. Its peak defines the epoch of recombination, when the dominant contribution to the CMB anisotropies arises.

Expanding the temperature anisotropy in multipole moments one finds the follow-

ing hierarchy of coupled differential equations [132, 133, 134]

$$\begin{aligned}
\dot{\Delta}^{(S)}_{T0} &= -k\Delta^{(S)}_{T1} + \dot{\phi}\,, \\
\dot{\Delta}^{(S)}_{T1} &= \frac{k}{3}\left[\Delta^{(S)}_{T0} - 2\Delta^{(S)}_{T2} + \psi\right] + \dot{\kappa}(\frac{v_b}{3} - \Delta^{(S)}_{T1})\,, \\
\dot{\Delta}^{(S)}_{T2} &= \frac{k}{5}\left[2\Delta^{(S)}_{T1} - 3\Delta^{(S)}_{T3}\right] + \dot{\kappa}\left[\frac{\Pi}{10} - \Delta^{(S)}_{T2}\right]\,, \\
\dot{\Delta}^{(S)}_{Tl} &= \frac{k}{2l+1}\left[l\Delta^{(S)}_{T(l-1)} - (l+1)\Delta^{(S)}_{T(l+1)}\right] - \dot{\kappa}\Delta^{(S)}_{Tl}\,, l > 2 \\
\dot{\Delta}^{(S)}_{Pl} &= \frac{k}{2l+1}\left[l\Delta^{(S)}_{P(l-1)} - (l+1)\Delta^{(S)}_{P(l+1)}\right] + \dot{\kappa}\left[-\Delta^{(S)}_{Pl} + \frac{1}{2}\Pi\left(\delta_{l0} + \frac{\delta_{l2}}{5}\right)\right]\,, \qquad (3.12)
\end{aligned}$$

where δ_{ij} is the Kronecker symbol.

For tensor perturbations the Boltzmann equation is given by [135],

$$\begin{aligned}
\dot{\Delta}^{(T)}_{T} + ik\mu\Delta^{(T)}_{T} &= -\dot{h} - \dot{\kappa}(\Delta^{(T)}_{T} - \Psi)\,, \\
\dot{\Delta}^{(T)}_{P} + ik\mu\Delta^{(T)}_{P} &= -\dot{\kappa}(\Delta^{(T)}_{P} + \Psi)\,, \\
\Psi \equiv \left[\frac{1}{10}\Delta^{(T)}_{T0}\right. &+ \left.\frac{1}{35}\Delta^{(T)}_{T2} + \frac{1}{210}\Delta^{(T)}_{T4} - \frac{3}{5}\Delta^{(T)}_{P0} + \frac{6}{35}\Delta^{(T)}_{P2} - \frac{1}{210}\Delta^{(T)}_{P4}\right]. \qquad (3.13)
\end{aligned}$$

Instead of solving the coupled system of differential Eqs. (3.12) one may formally integrate Eqs. (3.11) along the photon past light cone to obtain [136],

$$\begin{aligned}
\Delta^{(S)}_{T} &= \int_0^{\eta_0} d\eta e^{ik\mu(\eta-\eta_0)} e^{-\kappa}\{\dot{\kappa}e^{-\kappa}[\Delta_{T0} + i\mu v_b + \frac{1}{2}P_2(\mu)\Pi] + \dot{\phi} - ik\mu\psi\} \\
\Delta^{(S)}_{P} &= -\frac{1}{2}\int_0^{\eta_0} d\eta e^{ik\mu(\eta-\eta_0)} e^{-\kappa}\dot{\kappa}[1 - P_2(\mu)]\Pi. \qquad (3.14)
\end{aligned}$$

Expressions above can be manipulated leading to the following expression,

$$\begin{aligned}
\Delta^{(S)}_{T,P} &= \int_0^{\eta_0} d\eta e^{ik\mu(\eta-\eta_0)} S^{(S)}_{T,P}(k,\eta) \\
S^{(S)}_{T}(k,\eta) &= g\left(\Delta_{T0} + \psi - \frac{\dot{v}_b}{k} - \frac{\Pi}{4} - \frac{3\ddot{\Pi}}{4k^2}\right) \\
&+ e^{-\kappa}(\dot{\phi} + \dot{\psi}) - \dot{g}\left(\frac{v_b}{k} + \frac{3\dot{\Pi}}{4k^2}\right) - \frac{3\ddot{g}\Pi}{4k^2} \\
S^{(S)}_{P}(k,\eta) &= -\frac{3}{4k^2}\left(g\{k^2\Pi + \ddot{\Pi}\} + 2\dot{g}\dot{\Pi} + \ddot{g}\Pi\right). \qquad (3.15)
\end{aligned}$$

As will be explained in more detail in Sec. (3.3), some of the terms in the source function $S^{(S)}_T(\eta)$ are manifest evidence of the physics behind the CMB anisotropy and polarization. The first two contributions in the first term are the intrinsic anisotropy and gravitational potential contributions from the LS surface, while the third contribution

is part of the velocity term, the other part being the $k^{-1}\dot{g}v_b$ term in the second row. These terms make a dominant contribution to the anisotropy in the standard recombination models. The first term in the second row, $e^{-\kappa}(\dot{\phi}+\dot{\psi})$, is the so-called integrated Sachs-Wolfe (ISW) term and is important after recombination. It is especially important if matter-radiation equality occurs close to the recombination and in ΛCDM models. In both cases gravitational potential decays with time, which leads to an enhancement of anisotropies on large angular scales. Finally we have the terms caused by photon polarization and anisotropic Thomson scattering, which contribute to Π. These terms affect the anisotropy spectra at the 10% level and are important for accurate model predictions and they represent the sources for photon polarization.

In order to solve for the angular power spectrum one has to expand the plane wave $e^{ik\mu(\eta-\eta_0)}$ in terms of the Bessel (radial) and Legendre (angular) eigenfunctions, perform the ensemble average assuming that only the amplitude and not the phase of a given mode evolves in time (which is correct at first-order level), and integrate over the angular variable μ. This leads to

$$C^{(S)}_{(T,P)l} = (4\pi)^2 \int k^2 dk P_\psi(k) |\Delta^{(S)}_{(T,P)l}(k, \eta = \eta_0)|^2 \,, \tag{3.16}$$

where the multipole moment at present time $\Delta^{(S)}_{(T,P)l}(k, \eta = \eta_0)$ is given by the following expression [138],

$$\Delta^{(S)}_{(T,P)l}(k, \eta = \eta_0) = \int_0^{\eta_0} S^{(S)}_{T,P}(k, \eta) j_l[k(\eta_0 - \eta)] d\eta \,, \tag{3.17}$$

where $j_l(x)$ is the spherical Bessel function.

The main advantage of Eq. (3.17) is that it decomposes the anisotropy into a source term $S^{(S)}_{T,P}$, which does not depend on the multipole moment l and a geometrical term j_l, which does not depend on the particular cosmological model. The source term is the same for all multipole moments and only depends on gravitational potentials, baryon velocity and photon moments up to $l = 4$ in Eq. (3.15). By specifying the source term as a function of time one can compute the corresponding spectrum of anisotropies.

The solution for the tensor modes can similarly be written as an integral over the source term and the tensor spherical eigenfunctions χ^l_k. The latter are related to the spherical Bessel functions [137],

$$\chi^l_k(\eta) = \sqrt{\frac{(l+2)!}{2(l-2)!}} \frac{j_l(k\eta)}{(k\eta)^2}. \tag{3.18}$$

This gives [138]

$$\Delta^{(T)}_{(T,P)l} = \int_0^{\eta_0} d\eta S^{(T)}_{T,P}(k,\eta)\chi^l_k(\eta_0 - \eta), \tag{3.19}$$

where from Eq. 3.13 follows

$$S^{(T)}_T = -\dot{h}e^{-\kappa} + g\Psi \qquad S^{(T)}_P = -g\Psi\,. \tag{3.20}$$

For analogous solutions in the synchronous-gauge see Ref. [125].

3.3 The physics of CMB anisotropy and polarization

Given their mathematical description, let us now try to comment the main features of the CMB anisotropy power spectra and the physics behind them.

This description falls within the current paradigm of cosmological structure formation (*e.g.* [139]). When we observe the distribution of galaxies around us, we find that they are not arranged at random, but rather clustered together in coherent patterns that can stretch for up to 100Mpc. The distribution is characterized by large voids and a network of filamentary structures meeting in large overdense regions. This large-scale structure arose through the action of gravity on initially small amplitude perturbations in the density field left over from inflation: a region of space that is initially overdense gives rise to a larger (than the average) gravitational potential and the surrounding matter falls into this potential, increasing the overdensity. Similarly matter flows out of regions of underdensity, increasing further the density contrast. In this way gravity can amplify any already existing density perturbation and eventually the density contrasts become so large that nuclear fusion are ignited on and form stars, galaxies, etc.

The CMB anisotropies that we see today contain a snapshot of the density field conditions when the universe was 380,000 years old at LS (plus some small processes that occurred during their travel toward us) and the initial density fluctuations are seen as CMB temperature anisotropies across the sky.
The key concept is that anisotropy on a given angular scale is related to density perturbations on the LS surface of a given wavelength: multipole moment ℓ receives its dominant contribution from Fourier mode k, where $\ell \approx kr$ and r is the comoving distance to LS.

The CMB temperature spectrum in Fig. (1.1) clearly shows three distinct pieces: at large angular scales (low-ℓ) there is a plateau that rises into a series of bumps and wiggles which damp quasi-exponentially on small angular scales. It can be shown that

these three regimes are separated by two angular scales, the first at about one degree and the second at a few arcminutes.

To understand the origin of these features let us go back in time to just before recombination. At this time the universe contained the tightly coupled photon-baryon fluid and dark matter, with perturbations in the densities and gravitational potential on a wide range of scales. While perturbations in the dark matter grow continuously as the universe evolves, the gravity-driven collapse of a perturbation in the baryon-photon fluid is resisted by the pressure restoring force of the photons. For example, as an overdensity falls into a gravitational potential it becomes more and more compressed. Eventually photon pressure halts the collapse and the mode rebounds, becoming increasingly rarefied. The expansion is slowed and halted owing to the weight of the fluid and the gravitational potential, causing the mode to recollapse once more. In short, an acoustic wave is set up, with gravity the driving force and pressure the restoring force and at decoupling some of these acoustic modes are at a maximum, giving rise to the observed acoustic peaks and valleys in the CMB anisotropy angular spectrum of Fig. (1.1).

Mathematically, the Fourier mode k of the temperature fluctuation is governed by a harmonic-oscillator-like equation which can be obtained assuming infinite efficiency of the Thomson scattering in glueing baryons and photons together [140]

$$\left[m_{\rm eff}\Delta T_0(k,\eta)'\right]' + \frac{k^2}{3}\Delta T_0(k,\eta) = -F_k \tag{3.21}$$

where F is the gravitational forcing term owing to the dark-matter potentials, $m_{\rm eff}$ describes the inertia of the fluid, and primes denote derivatives with respect to the conformal time.

The large-angular scale Sachs-Wolfe plateau ($\ell < 100$) in the angular power spectrum arises from perturbations with periods longer than the age of the universe at LS, *i.e.* $\sim$ with wavelength larger than the horizon at LS. These waves are essentially frozen in their initial configuration and provide us with a probe of the physics that created them (*e.g.* inflation), unspoiled by cosmological evolution. Since CMB photons lose energy climbing out of the potential wells associated with these long-wavelength density perturbations, the temperature differences seen on the sky reflect the gravitational potential differences on the LS surface [141, 142]. If the density fluctuations are approximately scale-invariant the plateau in the angular power spectrum is flat.

At scales smaller than the horizon at LS, the baryon–photon fluctuations that produce anisotropy on sub-degree angular scales ($10^2 < \ell < 10^3$) have sufficient time to

undergo oscillations. At maximum compression (rarefaction) the CMB temperature is higher (lower) than average. Neutral compression corresponds to velocity maxima of the fluid, which leads to a Doppler-shifted CMB temperature. The Doppler effect is subdominant because we see only the line-of-sight component of the velocity and the speed of sound is less than the speed of light. Since LS is nearly instantaneous, the CMB provides a snapshot of these acoustic oscillations, with different wavelength modes being caught in different phases of oscillation. Because a given multipole ℓ is dominated by the effects of a narrow band of Fourier modes, this leads to peaks and valleys in the angular power spectrum. Since the power spectrum is the squared amplitude, and the troughs correspond to velocity maxima (which are $\pi/2$ out of phase with the density maxima), these peaks are modes that were maximally under– or over–dense at LS.

On even shorter scales ($\ell \gtrsim 10^3$) the finite duration of recombination has an observable effect [143, 144]. During this time the photons can random walk a distance given by the mean free path (which is increasing during recombination) times the square root of the number of scatterings with electrons. Thus photons can diffuse out of any overdensity on smaller scales than this, which leads to an exponential damping of the spectrum on small scales known as *Silk damping*. Approximating LS as an instantaneous event, the damping is exponential with an e-folding scale given by the geometric mean of the LS horizon and the photon mean free path.

Of course before/at/after LS, the photons not only respond to the gravitational potentials caused by matter density perturbations, but also to any other perturbations in the space-time metric *i.e.* also to vector and tensor metric modes. If not seeded by other mechanisms, vector perturbations decay and can be neglected, while tensor perturbations (which do not create baryon-photon oscillations) can contribute to the Sachs-Wolfe plateau (*e.g.* [141]). In particular tensor metric modes generate a quadrupole signature as they distort the distribution of passing photons. Gravitational waves redshift away inside the horizon so that their main effect on anisotropies occurs around horizon crossing: only scales above the horizon at recombination contribute significantly; therefore the produced anisotropies can constrain properties of the primordial fluctuations, such as the ratio of tensor to scalar fluctuations, r. The typical signature of gravity waves is an enhanced quadrupole $\ell = 2$ and a cut off at the multipole corresponding to the projected horizon at last scattering. If the same mechanism generates both the scalar and tensor fluctuations (*e.g.* inflation), there may exist a relation between their spectra. In particular, inflation predicts a consistency relation between the shape of the tensor

spectrum and the tensor-to-scalar amplitude ratio which may provide a sensitive test of this paradigm.

As the photons travel through the universe from the surface of LS they interact gravitationally with the matter. If the gravitational potentials are still evolving, additional temperature perturbations are generated by the ISW effect [141]: a photon falling into a gravitational potential gains energy; if the potential evolves during the photons' traverse, the energy lost climbing back out will be different from that gained falling in, leading to a net anisotropy. To linear order in the perturbations, the gravitational potential is constant when matter dominates the energy budget of the universe and this phase gives no contribution. However, right after recombination photons still contribute enough to the energy density of the universe and the change in time of the potential is non-zero: this is the so-called "early ISW effect". That can happen also at very late times if either curvature or a cosmological constant dominate producing the so-called "late ISW effect".

CMB photons are also characterized by some degree of polarization [145, 147, 146]. In fact, the Thomson scattering cross section σ, as a function of the solid angle Ω, depends on polarization

$$\frac{d\sigma}{d\Omega} \propto \left|\varepsilon_i \cdot \varepsilon_f\right|^2 \tag{3.22}$$

where $\varepsilon_{i,f}$ are the incident and final polarization directions. The scattered radiation intensity peaks normal to, and with polarization parallel to, the incident polarization. If the incoming radiation field is isotropic, the orthogonal polarization states balance and the outgoing radiation remains unpolarized. In the presence of a quadrupole anisotropy, instead, a linear polarization is generated by scattering.

Since we have observational evidence for anisotropies at LS, we expect the CMB is linearly polarized. The degree of polarization is directly related to the quadrupole anisotropy at LS. While the exact properties of the polarization depend on the mechanism for producing the anisotropy, several general properties arise: the polarization peaks at angular scales smaller than the horizon at LS (*i.e.* smaller scales than the first temperature peak) owing to causality. Since only those photons that scattered in an optically thin region near LS could have had a quadrupole anisotropy, the polarization fraction is small and dependent on the duration of LS; for a standard thermal history, it is a few percent of the temperature anisotropy. An additional change in polarization can occur during subsequent interaction with ionized matter (e.g. during reionization [148]). Moreover gravitational interactions do not generate or destroy polarization.

As discussed in Sec.3.2, the E-mode and B-mode polarization power spectra transform into one another under a 45-degree rotation of the polarization. The additional cross-power spectrum between T- and E-modes is due to the fact that density (or scalar) perturbations have no "handedness" and so generate only E mode of polarization. Vector and tensor perturbations instead create T- and both E- and B- modes. In Fig. (3.3), the power spectrum of the best-fit ΛCDM model, the data from WMAP–3 as well as some indication of the diffuse foregrounds by our own galaxy, are shown. In the top, the large scale plateau as well as the acoustic oscillations in the TT mode are shown. The TE and the EE modes are dominated by the scalar-type cosmological perturbations. Also, the predicted tensors for $r = 0.3$ determine the BB mode signal. The lensing curve, dashed, is also shown, and will be the subject of the next Chapter.

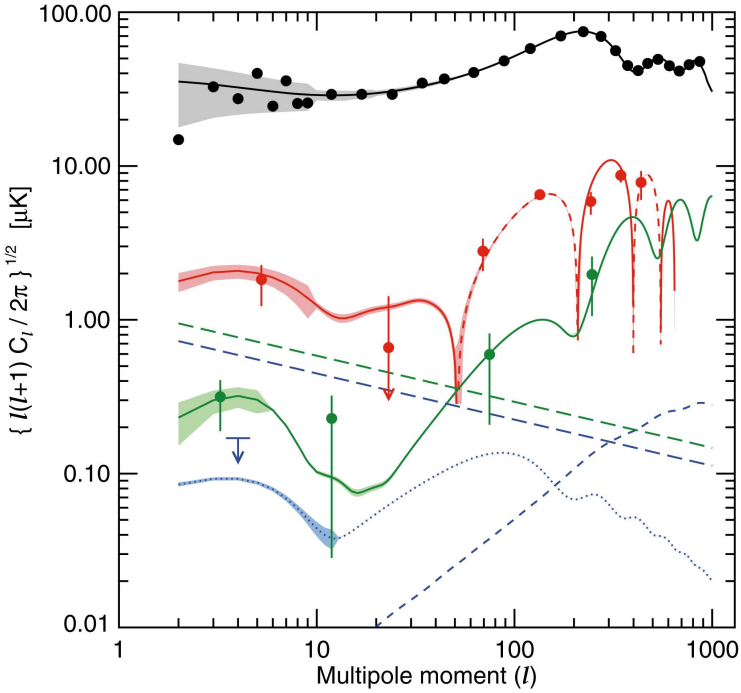

Figure 3.3: *Plots of signal for TT (black), TE (red), EE (green) for the best fit model, together with the WMAP–3 data. The dashed line for TE indicates areas of anticorrelation. The cosmic variance is shown as a light swath around each model. For BB (blue dots), a model with r = 0.3 is used. It is dotted to indicate that at this time WMAP only limits the signal. The BB lensing signal is shown as a blue dashed line. The straight dashed lines, with green for EE and blue for BB, indicate foreground emission from the diffuse gas in our galaxy. Both are evaluated at* $\nu = 65$ *GHz. From Ref. [28]*

Since different sources of anisotropy (scalar, vector, tensor) generate different pat-

terns of polarization [149, 150, 129], information from polarization is complementary to information from temperature anisotropies. Moreover the polarization pattern depends also on the kind of primordial fluctuations: adiabatic and isocurvature[1] modes generate different polarization spectra [151, 152, 129]. Finally, polarization depends on some of the cosmological parameters differently than the temperature anisotropy, allowing degeneracies in the fitted parameters to be removed and improving parameter constraints by a large factor [153, 154, 155, 156].

3.4 Secondary CMB anisotropies

We conclude this Chapter with an overview of the mechanisms giving rise to secondary anisotropies which occur due to intervening effects between recombination and the present. These divide basically into two categories: gravitational effects from metric distortions and rescattering effects from reionization. Both leave imprints of the more recent evolution of the Universe and the structure within it. Compared with the primary signal, secondary anisotropies provide more details on the evolution of structure and less robust constraints on the background parameters.

If metric fluctuations evolve as the photons stream close to them, they leave their mark as gravitational redshifts. Common manifestations include the cited late ISW effect from rapid expansion and the *Rees-Sciama (RS) effect* from non-linear structures [157]: once fluctuations leave the linear regime, their subsequent evolution make the potentials vary with time owing to both the growth and movement of bound haloes, leading to anisotropies through the RS effect. Since the smallest scales go non-linear first, the effect peaks toward small scales and the scale at which fluctuations become nonlinear is in principle also imprinted on the CMB, even if the effect is very small and is not the dominant source of anisotropy on any scale.

In addition to the energy gained and lost by photons due to time-varying potentials, the path a photon takes is altered by *gravitational lensing*, which we will describe in detail in the next Chapter.

Observations of the spectra of high redshift Quasars indicate that the universe is highly ionized out to redshift $z \sim 5$, thus photons can again scatter off free electrons at later times after LS. Unlike the $z \sim 10^3$ LS surface, however, the electron density

[1] An isocurvature perturbation is one which leaves the total density unperturbed, while perturbing the relative amounts of different materials.

today is quite low so that the baryons and photons do not become tightly coupled and can have a large relative velocity. This rescattering both erases primary anisotropies and generates new secondary ones, or better, ıreionization damps power on angular scales smaller than the horizon subtended by the epoch of reionization and generates extra power via the Doppler effect due to the large relative velocity of the photons and baryons fluids. If the underlying primary signal is known, the angular extent of the new fluctuations measures the horizon size at the rescattering epoch and their amplitude probes the baryon velocity at that time.
It is unlikely that the reionization of the universe will occur uniformly throughout space, so anisotropies will be generated owing to the "patchiness" of reionization. Depending on the redshift of reionization and whether the ionizing sources are quasars or stars, the angular scale of this anisotropy could be quite different. Current calculations and numerical simulations [158, 159, 160] suggest the patchy reionization will not dominate except on extremely small angular scales.

In addition, once structure formation is well underway, the photons can interact with hot gas in the intergalactic medium [161, 162]. The CMB photons can either be upscattered in energy when interacting with hot gas via the *"thermal" Sunyaev-Zel'dovich (SZ) effect* or have their temperature shifted locally by a Doppler shift from the peculiar velocity of the scattering medium via the *"kinetic" SZ and Ostriker-Vishniac effects* [163]. The thermal SZ effect is probably the largest source of anisotropy on angular scales of a few arcminutes and has been calculated both analytically [164, 165, 166, 167, 168] and numerically [169, 170, 171, 172, 173]. It is independent on redshift, so it can yield information on clusters at much higher redshift than does X-ray emission. In the $4.5'$ channels of Planck, the thermal SZ effect will probably probe cluster abundance at high redshifts.

Chapter 4

Weak Gravitational Lensing of the CMB

A gravitational lens is formed when the light from a very distant, bright source (such as a quasar) is "bent" around a massive object (such as a massive galaxy) between the source object and the observer. The process is known as *gravitational lensing*, and is one of the predictions of Albert Einstein's GR theory according to which mass warps the space-time to create gravitational fields and to bend light as a result.

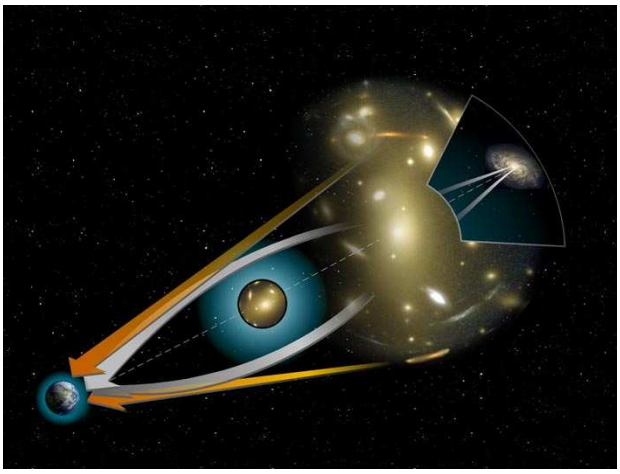

Figure 4.1: *Bending light around a massive object from a distant source. The orange arrows show the apparent position of the background source. The white arrows show the path of the light from the true position of the source. From http://hubblesite.org.*

The official formulation of the gravitational lensing theory is dated 1936 [176], but, actually, gravitational lensing was found by Einstein even before his GR theory was formulated in 1915. In fact, the reconstruction of some of Einstein's research notes dating back to 1912, Fig. 4.2, reveals that he explored the possibility of gravitational lensing,

deriving its basic features, even three years before completing the GR theory. When 24 years later he finally published the very same results on lensing, it was only in response to prodding by the amateur scientist R. W. Mandl [177].

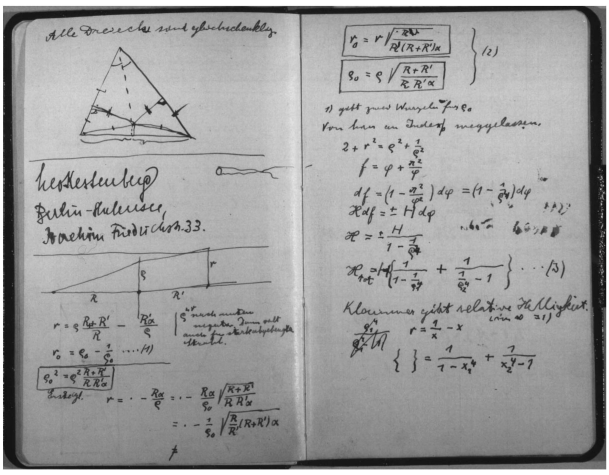

Figure 4.2: *Notes about gravitational lensing dated to 1912 on two pages of Einstein's scratch notebook. Between these pages a loose sheet containing further notes on the lensing effect was found. From Ref. [177].*

The gravitational lensing theory was confirmed in 1919 during a solar eclipse, when Arthur Eddington observed that stars passing close to the sun appeared slightly out of position, confirming that the light from stars was slightly bent by its gravitational field.

In gravitational lensing maximum "bending" occurs closest to, and minimum "bending" furthest from, the center of the lens. Consequently a gravitational lens has no single focal point, but a focal line instead. Commonly, the massive lensing galaxy is off-center, creating a number of images according to the relative positions of the source, lens, and observer, and the shape of the gravitational well of the lensing galaxy. In addition, the observer may see sources duplicated about a simple gravitational lens, although the lensed image will always be distorted when compared to the source (Fig. 4.1). Moreover, gravitational lensing can increase the apparent brightness of the sources.

Fig. 4.3 shows the actual gravitational lensing effects clearly observed by the Hubble Space Telescope (HST) in the galaxy cluster Abell 2218.

When the involved fields are strong enough, if the source, the massive lensing object, and the observer lie on a straight line, the source will appear as a ring behind the massive object.

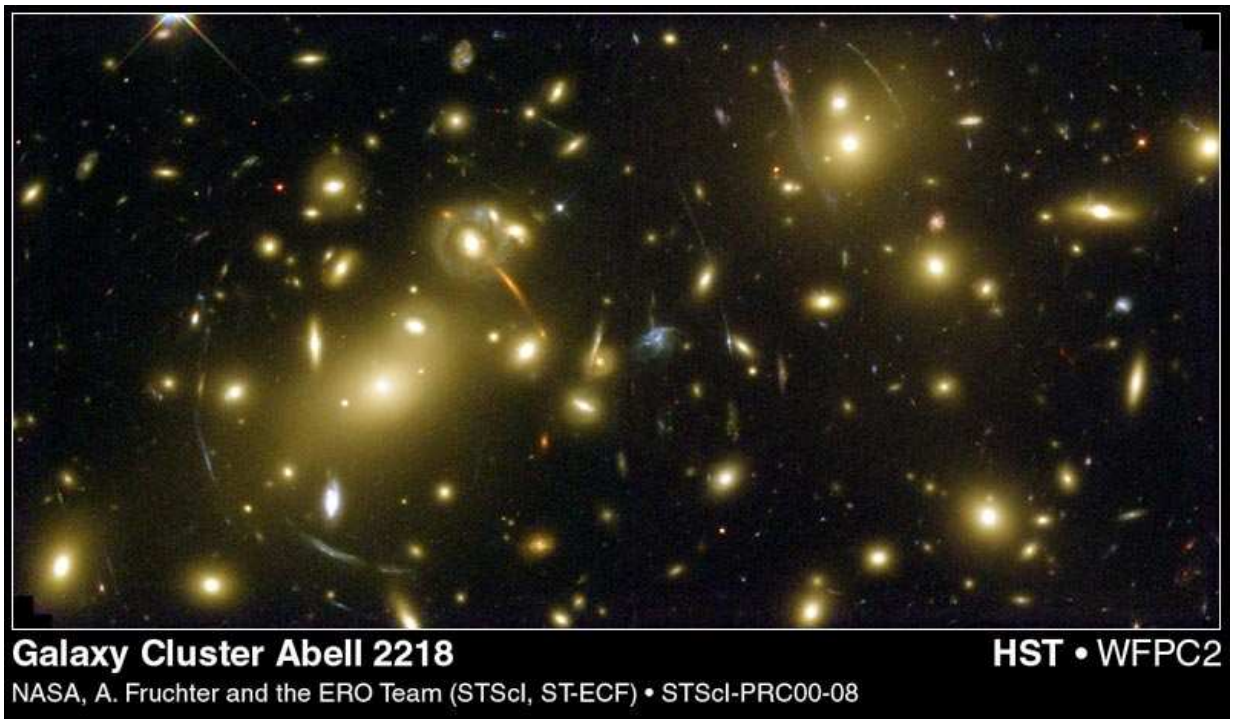

Figure 4.3: *The cluster Abell 2218 hosts one of the most impressive collections of arcs. This* HST *image of the cluster's central region shows a pattern of strongly distorted galaxy images tangentially aligned with respect to the cluster centre. The gravitational field of the cluster magnifies the light of more distant galaxies far behind it, providing a deep probe of the very distant universe. The cluster was imaged in full color in January 2000, providing astronomers with a spectacular and unique new view of the early universe. From http://hubblesite.org.*

This phenomenon was first mentioned in 1924 by the St. Petersburg physicist Orest Chwolson [178], and quantified by Einstein in 1936 [176]. It is usually referred to in the literature as the "Einstein ring", since Chwolson did not concern himself with the flux or radius of the ring image.

Actually, Einstein always discarded the ring and apparent brightness amplification effects as a speculative idea only, without any chance of empirical confirmation: indeed his theory predicted that it was possible for astronomical objects to bend light, and that under the correct conditions, one would observe multiple images and magnification of a single source; however, as he only considered gravitational lensing by single stars, he incorrectly concluded that these phenomena would most likely remain unobserved for the foreseeable future. In Ref. [176] he verbatim says: "Of course, there is no hope of observing this phenomenon directly".

In 1937 instead, Fritz Zwicky first considered the case where a galaxy could act as a lens, something that according to his calculations should be well within the reach of observations, contrary to Einstein hopelessness...
In his paper [179], Zwicky says explicitely: "The gravitational fields of a number of foreground nebulae may therefore be expected to deflect the light coming to us from certain background nebulae. The observation of such gravitational lens effects promises to furnish us with the simplest and most accurate determination of nebular masses. No thorough search for these effects has yet been undertaken".

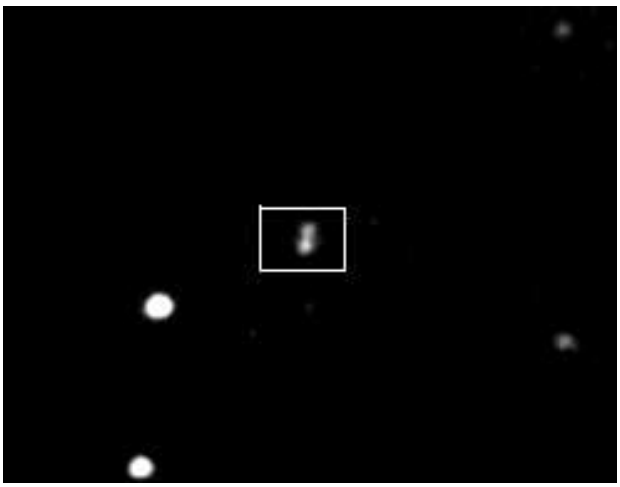

Figure 4.4: **QSO 0957+561**. *This quasar lies at a distance of 7.8 billion years far away from the Earth ($z = 1.414$) and is receding away from us at nearly 210,000 km/sec. Due to an intervening mass lying in the optical path between the Earth and the quasar, the light from the quasar is bent yielding two images of the source with relative magnitudes of 16.7 (QSO 0957+561A) and 16.5 (QSO 0957+561B) and an apparent separation of only 6 arcseconds.*

It was not until 1979 that the first astronomical lensed object would be identified, Fig. 4.4. It became known as the "Twin Quasar" since it initially looked like two identical quasars; it is officially named Q0957+561 and lies at $z = 1.41$ in the constellation Ursa Major. The lensing galaxy, known as YGKOW G1 is a giant elliptical galaxy at $z = 0.355$. The Twin–Quasar two images are separated by $6''$ and were discovered accidentally by Dennis Walsh, Bob Carswell, and Ray Weymann using the Kitt Peak National Observatory 2.1 meter telescope.

4.1 Gravitational lensing systems

The basic idea of gravitational lensing is extremely simple: any mass distribution modifies the structure of the spacetime, and therefore the trajectories of free falling objects. As a result, if these objects are photons following their null geodesics, the observed light rays, which encounter a density distribution in their path towards us, suffer a deviation. Gravitational lenses can be used as gravitational telescopes, since they concentrate the light from objects seen behind them, making very faint objects appear brighter and therefore more easily studied.
Gravitational lensing system are made up by three essential ingredients:

1. a physical objects that emits light, identifiable with the **source**; it can be a star, a galaxy, or a quasar, or the CMB itself for instance;

2. a matter concentration acting as the deflector (or **lens**), which does not need to be luminous but only to feel gravitational interactions, and thus can be a star, a galaxy, but also a dark matter halo or their large scale distribution, or a black hole;

3. an **observer**, namely someone collecting the emitted light from the source by means of a telescope or a detector.

In addition to these elements, we need knowledge of the properties of the **spacetime**, which may be regarded as the fourth element of the picture, in which the gravitational lensing system is embedded. The relative position of the set source–lens–observer will play its role as well: although in principle any mass distribution in the Universe bends the spacetime acting as lens for any source, a (rough) alignment among the three elements is needed in order for the effect to be appreciable.

Gravitational lensing is mainly divided in three sub-classes:

Strong lensing, where there are easily visible distortions such as the formation of Einstein rings, arcs, and multiple images, Fig. 4.3. Strong gravitational lenses may be used to examine objects at distances at which they would not normally be visible, providing information from further back in time than otherwise possible. Also, not just the object being lensed but the lens itself can provide useful information. By inverting the lens equations, information can be gathered on the mass and distribution of the lensing body. The statistics of strong gravitational lenses can also be used to measure values of cosmological parameters such as the cosmological constant and the mean density of

matter in the universe [180].
Another parameter that come out from the study of strong gravitational lenses is the Hubble's constant which encodes the age and size of the universe. Theoretically, it can be determined by measuring two quantities, the angular separation between two images, and the time delay between these images which has in turn two contributions: the first is the obvious delay due to the difference in optical path length between the two rays, and the second is a general relativistic effect, the "Shapiro effect", that describes light rays as taking longer to traverse a region of stronger gravitational field, the gravitational time dilation effect. Because the two rays travel through different parts of the potential well created by the deflector, the clocks carrying the source's signal will differ by a small amount.

Weak lensing, where the distortions of background objects are much smaller than in the strong lensing case, and can only be detected by analyzing large numbers of objects to find distortions of only a few percent. The principal aspect of weak–lensing is that measurements of its effects are statistical in nature. While a single multiply-imaged source provides information on the mass distribution of the deflector, weak–lensing effects show up only across ensembles of sources.
For instance, by measuring the shapes and orientations of large numbers of distant galaxies, these quantities can be averaged to measure the lensing field in any region. In particular, magnification and distortion effects due to weak–lensing can be used to probe the statistical properties of the matter distribution between us and an ensemble of distant sources, provided some assumptions on the source properties can be made. For example, if a *standard candle*[1] at high redshift is identified, its flux can be used to estimate the magnification along its line–of–sight. It can be assumed that the orientation of faint distant galaxies is random. Then, any coherent alignment of images signals the presence of an intervening tidal gravitational field. Furthermore, the positions on the sky

[1]The term *standard candle* is used for any class of astronomical objects whose intrinsic luminosity can be inferred independently of the observed flux. In the simplest case, all members of the class have the same luminosity. More typically, the luminosity depends on some other known and observable parameters, such that the luminosity can be inferred from them. The luminosity distance to any standard candle can directly be inferred from the square root of the ratio of source luminosity and observed flux. Since the luminosity distance depends on cosmological parameters, the geometry of the Universe can then directly be investigated. Probably the best candidates for standard candles are supernovae of Type Ia already mentioned in the Introduction. They can be observed to quite high redshifts, and thus be utilized to estimate cosmological parameters.

of cosmic objects at vastly different distances from us should be mutually independent. A statistical association of foreground objects with background sources can therefore indicate the magnification caused by the foreground objects on the background sources [181].
Since galaxies are intrinsically elliptical and the weak gravitational lensing signal is small, a very large number of galaxies must be used in weak–lensing surveys, for which a number of important sources of systematic error must be carefully avoided: the intrinsic shape of galaxies, the tendency of a camera's point spread function to distort the shape of a galaxy, the tendency of atmospheric seeing to distort images, and non-uniform photometry, or obscuration effects, must be carefully controlled at a level well below the expected weak–lensing effects. The results of these surveys are important for cosmological parameter estimation, for a consistency check on other cosmological observations, and to provide an important future constraint on dark energy and dark matter.
Weak lensing effects are being studied for the CMB as well and are the main subject of this Chapter.

Microlensing, where no distortion in shape can be seen, but the amount of light received from a background object changes in time due to the transit of a microlens in front of the source. By far the easiest effect to detect in a microlensing experiment is the apparent brightening of the source. The background source and the lens may be stars in the Milky Way in one typical case, or stars in a remote galaxy and an even more distant quasar in another case. Gravitational microlensing can provide information on comparatively small astronomical objects, such as massive compact halo objects (MACHOs) within our own galaxy, or extrasolar planets.

In general, every gravitational lensing effect is very small, such that a massive galaxy will produce multiple images separated by only a few arcseconds. Galaxy clusters can produce separations of several arcminutes. In the microlensing case, instead the typical separation scale would be of the order of a few millionths of degree, too small to be detected by any realistic measurement; these is the reason for exploiting different observational approaches of detection in this case.

In almost all the astrophysical lensing cases, the light behavior is well described through the geometrical optics approximation, basically requiring that the wavelength of the light is much smaller both than its typical travel distance and the Universe' radius of curvature, which is proportional to H_0^{-1}. If this is the case:

- light can be treated as particle–like, forgetting about its wave nature;

- since the radial extension of the involved astrophysical entities is much smaller than their relative distances, source, lens and observer can be thought of as lying on planes. In particular, the spatial coordinates can be separated into a radial coordinate along the line of sight and two angular ones (ϑ, φ) lying on a plane perpendicular to it, and characterizing the angular displacement from the polar axis. This latter is often referred to as the *flat-sky* approximation.

The geometry of the problem is depicted in Fig. 4.5 where it is sketched how a source, whose angular position is $\vec{\beta}$, is seen by the observer at the origin as arriving from an apparent angular position $\vec{\theta}$, i.e. differing from the true one by an amount $\boldsymbol{\alpha}$ called *deflection angle*. Here the *angular diameter distance* $D(z)$ of an object, at comoving distance $r = r(z)$, is defined as the ratio between the proper physical size of the object and the subtended angle of observation. It depends on the spatial curvature of the Universe and, in the flat case, it reduces to $D = a\chi$.

4.2 The Born approximation

In what follows we will consider the *small-angle scattering* limit, *i.e.* the case where the *change* in the comoving separation of source light–rays, owing to the deflection caused by gravitational lensing from a matter distribution, is small compared to the comoving separation of the *undeflected* rays, whose employment is therefore sufficient to calculate all the relevant integrated quantities. This represents the so-called "first Born approximation" and, in this case, a linearized treatment in the metric perturbations results to be appropriate.

Furthermore, we will only consider lensing by density perturbations and adopt the conformal Newtonian gauge, *i.e.* the Poisson gauge of Sec. 2.1 without vector and tensor metric perturbation. The line element, in a FRW background of generic spatial curvature, is then

$$ds^2 = a^2(\eta)[-(1+2\phi)\, d\eta^2 + (1-2\psi)\gamma_{\alpha\beta}\, dx^\alpha\, dx^\beta], \tag{4.1}$$

where the unperturbed spatial metric $\gamma_{\alpha\beta}$ is such that

$$\gamma_{\alpha\beta}\, dx^\alpha\, dx^\beta = \, d\chi^2 + r^2(\chi)(\, d\vartheta^2 + \sin^2\vartheta\, d\varphi^2)\,, \tag{4.2}$$

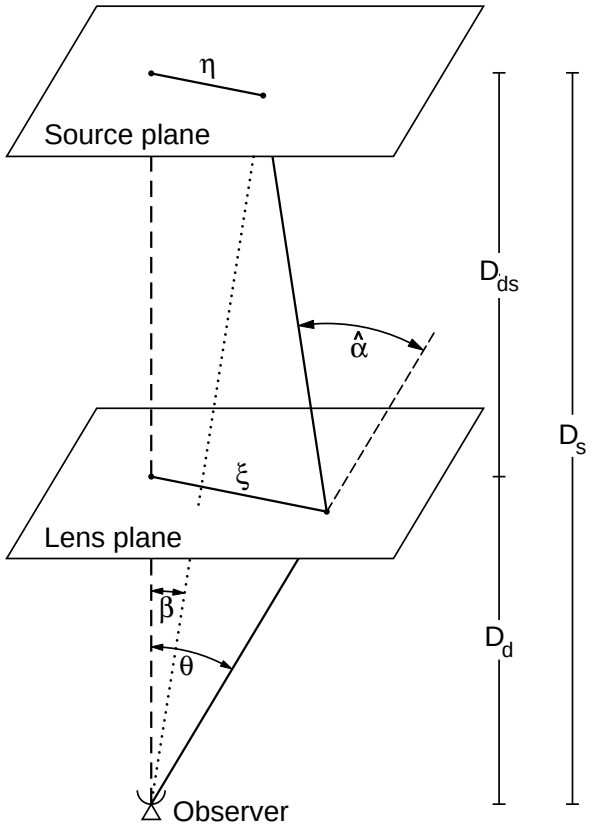

Figure 4.5: *A mass concentration at redshift $z_{\rm d}$ (or angular diameter distance $D_{\rm d}$) deflects the light rays from a source at redshift $z_{\rm s}$ (or angular diameter distance $D_{\rm s}$). If there are no other deflectors close to the line-of-sight, and if the extent of the deflecting mass along the line-of-sight is very much smaller than both $D_{\rm d}$ and the angular diameter distance $D_{\rm ds}$ from the deflector to the source, the actual light rays which are smoothly curved in the neighborhood of the deflector can be replaced by two straight rays with a kink near the deflector. The magnitude and direction of this kink is described by the* deflection angle $\boldsymbol{\alpha}$*, which depends on the mass distribution of the deflector and the impact vector of the light ray. From Ref. [181].*

where $r(\chi)$ is defined from Eq. (1.4).

Since for lensing we are only calculating the path of null geodesics ($ds^2 = 0$), we can divide the line element by $[-a^2(\eta)(1-2\psi)]$ and use the related conformal metric at first order in the perturbations ϕ and ψ

$$d\hat{s}^2 = (1+4\Phi)\, d\eta^2 - \gamma_{\alpha\beta}\, dx^\alpha\, dx^\beta \,, \tag{4.3}$$

where $\Phi \equiv (\phi+\psi)/2$ is the so-called 'Weyl potential' [175]. For matter perturbations in the linear limit with no stress perturbations, the equality $\psi = \phi = \Phi$ holds (which is

also the case for the *weak–field limit* on small scales), and, therefore, Φ is related to the matter–distribution density via the corresponding expression for the Poisson equation (see Sec. 2.3) [182].

In order to obtain the incoming–photons trajectories (with focus at the origin of the conformal time η_0), we have to solve the geodesic equation, expressed in this new conformal metric, whose 0-component reads

$$\frac{d^2\eta}{d\hat{\lambda}^2} + 2\left(\frac{d\eta}{d\hat{\lambda}}\right)^2 \frac{d\Phi}{d\eta} + 2\frac{d\eta}{d\hat{\lambda}}\frac{dx^\alpha}{d\hat{\lambda}}\frac{\partial\Phi}{\partial x^\alpha} = 0, \tag{4.4}$$

where the derivative $d\Phi/\,d\eta = \partial_\eta\Phi + (\,dx^\alpha/\,d\eta)\partial_\alpha\Phi$ is along the *perturbed* ray and $\hat{\lambda}$ is the affine parameter in the conformal metric which differs from that in the original frame. With Eq. (4.4), we can eliminate the affine parameter $\hat{\lambda}$ in favor of η, and obtain the spatial component of the geodesic equation [175]

$$\frac{d^2x^\alpha}{d\eta^2} - 2\frac{dx^\alpha}{d\eta}\left(\frac{d\Phi}{d\eta} + \frac{dx^\beta}{d\eta}\frac{\partial\Phi}{\partial x^\beta}\right) + 2\gamma^{\alpha\beta}\frac{\partial\Phi}{\partial x^\beta} + {}^{(3)}\bar{\Gamma}^\alpha_{jk}\frac{dx^\beta}{d\eta}\frac{dx^k}{d\eta} = 0, \tag{4.5}$$

where ${}^{(3)}\bar{\Gamma}^\alpha_{jk}$ are the connection coefficients of the unperturbed 3–D geometry $\gamma_{\alpha\beta}$ [62].

It is very convenient to consider an observer located at the origin of the spatial coordinates, in which case we are interested in rays that focus at $x^\alpha = 0$. For such rays, $d\chi/\,d\eta = -1 + O(\Phi)$ and $d\vartheta/\,d\eta = O(\Phi)$, with an equivalent result for φ. Substituting these results in Eq. (4.5), and evaluating the background connection coefficients, we find

$$\frac{d^2\chi}{d\eta^2} + 2\frac{d\Phi}{d\eta} = 0, \tag{4.6}$$

$$\frac{d^2\vartheta}{d\eta^2} - 2\frac{d\ln r(\chi)}{d\chi}\frac{d\vartheta}{d\eta} + \frac{2}{r^2(\chi)}\frac{\partial\Phi}{\partial\vartheta} = 0, \tag{4.7}$$

$$\frac{d^2\varphi}{d\eta^2} - 2\frac{d\ln r(\chi)}{d\chi}\frac{d\varphi}{d\eta} + \frac{2}{r^2(\chi)}\frac{1}{\sin^2\vartheta}\frac{\partial\Phi}{\partial\varphi} = 0, \tag{4.8}$$

which determine the perturbed rays up to first order in Φ [175].

Eq. (4.6) has $d\chi/\,d\eta + 2\Phi$ as a first integral, and this must equal -1 by the null condition for the perturbed ray. Integrating again, we find

$$\chi = \eta_0 - \eta - 2\int_{\eta_0}^{\eta} \Phi\; d\eta', \tag{4.9}$$

where the integral is along the ray. Since we are only working to first-order in Φ, we can evaluate the integral along the *unperturbed* path $\vartheta = \text{const}$, $\varphi = \text{const}$ and $\chi =$

$\eta_0 - \eta$. Integrating to a fixed η, Eq. (4.9) implies a radial displacement. Alternatively, integrating to a fixed χ, it implies a variation in the conformal time at emission; this is a time delay if the potential is negative on-average along the ray, i.e. it passes mostly through overdense regions.

Eqs. (4.7) and (4.8) can be integrated twice back to a conformal time $\eta_0 - \eta_* = \chi_*$ using the zero-order result $\chi = \eta_0 - \eta$, since it only appears in the argument of a function multiplying first-order terms. Then, changing integration order, the integral over $\int r^{-2}(\eta_0 - \eta')\, d\eta'$ can be done using the explicit form in Eq. (1.4). The result is [182]

$$\vartheta(\eta_0 - \chi_*) = \vartheta_0 - \int_0^{\chi_*} d\chi \frac{r(\chi_* - \chi)}{r(\chi_*)r(\chi)} 2 \frac{\partial}{\partial \vartheta} \Phi(\chi \hat{\mathbf{n}}; \eta_0 - \chi), \tag{4.10}$$

$$\varphi(\eta_0 - \chi_*) = \varphi_0 - \int_0^{\chi_*} d\chi \frac{r(\chi_* - \chi)}{r(\chi_*)r(\chi)} \frac{2}{\sin^2 \vartheta} \frac{\partial}{\partial \varphi} \Phi(\chi \hat{\mathbf{n}}; \eta_0 - \chi), \tag{4.11}$$

where ϑ_0 and φ_0 label the line of sight $\hat{\mathbf{n}}$, and $\eta_0 - \chi$ is the conformal time at which the photon was at position $\chi\hat{\mathbf{n}}$. This is a first–order solution and one could continue this procedure to generate solutions for the photon trajectories of arbitrary accuracy. From Eqs.(4.10)-(4.11) we get the displacement vector or *deflection angle* $\boldsymbol{\alpha}$ on the sphere

$$\boldsymbol{\alpha}(\chi_*, \hat{\mathbf{n}}) = -2 \int_0^{\chi_*} d\chi \frac{r(\chi_* - \chi)}{r(\chi_*)r(\chi)} \nabla_{\hat{\mathbf{n}}} \Phi(\chi \hat{\mathbf{n}}; \eta_0 - \chi) \tag{4.12}$$

where $[1/r(\chi)]\nabla_{\hat{\mathbf{n}}}$ is the 2-D transverse derivative with respect to the line–of–sight [175].

Moreover, if we define the *lensing potential* as,

$$\Psi(\chi_*, \hat{\mathbf{n}}) \equiv -2 \int_0^{\chi_*} d\chi \frac{r(\chi_* - \chi)}{r(\chi_*)r(\chi)} \Phi(\chi \hat{\mathbf{n}}, \eta_0 - \chi)\ , \tag{4.13}$$

the deflection angle results to be exactly its derivative on the sphere at $\hat{\mathbf{n}}$: $\boldsymbol{\alpha} = \nabla_{\hat{\mathbf{n}}} \Psi$.

Actually, the lensing potential appears to be formally divergent because of the $1/\chi$ term near $\chi = 0$. However this divergence only affects the monopole potential, which does not contribute to the deflection angle. Therefore the monopole term can be set to zero, and the remaining multipoles will be finite and the lensing potential field well defined [175].

In reality, owing to the statistical features of weak–lensing, we deal with lensing potential averaged over the source distance distribution $n(\chi)$

$$\Psi(\hat{\mathbf{n}}) = \int d\chi_* n(\chi_*) \Psi(\chi_*, \hat{\mathbf{n}}) = -2 \int d\chi g(\chi) \Phi(\chi \hat{\mathbf{n}}, \eta_0 - \chi)\ , \tag{4.14}$$

where

$$g(\chi) \equiv \frac{1}{r(\chi)} \int_\chi^\infty d\chi' n(\chi') \frac{r(\chi' - \chi)}{r(\chi')} \tag{4.15}$$

is a bell-shaped function which peaks at roughly half of the background source distance, and is normalised so that $\int d\chi n(\chi) = 1$ [182, 36, 183]. Eq.(4.14) can be obviously extended to the averaged deflection angle as well.

In the case of interest, the weak–lensing of the CMB from cosmological structures, if we neglect reionization, and approximate recombination as instantaneous so that the CMB is described by a single source plane at comoving distance $\chi = \chi_*(z \sim 10^3)$, the source distribution $n(\chi)$ is the Thomson visibility at last–scattering and can be replaced by a delta function at χ_*. In this case, the function g in Eq. (4.15) peaks at about $z \approx 1$, with a width $\delta z \approx 0.5$.

If the potential Φ is Gaussian, the lensing potential is Gaussian as well. On small scales however, non-linear evolution introduce a degree of non-Gaussianity even for Gaussian primordial fields; in this case the use of semi–analytical procedures or of N-body simulation should be exploited to account for the non-linear structure formation (see Chapter 5).

The derivative of the averaged deflection angle defines the *magnification matrix* (see *e.g.* Ref. [181, 175, 36])

$$A_{ij} \equiv \delta_{ij} + \frac{\partial}{\partial\theta_i}\alpha_j = \begin{pmatrix} 1-k-\gamma_1 & -\gamma_2+\omega \\ -\gamma_2-\omega & 1-k+\gamma_1 \end{pmatrix} .$$

An infinitesimal source with surface brightness $I(\hat{\mathbf{n}} + \boldsymbol{\delta\xi})$ at position $\boldsymbol{\delta\xi}$ about $\hat{\mathbf{n}}$ before lensing, becomes, after lensing, $I(\hat{\mathbf{n}}' + \mathbf{A}\boldsymbol{\delta\xi})$. At the lowest order the magnification of the intensity $\mu \equiv |\mathbf{A}|^{-1} = 1/[(1-k)^2 + \omega^2 - |\gamma|^2] \approx 1 + 2k$ is determined by the convergence, $k = -\frac{1}{2}\nabla \cdot \boldsymbol{\alpha}$. The shear $\gamma_1 + i\gamma_2$ determines the area-preserving distortion, and the antisymmetric term ω determines the rotation. Since Eq. (4.12) is purely a derivative, the antisymmetric rotation ω vanishes at the lowest order, *i.e.* at the first Born approximation. At the next order, this is no longer true and in general $\boldsymbol{\alpha}$ has a curl component. However, because it only appears at second order, its power spectrum is fourth order in the gravitational potential, with most effect on small scales. It is therefore likely to be less important than uncertainty in the non-linear potential evolution that gives a much larger effect on these scales [188, 189].
In Fig.4.6 we explain the effect of magnification and shear on a circular image.

The shearing effect on CMB is real and may be observable through changes of the hot and cold spot ellipticity distribution [184, 185]. However, in the CMB case, including shear and convergence effects on perturbation scales is easily described as the remapping of the CMB anisotropy and polarization fields by the deflection angle as a function

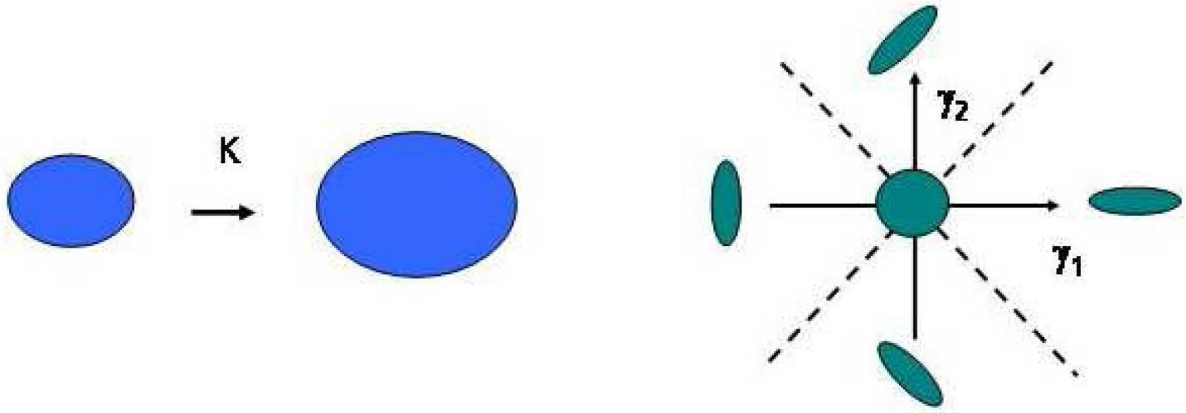

Figure 4.6: *Left: The convergence k does not change the shape of the object but only its size. Right: A positive (negative) shear component γ_1 corresponds to an elongation (compression) along the x-axis of an initially circular pattern. A positive (negative) value of the shear component γ_2 corresponds instead to an elongation (compression) along the $x = y$ axis. From Ref. [36].*

of position, and this will be our strategy for carrying out all-sky CMB lensed maps.
In fact, the flat-sky limit, sketched in Fig. 4.5, is a good approximation for observations covering only a small fraction of the sky, but not appropriate anymore when observing a significant fraction, also because the lensing deflections are correlated over degree scales, implying that correction due to the sky curvature is non-negligible (see Fig.4.7)

4.3 Lensing effects on the CMB

Weak lensing of the CMB deflects photons coming from an original direction $\hat{\mathbf{n}}'$ on the last scattering surface to an observed direction $\hat{\mathbf{n}}$ on the sky today; a lensed CMB field is given by

$$\tilde{X}(\hat{\mathbf{n}}) = X(\hat{\mathbf{n}}') \tag{4.16}$$

where $X = T, E, B$ are the unlensed ones. The vector $\hat{\mathbf{n}}'$ is obtained from $\hat{\mathbf{n}}$ by moving its end on the surface of a unit sphere by a distance $|\nabla_{\hat{\mathbf{n}}}\Psi(\hat{\mathbf{n}})|$ along a geodesic in the direction of $\nabla_{\hat{\mathbf{n}}}\Psi(\hat{\mathbf{n}})$ [183, 190, 191]. This is sometimes written as $\hat{\mathbf{n}}' = \hat{\mathbf{n}} + \nabla_{\hat{\mathbf{n}}}\Psi(\hat{\mathbf{n}})$. It is often assumed that $|\nabla_{\hat{\mathbf{n}}}\Psi|$ is constant between $\hat{\mathbf{n}}$ and $\hat{\mathbf{n}}'$, consistent with working out the lensing potential in the Born approximation. CMB lensing deflections are a few arcminutes, but are coherent over the degree scale, justifying this approximation.

Since, as a first approximation, the CMB lensing is a linear function of two Gaussian fields (the unlensed background CMB and the matter distribution), the result is a *non-*

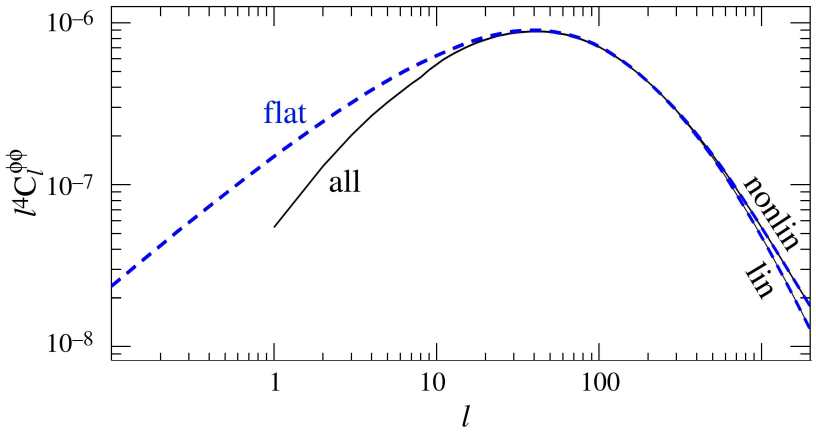

Figure 4.7: *The lensing potential power spectrum (defined decomposing the lensing potential in spherical harmonics, in the same way as for the CMB anisotropies, Eq.* (3.3) *and Eq.* (3.7)*), has been calculated, in the case of the linear and non-linear matter evolution, by the flat- and all-sky approaches: a non-negligible fraction of the power comes from scales where the flat-sky approximation is inadequate. From Ref. [183].*

Gaussian field, *i.e.* lensing induces a non-Gaussian spatial correlation structure between the temperature and lensing potential but does not alter the variance at a point [191].

CMB weak–lensing smoothes out features in the temperature power spectrum, where lensing effects become visible at $l \gtrsim 500$, corresponding to an angular scale of $\varphi \lesssim (\pi/500)\,\mathrm{rad} \approx 20'$, corresponding to the scale where coherent gravitational light deflection sets in. An important effect of lensing is seen at the high-l tail of the temperature power spectrum, where the lensed power spectrum falls systematically above the unlensed one by power transfer from large to small scales Fig 4.8 [181, 193, 194, 195, 196, 197, 198, 199].

Concerning the polarization, lensing changes the E-mode polarization C_l peaks by up to 20% on the scales of interests as well. Moreover, gravitational lensing of scalar E-mode polarization generates the *lensed* B-modes via the displacement and distortion of the E-pattern. In Fig. 4.9 the lensing effects on the T-, E-, and B-modes are shown.

This additional source of curl-component must be taken into account if the CMB polarization is to be used to detect the inflationary gravitational-wave background (IGW)

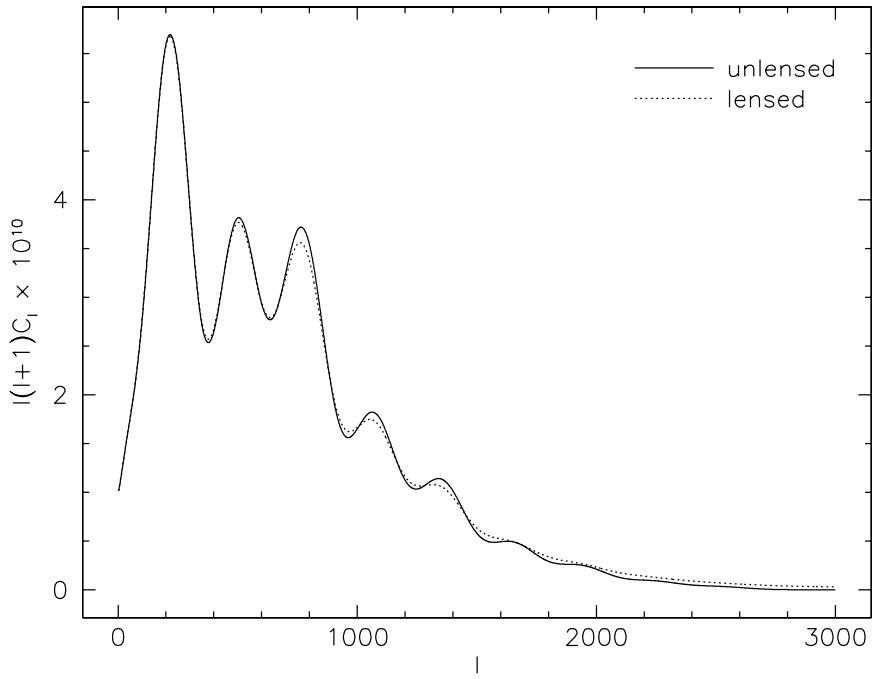

Figure 4.8: *The CMB power spectrum coefficients $l(l+1)C_l$ are shown as a function of l. The solid line displays the intrinsic power spectrum, the dotted line the lensed power spectrum for an Einstein-de Sitter universe filled with cold dark matter. Evidently, lensing smoothes the spectrum at small angular scales (large l), while it has no visible effect on larger scales. From Ref. [181].*

since, in some sense, the lensing–induced B-modes act as a foreground from which IGWs must be distinguished. If the energy scale of inflation is sufficiently large, the lensed B-modes will be no problem. However, as this scale is reduced, the IGW signal becomes smaller and will at some point get lost in the cosmic-shear induced noise [201, 202, 203], Fig. 4.10. Refs. [202, 203] show that if the gravitational-wave background is large enough to be accessible with the Planck satellite ($r = 0.1 ormore$), then the cosmic-shear contribution to the curl component is likely not to be relevant. For lower values of r, the cosmic-shear distortion to the CMB curl will need to be subtracted.

The CMB–lensing analysis is also relevant for several important reasons.
First of all, CMB distortions due to cosmic-shear are of interest on their own, since they allow to extract information about the unlensed CMB and probe the distribution of dark matter throughout the Universe as well as the growth of density perturbations at early times. These goals are important for determining the matter power spectrum and thus

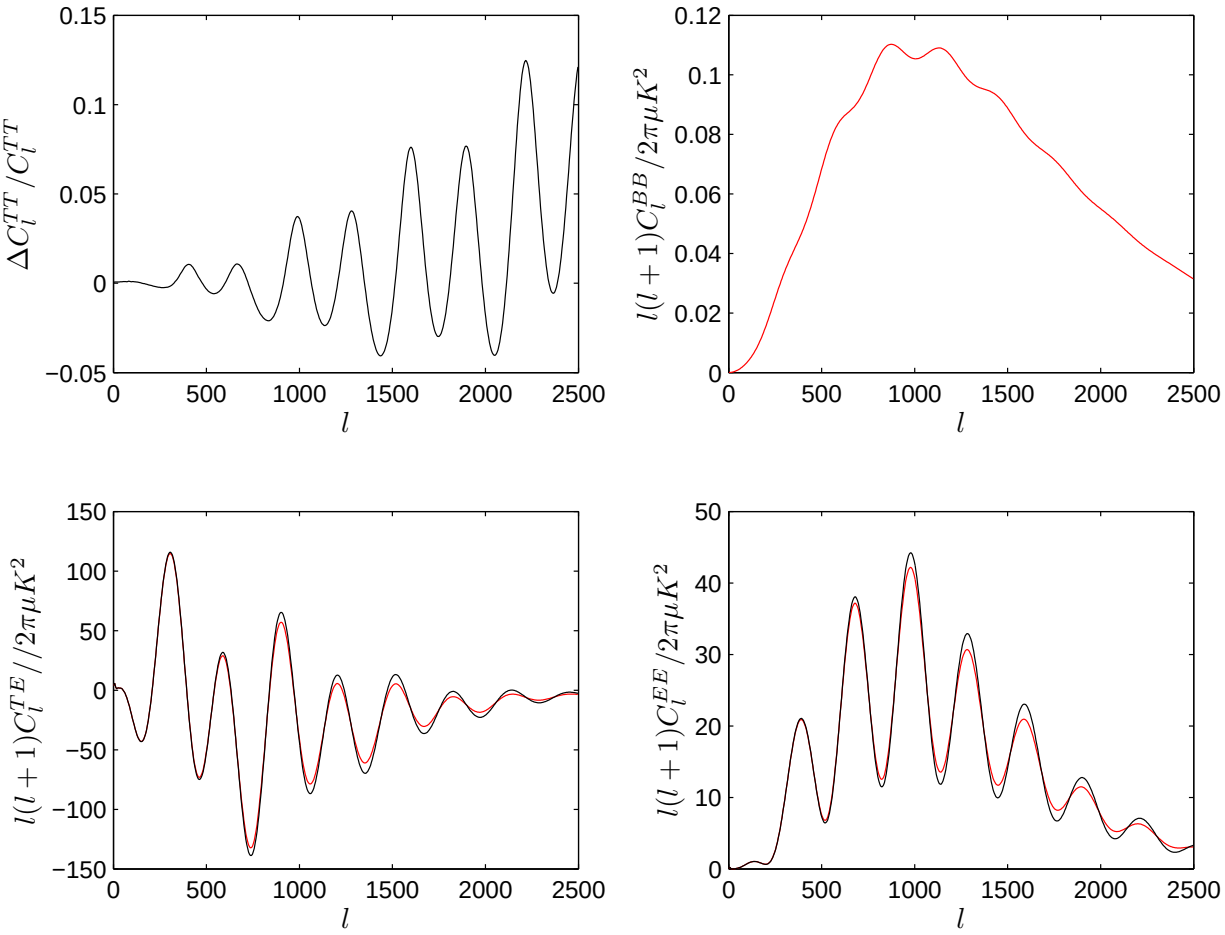

Figure 4.9: *The effect of lensing on the CMB power spectra. The top plots show the fractional change in the temperature spectrum C_l^{TT} and the lensing-induced B-polarization spectrum C_l^{BB}. The bottom plots show the lensed (grey/red, less peaked) and unlensed (black) T-E cross-correlation C_l^{TE} and E-polarization C_l^{EE} power spectra. From Ref. [191].*

for testing inflation and constraining the inflaton potential.

With the lensing cross–section peaking at roughly the onset of cosmic acceleration, $z \approx 1 as already mentioned$, the CMB lensing has been studied for constraining the dark energy abundance at the corresponding epoch [205, 206]. Cross-correlation of the lensing potential with the temperature can probe curvature and dark energy via the effect on the large-scale ISW effect [207, 208, 209, 210, 211].

Furthermore, the different lensing behavior with the cosmological parameters can help to break existing degeneracy between them [212].

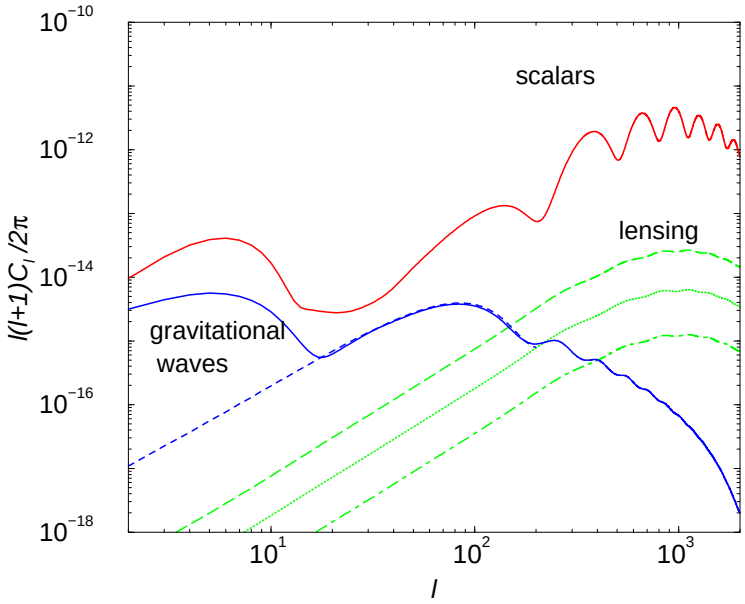

Figure 4.10: *Contributions to the CMB polarization power spectra. The upper (blue) solid "gravitational waves" curve is the curl component due to gravitational waves in the presence of reionization with an optical depth given by the first year WMAP data and the associated (blue) dashed curve is that with no reionization. The amplitude of this curve is for the largest inflaton-potential height ($V \simeq 3.5 \times 10^{16}$ GeV) allowed by COBE; note that $C_l^{\rm BB,GW} \propto V$, so the amplitude of this curve will be reduced accordingly if V is reduced. The short-dash (green) "lensing" curve is the curl power spectrum induced by cosmic shear (weak gravitational lensing due to density perturbations between us and the surface of last scattering). The red "scalar" curve is the EE power spectrum due to density perturbations (with reionization), shown here for reference. The dotted "lensing" (green) curve is the cosmic-shear contribution to the curl component that comes from structures out to a redshift $z = 1$, and the green "lensing" dot-dash curve is the residual cosmic-shear power spectrum left after subtraction with higher-order temperature-polarization correlations. From Ref. [204].*

Moreover, CMB lensing is of remarkable importance in the cosmological parameter analyses in order to obtain accurate results from CMB observations. For example, we know that lensing smooths out of about $\sim 2\%$ the third peak in the CMB temperature power spectrum, but this effect can be also produced by lowering the baryon density at the LS surface; therefore making a clear distinction of the two effects is strongly required [191].

Further on, unlensed CMB anisotropy is only weakly sensitive to neutrino masses suf-

ficiently light that they are relativistic at recombination. However the lensing potential probes later times, and the small scale damping effect on the lensing potential power spectrum can be significant. A neutrino with mass 0.1eV only changes the unlensed spectra at the sub-percent level, but the effect on the potential power spectrum is $\sim 5\%$ [255]. If the lensing potential can be reconstructed to within this accuracy, this extra information can be used to improve the limits on the neutrino mass from CMB data alone. Future experiments may ultimately be able to probe neutrino masses with error of ± 0.035eV [256].

Since the hot and cold CMB anisotropy–spot ellipticities have a very specific probability distribution for Gaussian fields [146], additional ellipticities caused by lensing shear should show up clearly as an excess of more elliptical shapes [184] and change their correlation in a characteristic way [186, 187]. The lensing-induced degree of non-Gaussianity must therefore be accounted for when attempting to access the degree of *primordial* non-Gaussianity from the CMB analysis.

Finally, the lensing signature in temperature and polarization of high-redshift clusters can be also used to constrain their mass [175].

Chapter 5

CMB Weak-Lensing from the Millennium Simulation

In a ΛCDM universe, quasi-equilibrium dark matter haloes grow by the collapse and the hierarchical aggregation of ever more massive systems, a process described surprisingly well by the phenomenological model of Press and Schechter and its extensions [213, 214]. Galaxies form at the centers of these dark haloes by the cooling and condensation of gas which fragments into stars once it becomes sufficiently dense. Groups and clusters of galaxies form as haloes aggregate into larger systems. They are arranged in the "cosmic web", the larger-scale pattern of filaments and sheets produced by the nonlinear gravitational evolution of the pattern already present in the Gaussian random field of initial fluctuations.

The presence of dark matter was first inferred from the dynamics of galaxy clusters by Zwicky in 1933 [215] and after confirmed by Smith [216] using Virgo cluster measurements. Zwicky found that galaxies in the Coma cluster were moving with surprisingly high speeds, indicative of a Coma cluster mass density at one order of magnitude greater than what would be expected from spreading the mass associated with the luminous parts of the galaxies over the volume of the cluster. Zwicky's measurements were probing larger scales with respect to the previous measurements, meaning that he was detecting mass that lies outside the luminous parts of the galaxies, *i.e.*, dark matter. Ordinary baryonic matter, being largely nonrelativistic, is then pulled in by the gravitational field of the cluster.

Babcock work [217] was the next major development in the dark matter story: he measured the rotation speed of luminous objects in or near the disk of the Andromeda (M31) galaxy, out to a distance of almost 20 kpc from the center. He found that the rotation

speed was still rising and not exhibiting the $1/\sqrt{r}$ Keplerian fall off with the distance r from the center expected if the M31 mass distribution followed the distribution of the light. That is, Babcock found that the outer part of the luminous component of M31 was dominated by non-luminous matter.
Later, in 1973, Ostriker and Peebles [218] noted that one way of making the disk of a spiral galaxy stable against a bar-like instability is to embed it in a massive halo, a suggestion that was proved consistent with the observational evidence.
These early results have been confirmed by a number of different techniques, including measuring the X-ray temperature of hot gas in galaxy clusters (which is a probe of the gravitational potential felt by the gas), galactic rotation curves, the structure of galaxy groups and clusters, large-scale cosmic flows and, perhaps most directly, measurements of gravitational lensing of background sources by galaxy clusters: the distorted images of background galaxies as their light travels near mass concentrations reveal the presence of dark matter in the outer haloes of galaxies, in galaxy clusters and in the general mass field.

CDM has now become a standard assumption which gives an excellent fit to observations, except possibly on the shortest scales where there remains some controversy concerning the structure of dwarf galaxies and possible substructure in galaxy haloes. Dark matter which has a large velocity dispersion, the so-called hot dark matter, has instead long been excluded as it does not permit galaxies to form. Other suggestions include a modest velocity dispersion (warm dark matter) and the possibility that the dark matter comprises two separate components, *e.g.* a cold one and a hot one, an example being if massive neutrinos have a non-negligible effect. If neutrinos had a mass ~ 5 eV, then their density would be comparable to the dark-matter density. However, neutrino masses are now known, from laboratory experiments as well as large-scale-structure data to be $\lesssim$eV (*e.g.* Ref. [219]), and, even if neutrinos did have the right mass, it is difficult to see, essentially from the Pauli principle [220] how they could be the dark matter. It appears likely then, that some exotic new candidate is required.
For the past two decades, the two leading candidates from particle theory have been weakly-interacting massive particles (WIMPs), such as the lightest superpartner (LSP) in supersymmetric extensions of the standard model [221, 222, 223], and axions [224].
In the minimal supersymmetric extension of the standard model (MSSM), the lightest supersymmetric particle is stable and represented usually by the neutralino, a linear combination of the supersymmetric partners of the photon, Z^0, and Higgs bosons.

In the MSSM model, the neutralino has only electroweak interactions and, from detailed calculations in a very broad class of supersymmetric extensions of the standard model [225], it is expected that its cosmological density is of order the dark-matter density. These particles are now among the primary targets for the Large Hadron Collider (LHC), which should begin science operations by the end of 2008. However, one can also try to detect neutralinos in the Galactic halo.
The other leading dark-matter candidate is the axion whose mass is constrained to be $m_a \sim 10^{-4}$ eV by a variety of astrophysical observations and laboratory experiments [224]. Smaller masses would lead to an unacceptably large cosmological abundance, while larger masses are ruled out by a combination of constraints from supernova 1987A, globular clusters, laboratory experiments, and a search for two-photon decays of relic axions. If the axion mass is in the relatively small viable range, the relic density is $\Omega_a \sim 1$, and so the axion may account for the halo dark matter. Such axions would be produced with zero momentum by a misalignment mechanism in the early Universe and therefore act as cold dark matter [226].

In N-body simulations, the dominant mass component is constituted by CDM, assumed to be made of elementary particles that currently interact only gravitationally, so the collisionless dark matter fluid can be represented by a set of discrete point particles. This representation as an N-body system is a coarse approximation whose fidelity improves as the number of particles in the simulation increases.
Cosmological simulations using increasingly sophisticated numerical methods provide a test bed for models of structure formation which attempt to reduce cosmology to an initial value problem: given the initial conditions, a background cosmological model with specified composition, and primordial fluctuations in the matter, radiation, and spacetime geometry, the goal is to compute the evolution of structure from the Big Bang to the present day using well-known physics laws.
While the initial, linear growth of density perturbations can be calculated analytically, the collapse of fluctuations and the subsequent hierarchical build-up of structure is a highly nonlinear process which is only accessible through direct numerical simulation. Simulations bridge the gap that often exists between basic theory and observation. They have found many uses, including testing and calibrating methods used to measure cosmological parameters, providing insight into nonlinear gravitational clustering and hydrodynamic turbulence, helping to explain the nature of systems such as quasi-stellar object absorption lines, and highlighting shortcomings in the current physical modeling

of galaxy formation. However, their main use has been and continues to be testing the viability of cosmological models of structure formation, such as the CDM model and its variants.

The current generation of cosmological simulations has antecedents that date back several decades. The first gravitational N-body simulation of interacting galaxies was performed using an analog optical computer (Holmberg 1941): gravity was represented by the flux from 37 lightbulbs, with photocells and galvanometers used to measure and display the inverse square law force. The first astronomical N-body computations using digital computers were made in the early 1960s by von Hoerner and Aarseth. These early simulations were limited to at most about 100 particles. Gas dynamical simulations of galaxy formation began with the pioneering spherically symmetric calculations of Larson in 1969. Increasingly large simulations of cluster collapse and evolution were performed throughout the 1970s, *e.g.* by Peebles and White. The first truly cosmological simulations of structure formation were the N-body integrations of Press & Schechter in 1974 in their influential paper on the mass distribution of bound clumps formed by hierarchical clustering [213, 227].

Computer simulations of structure formation in the Universe began with purely gravitational codes that directly compute the forces between a finite number of particles ("Particle-Particle" or PP codes) which sample the matter distribution. Binning the particles on a grid and computing the forces using the Fast Fourier Transform (the "Particle-Mesh" or PM method) is computationally more efficient, allowing simulation of larger volumes of space, but has force resolution of the order of the grid spacing. A compromise is the P^3M method, which uses PM for large scale forces supplemented by direct PP calculations on small scales, as used for the important suite of CDM simulations by Davis et al. [228]. The force resolution of PM codes and the force resolution and speed of P^3M codes is increased by employing multiple grid levels [229] as it happens in the adaptive mesh refinement (AMR; [230]) which dynamically increases the force resolution in the PM gravity solver [231, 232]. Another approach to achieving both speed and good force resolution in gravitational N-body simulation is the use of the "hierarchical tree algorithm" [233], and large cosmological simulations use a parallelized version of this method [234]. Finally, a significant increase in speed has been obtained with the use of the so-called "Tree Particle-Mesh algorithm" (TreePM) [235] described below.

5.1 The Millennium Simulation

The *Millennium Simulation* [236] is a high-resolution N-body simulation implemented by the Virgo Consortium, a collaboration of British, German, Canadian, and US astrophysicists. It follows $N = 2160^3 \simeq 1.0078 \times 10^{10}$ particles, with a mass of $8.6 \times 10^8\, h^{-1}\mathrm{M}_\odot$, from redshift $z = 127$ to the present in a cubic region $500\, h^{-1}$Mpc comoving on a side, where $1 + z$ is the expansion factor of the Universe relative to the present and h is Hubble's constant in units of $100\,\mathrm{km\,s^{-1}Mpc^{-1}}$. With ten times as many particles as the previous largest computations of this kind [238, 239, 240], it offers substantially improved spatial and time resolution within a large cosmological volume.

The Millennium Simulation was carried out with a specially customized version of the GADGET2–code [241], using the "TreePM" method [242] for evaluating gravitational forces. This is a combination of a hierarchical multipole expansion, or "tree" algorithm [233], used to compute short-range gravitational forces, and a classical, Fourier transform particle-mesh method [244] to determine long-range gravitational forces. This combination allows for a very large dynamic range and high computational speed even in situations where the clustering becomes strong . The calculation was performed on 512 processors of an IBM p690 parallel computer at the Computing Centre of the Max-Planck Society in Garching, Germany. It utilized almost all the 1 TB of physically distributed memory available and required about 350 000 processor hours of CPU time, or 28 days of wall-clock time.

The cosmological parameters of the Millennium Simulation are: $\Omega_m = \Omega_{CDM} + \Omega_b = 0.25$, $\Omega_b = 0.045$, $h = 0.73$, $\Omega_\Lambda = 0.75$, $n_s = 1$, and $\sigma_8 = 0.9$, all evaluated at the present time ($z = 0$). The adopted parameter values are consistent with a combined analysis of the 2dFGRS [245] and first year WMAP data [18].

The simulation volume is large enough to include interesting rare objects. At the present day, the richest clusters of galaxies contain about 3 million particles. The gravitational force law is softened isotropically on a comoving scale of $5\, h^{-1}$kpc, which can be taken as the spatial resolution limit of the calculation. Thus, the simulation achieves a dynamic range of 10^5 in 3D, and this resolution is available everywhere in the simulation volume [236].

Initial conditions have been laid down by perturbing a homogeneous, 'glass-like'[1],

[1]Such a glass is formed when a Poisson particle distribution in a periodic box is evolved with the sign of gravity reversed until residual forces have dropped to negligible levels

particle distribution [246] with a realization of a Gaussian random field with the ΛCDM linear power spectrum as given by the Boltzmann code CMBFAST[247]. The displacement field in Fourier space was constructed using the Zel'dovich approximation [248], with the amplitude of each random phase mode drawn from a Rayleigh distribution. The simulation was evolved from $z = 127$ to the present using a leap–frog integration scheme based on a split of the potential energy into a short-range and long-range component [249], with individual and adaptive timesteps, with up to 11 000 timesteps for individual particles.

The evolution of the simulation particles under gravity in an expanding background is governed by the Hamiltonian

$$H = \sum_i \frac{\vec{p}_i^2}{2\, m_i\, a(t)^2} + \frac{1}{2} \sum_{ij} \frac{m_i m_j\, \phi(\vec{x}_i - \vec{x}_j)}{a(t)}, \tag{5.1}$$

where $H = H(\vec{p}_1, \ldots, \vec{p}_N, \vec{x}_1, \ldots, \vec{x}_N, t)$. The $\vec{x}_i$ are comoving coordinate vectors, and the corresponding canonical momenta are given by $\vec{p}_i = a^2 m_i \dot{\vec{x}}_i$, where m_i represents the particle mass. The explicit time dependence of the Hamiltonian arises from the evolution $a(t)$ of the scale factor, which is given by the FRW model that describes the background cosmology. Due to the assumption of periodic boundary conditions for a cube of size L^3, the interaction potential $\phi(\vec{x})$ is the solution of

$$\nabla^2 \phi(\vec{x}) = 4\pi G \left[-\frac{1}{L^3} + \sum_{\vec{n}} \delta_\epsilon(\vec{x} - \vec{n}L) \right], \tag{5.2}$$

where the sum over $\vec{n} = (n_1, n_2, n_3)$ extends over all integer triplets. The density distribution function $\delta_\epsilon(\vec{x})$ of a single particle is spread over the gravitational softening length $\epsilon = 5\, h^{-1}$kpc. Note that the mean density is subtracted in equation (5.2), so the solution of the Poisson equation corresponds to the *physical peculiar potential multiplied by the scale factor a*, where the dynamics of the system is governed by

$$\nabla^2 \phi(\vec{x}) = 4\pi G [\rho(\vec{x}) - \overline{\rho}]\,. \tag{5.3}$$

The equations of motion corresponding to equation (5.1) are $\sim 10^{10}$ simple differential equations, coupled tightly by the mutual gravitational forces between the particles [236].

The particle data has been stored at 64 output times, each of size 300 GB, giving a raw data volume of nearly 20 TB. This allowed the construction of finely resolved hierarchical merging trees for tens of millions of haloes and for the sub-haloes that survive

within them. A galaxy catalogue for the full simulation, typically containing $\sim 2 \times 10^6$ galaxies at $z = 0$ together with their full histories, can then be built for any desired semi-analytic model[2] [250, 251].

Fig. 5.1 shows the impressive resemblance between spectroscopic redshift surveys and mock galaxy catalogs obtained exploiting the dark matter distribution of the Millennium Simulation.

For our particular purpose of making all-sky lensing–potential and deflection–angle maps, we have used the 3-D field of the gravitational potential stored at each of the 64 output times in units of $(\mathrm{km/sec})^2$. The mesh dimensions of each gravitational potential file are 2560^3 and cover a comoving cube with $(500\ \mathrm{Mpc}/h)^3$ by volume (that means the gravitational potential grid has a resolution of $\sim 0.195\ \mathrm{Mpc}/h$). Because of issues of file size and parallelization, each potential field is split up into several files, where each of the files contains a slab from the cube, and the slicing is done along the x-axes.

In Fig. 5.2, we show the resulting time evolution of the *dark matter* power spectrum of the Millennium Simulation. On large scales and at early times, the mode amplitudes grow linearly, roughly in proportion to the cosmological expansion factor. Nonlinear evolution accelerates the growth on small scales when the dimensionless power $\Delta^2(k) = k^3 P(k)/(2\pi^2)$ approaches unity; this regime can only be studied accurately using numerical simulations. In the Millennium Simulation, it has been possible to determine the nonlinear power spectrum over a larger range of scales than in earlier works [109], almost five orders of magnitude in wavenumbers [236].
This is a very important point in the CMB lensing analysis. In fact, the non-linear evolution of the gravitational potential changes on small scales the angular power spectrum $C_l^{\Psi\Psi}$ of the *lensing potential* Ψ and introduces some degree of *non-Gaussianity* in its dis-

[2] A semi-analytic model can be viewed as a simplified simulation of the galaxy formation process, where the star formation and its regulation by feedback processes is parameterized in terms of simple analytic physical models. These models take the form of differential equations that describe radiative cooling of gas, star formation, growth of supermassive black holes, feedback processes by supernovae and active galactic nuclei (AGN), and effects due to a reionising UV background. In addition, the morphological transformation of galaxies and the process of metal enrichment are modeled as well. Of substantial importance is the tracking of dark matter substructure. For what concerns the Millennium Simulation, this has been carried out consistently and with unprecedented resolution throughout the large cosmological simulation volume, allowing an accurate determination of the orbits of galaxies within larger structures, as well as robust estimates of the survival time of structures infalling into larger objects. Dark matter substructure properties, like angular momentum or density profile, have been used as well to directly determine sizes of galactic disks and their rotation curves.

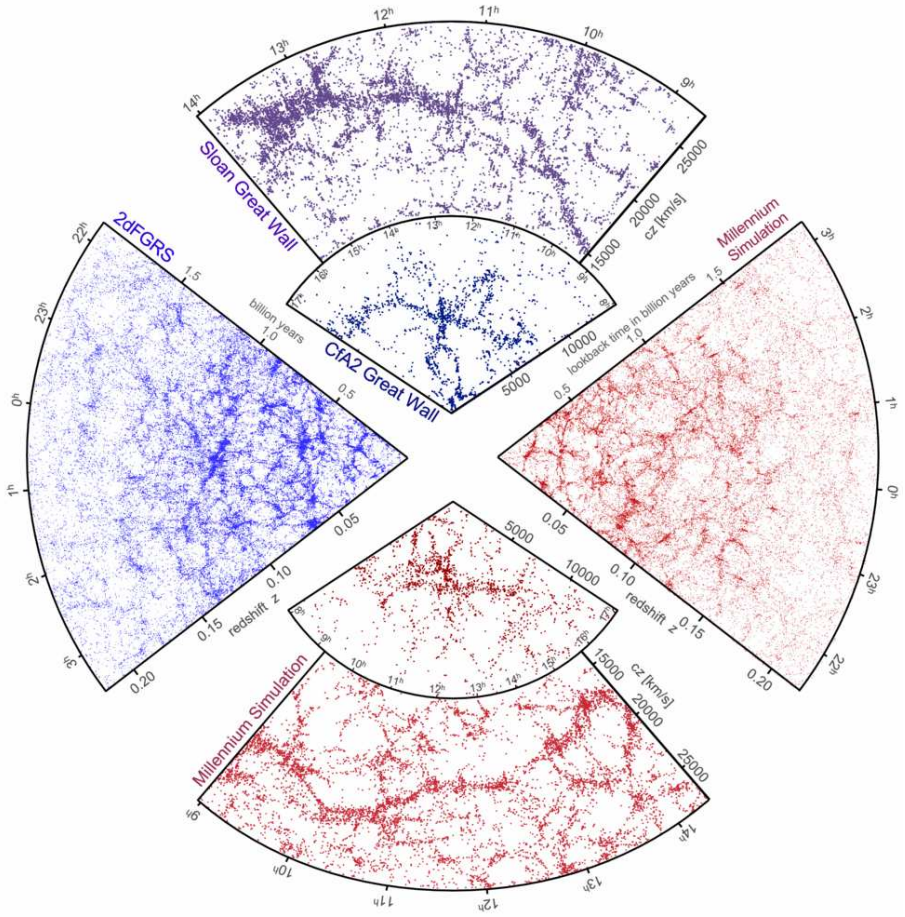

Figure 5.1: **The galaxy distribution obtained from spectroscopic redshift surveys and from mock catalogues constructed from cosmological simulations.** *The small slice at the top shows the CfA2 "Great Wall" [252], with the Coma cluster at the centre. Drawn to the same scale is a small section of the SDSS, in which an even larger "Sloan Great Wall" has been identified [253]. This is one of the largest observed structures in the Universe, containing over 10,000 galaxies and stretching over more than 1.37 billion light years. The wedge on the left shows one-half of the 2dFGRS, which determined distances to more than 220,000 galaxies in the southern sky out to a depth of 2 billion light years. The SDSS has a similar depth but a larger solid angle and currently includes over 650,000 observed redshifts in the northern sky. At the bottom and on the right, mock galaxy surveys constructed using semi-analytic techniques to simulate the formation and evolution of galaxies within the evolving dark matter distribution of the Millennium simulation [236] are shown, selected with matching survey geometries and magnitude limits. From Ref. [237]*

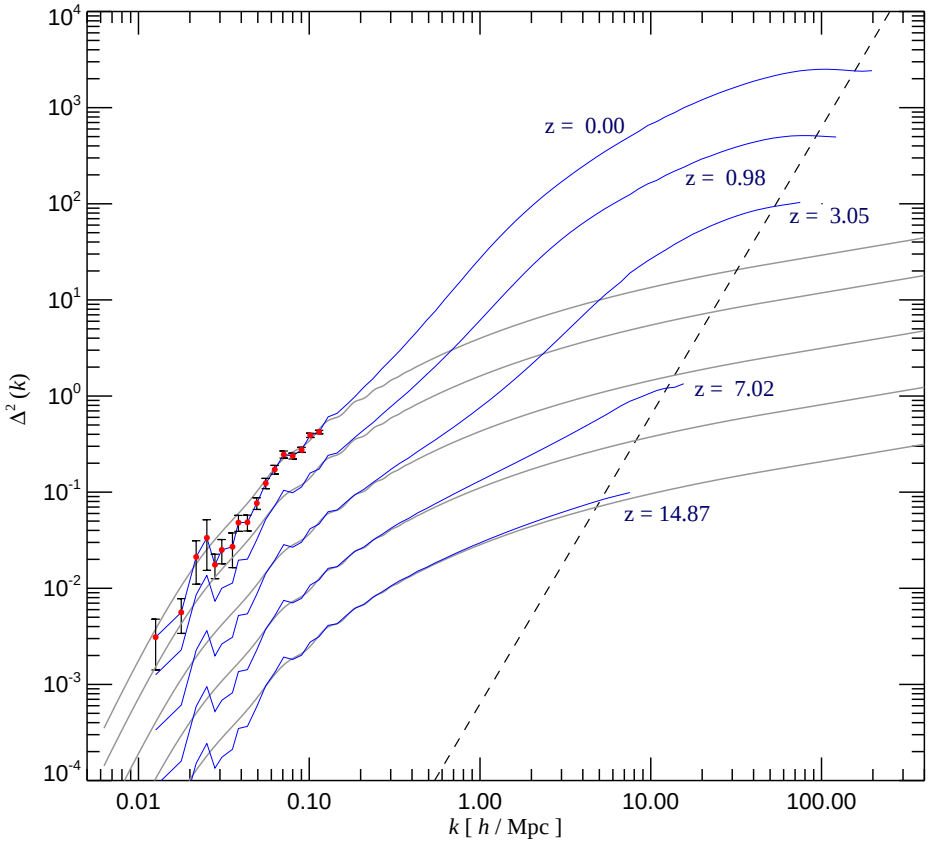

Figure 5.2: The power spectrum of the dark matter distribution in the Millennium Simulation at various epochs (blue lines). *The gray lines show the power spectrum predicted for linear growth, while the dashed line denotes the shot-noise limit expected if the simulation particles are a Poisson sampling from a smooth underlying density field. In practice, the sampling is significantly sub-Poisson at early times and in low density regions, but approaches the Poisson limit in nonlinear structures. Shot-noise subtraction allows us to probe the spectrum slightly beyond the Poisson limit. Fluctuations around the linear input spectrum on the largest scales are due to the small number of modes sampled at these wavelengths and the Rayleigh distribution of individual mode amplitudes assumed in setting up the initial conditions. To indicate the bin sizes and expected sample variance on these large scales, we have included symbols and error bars in the $z = 0$ estimates. On smaller scales, the statistical error bars are negligibly small. From Ref. [236].*

tribution. This non-linear evolution not only alters the lensed temperature power spectrum by about $\sim 0.2\%$ at $\ell \sim 2000$ and $\sim 1\%$ or more on smaller scales, but, much more notably, introduces $\sim 10\%$ corrections to the B–mode polarization power on *all the scales*

[191, 175].

5.2 All-sky simulated lensed maps: the state of the art

The increasing sensitivity and resolution of the forthcoming CMB experiments demands a detailed mapping in total intensity and polarization of the last-scattering photons. We know that CMB is characterized by primary and secondary anisotropies in the intensity and polarization (Chapter 3), and, among the main phenomena which can generate secondary effects, the CMB weak-lensing is noteworthy and is caused by the distortion that the gradients of the gravitational potential from matter structures induce on the geodesics of the LS photons (Chapter 4). This is one of the most relevant effects which are detectable by the forthcoming probes and has high relevance for studying the structure formation and the cosmic acceleration.

On the experimental side, CMB observations are already at the level of precision such that the lensing effect on the temperature and polarization power spectra will become crucial for an accurate analysis. This will certainly be the case once data from the future Planck satellite becomes available. CMB experiments, targeting polarization[3], and in particular the B-modes from gravitational waves, require a precise knowledge of the lensing effects in order to separate them from the cosmological signal. For all such instruments, lensing reconstruction and delensing will become essential. [175].

On the theoretical side instead, since the lensing signal has the same frequency spectrum as the unlensed CMB (and hence cannot easily be distinguished), the understanding and modeling of this effect is essential for the correct interpretation of the CMB data. The delensing methods for subtracting out the B-mode lensing signal have so far only been developed in idealized cases: flat sky without boundaries, simple noise and beam properties, all-sky without non-linear structures, etc. Improved methods may be required to obtain accurate parameter constraints from future high-resolution measurements of the E and B polarization [175].

For all these reasons, simulated all-sky lensing maps from N-body simulations are gaining increasing importance, since they should in principle allow to recover a much more accurate and realistic signal than the simple lensing potential spectrum obtained in a semi-analytical way, as shown in Chapter 4. On the other hand, if the lensing potential can be reconstructed accurately, the sky can be delensed simply by mapping

[3] http://lambda.gsfc.nasa.gov

points back according to the deflection angle. This would be useful for CMB analyses, as the unlensed sky has much simpler statistics than the lensed sky. For example, the smoothing effect of lensing also potentially hides any small scale structure in the CMB power spectrum [254], and delensing would be very useful to uncover this information. Lensing potential reconstruction could also provide good non-degenerate constraints do distinguish the scale-dependent effects of massive neutrinos and dark–energy evolution [255].

In this Chapter we show the results from our first step (the construction of all-sky lensing–potential and deflection–angle maps) in the realization of simulated all-sky lensed CMB maps from the dark-matter distribution of the Millennium Simulation. This work, made in collaboration with my supervisors and Volker Springel, Matthias Bartelmann and Simon White, allows a significant leap forward in the knowledge of the weak-lensing distortion of the CMB temperature and polarization maps, since it is computed on the basis of well resolved and fully non-linear dark matter structures which are supposed to reproduce the ΛCDM model accurately. In this way, a more realistic small-scale lensing analyses can be performed and the whole non-Gaussian statistics injected by lensing onto the background CMB anisotropies, both in intensity and polarization, can be characterized properly, significantly extending the existing approach which is only based on the power spectrum and the Gaussianity assumption of the lensing potential field.

Indeed, all-sky lensed CMB maps have already been carried out [191] using the first-Born approximation and under the assumption that "both the lensing potential and unlensed CMB fields are Gaussian and statistically isotropic" [175].
In these previous works, however, the lensing potential map is constructed via a semi–analytic approach, *i.e.* the non-linear matter power spectrum, provided by a semi–analytical formula at different redshifts [257][4], is interpolated and integrated along the line–of–sight to produce directly the angular power spectrum of the lensing potential Ψ. Given the Gaussian distribution of the spherical harmonic coefficients Ψ_{lm} (where $\Psi(\hat{\mathbf{n}}) = \sum_{lm} \Psi_{lm} Y_{lm}(\hat{\mathbf{n}})$), its variance $C_l^{\Psi\Psi}$ is the used to carry out a synthetic sky map of Ψ, neglecting completely all the information which arise from the *non-Gaussian* features

[4] As discussed in Sec. 4.3, on small scales the lensing evolution is not linear and Gaussian anymore, due to the non-linear structure evolution. The main effect is to change the Φ power spectrum on small scales, which can be estimated from numerical simulations. For simple models, fits to numerical simulation like the HALOFIT code of Ref. [257] can be used to compute an approximate non-linear, equal-time power spectrum, given an accurate numerical linear power spectrum at some redshift.

of the non-linear matter distribution, as, *e.g.*, the output of a N-body simulation results to be.
Given the two maps, one of the gradient of the lensing potential and one of the background CMB, a lensed CMB map can then be made by remapping points on the CMB map according to the deflection vector $\boldsymbol{\alpha} = \nabla_{\hat{\mathbf{n}}}\Psi$ obtained from the lensing potential map [258, 184, 259] (see Sec. 4.2).
In the cited works [191], the deflection vector field is constructed exploiting its power spectrum $\ell(\ell+1)C_l^{\Psi\Psi}$ and the vector spherical harmonic analysis; spherical trigonometry is then used to calculate the pixel remapping from the geodesic in the direction of the deflection vector.

This strategy of extrapolating the lensing–potential and deflection–angle maps from their power spectra could be a good approximation on large scales, but on small scales a modeling of the effects of a realistic non-linear evolution of matter structures is needed, and requires doing detailed numerical simulations of the matter density field.
For what concerns the line–of–sight integration instead, even if the photon path could be computed by ray tracing with more accuracy, in most of the cases the first Born–approximation along the *undeflected* photon path can be used to good accuracy to obtain results which include the non-linear physics. Even on these small scales, in fact, this approximation still holds in the small-angle scattering limit, *i.e.* for typical deflections being of the order of arcminutes or less [260, 261]. For example, single clusters (for which the deflection occurs only in a very thin section of the photon path, over which the deflected and undeflected paths are the same) typically give deflection angles of 1 arcminute, while smaller structures, such as galaxies, give arcsecond deflections. Only a minuscule fraction of lines of sight come close to black holes or other dense bodies that violate the small-angle assumption. Finally, it can be shown that the Born–approximation apply equally well to 'strong' lensing cases, provided that deflection angles are small[5] [175]. Finally, as already discussed in Sec. 4.2, second order corrections to the first-Born approximation (for instance a non-vanishing curl component ω) are expected to be much less than the non-linear structure evolution effects on small scales. For this reasons the first Born–approximation looks accurate enough for carryng out all-sky weak-lensed CMB maps from N-body simulation.

[5]This can happen even for tiny deflection angles if the source is small. For example massive clusters have a CMB Einstein ring at a radius of only ~ 1 arcminute from the centre, corresponding to the radius at which deflected rays meet at a point on the last scattering surface.

5.3 Map-making procedure with the Millennium Run

Our approach is completely different from the previous ones. Our computation, in fact, performs a Born–approximation ray–tracing of the CMB photons in the 3-D field of the peculiar gravitational potential stored by the Millennium Simulation at each of the time outputs (see Sec. 5.1).

The method, followed to carry out our mock maps, stacks up around the observer (fixed at $z = 0$) the 3-D peculiar–gravitational–potential boxes of the simulation. In this way we should produce a fair statistical sample for an eventual CMB–lensing analysis. The extension of the all-sky map corresponds to a redshift of $z_* = 11$ (beyond this redshifts the contribution from matter structures to the lensing potential integral is completely negligible), *i.e.* to a comoving distance of approximately $r_* = 7236$ Mpc/h; in other words, we stack the simulation volume roughly 14.5 times along both the positive and negative directions of the three Cartesian axes x, y, z with origin on the observer.

The necessity of avoiding the repetition of the same structures along the line–of–sight requires the randomization of the boxes used to build up the lensing all-sky maps. Moreover, in order to avoid unphysical ripples in the simulated lensing–potential and deflection–angle fields, we need everywhere a continuous force transverse to the line–of–sight, so we divide all the volume up to $z_* = 11$ in spherical shells each of thickness 500 Mpc/h comoving (obviously the innermost shell is actually a sphere 250 Mpc/h by comoving radius, centered at the observer).
All the simulation boxes falling into the same shell undergo the same randomization process, *i.e.* they are all translated and rotated with the same random vectors generating the random coordinate transformations, the randomization seeds changing instead from shell to shell. This eliminates any preferred direction in the simulated all-sky maps. With this method we fill in, up to $z_* = 11$, the 3-D space around the observer with the gravitational potential field generated by the Millennium–Simulation matter distribution and, at the same time, by exploiting the appropriately randomized snapshots along the line–of–sight integral, we keep into account also the temporal evolution of the Millennium dark–matter structures. Fig. 5.3 represents a schematic picture of the developed staking–randomization process.

Furthermore, since the gravitational–potential box is a Cartesian grid with resolution ~ 0.195 Mpc$/h$, we apply a spatial three-linear interpolation method to calculate the correct value of the gravitational potential at each step of the line–of–sight pointing in the $\hat{\mathbf{n}}$-direction and crossing the simulation box.

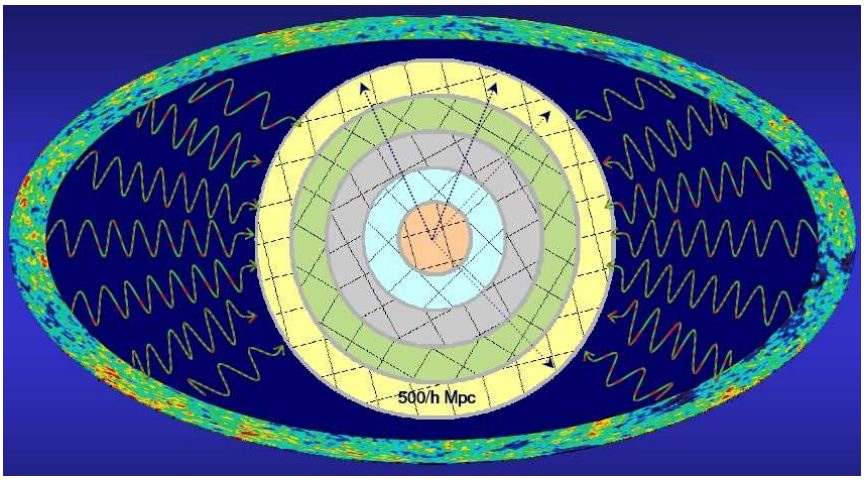

Figure 5.3: *In this picture the adopted staking–randomization process is shown. CMB photons, the electromagnetic radiation coming from the LS surface, pass through the dark-matter distribution of the Universe simulated by stacking the gravitational potential boxes of the Millennium simulation,* 500 *Mpc comoving by side. Each of the boxes (squares), which fall in the same shell (circles), are randomized with the same way coordinate transformation (rotation+translation), which, in turn, differs from shell to shell.*

Moreover, since the sampling of the gravitational potential in the direction transverse to the line–of–sight varies greatly with the distance from the observer, in order to extract the maximum information, even on the smallest scales of the potential field (which are of primary importance mainly for the lensed B-mode signal), we integrate up directly the deflection angle vector along each light–ray. For this purpose, around each integration point, we implement a fourth-order differentiation scheme to compute the local 3-D grid of the transverse gradient of the gravitational potential and, by means of a three-linear interpolation, we calculate its value along the line–of–sight.

In this way, adopting a trapezoidal formula, we compute, in comoving coordinates and flat geometry, the lensing–potential integral

$$\Psi(\hat{\mathbf{n}}) \equiv -2 \int_0^{r_*} dr \frac{r_* - r}{r_* r} \, \Phi(r\hat{\mathbf{n}}; \eta_0 - r) \,, \tag{5.4}$$

and the corresponding deflection–angle integral

$$\boldsymbol{\alpha}(\hat{\mathbf{n}}) \equiv -2 \int_0^{r_*} dr \frac{r_* - r}{r_* r} \, \nabla_{\hat{\mathbf{n}}} \Phi(r\hat{\mathbf{n}}; \eta_0 - r) \,, \tag{5.5}$$

where Φ is the solution of Eq. (5.3) divided by the corresponding scale factor $a(\eta_0 - r)$, the integration path is the undeflected one, and the directions $\hat{\mathbf{n}} \equiv (\vartheta, \varphi)$ follow the HEALPix all-sky pixelization [262].

5.4 The simulated lensing potential and deflection angle

In this Section we show our first results obtained with the Millennium Simulation (MS).

The maps shown in Figs. (5.4)-(5.6), corresponding to a resolution of $3.44'$ [262], represent the 2-D fields on the sky of the lensing–potential, the deflection–angle ϑ/φ-components, and its module $|\boldsymbol{\alpha}|$, respectively, obtained with the previously described procedure.

The mean value of $|\boldsymbol{\alpha}|$ is $1.5'$, while its standard deviation is $0.8'$, about a factor 2 lower than the theoretically expected value of $\sim 1.5'$. The current interpretation is that this is due to the lack of matter power on scales larger than 500 Mpc/h comoving in the MS, since it is well known that a relevant contribution to lensing comes from the linear scales, as we address in more detail in the following. Several interesting features should be noted in these maps.

The distribution of the lensing potential appears to be dominated by large scale structure, which are probably the projection of the large scale potential waves projected onto the observer position in our line of sight integration. This is likely to be related also to the underlying ΛCDM model, where the large scale potential dynamics is enhanced due to the onset of cosmic acceleration. On the other hand, the lensing power cannot be directly inferred by this map, as for the lensing deflection the gradient of the latter is what really matters, as we see in the following.

The maps showing the lensing deflection angles do have interesting features as well. First of all, the signal in the two components of the deflection angle appears to possess to distinct regimes. A diffuse, sort of background distribution caused probably by the lines of sight where no dominant structure is encountered, as well as sharp features, extending over several degrees, caused probably by dominating CDM filaments determining the largest contribution to the deflection in the line of sight integration itself. The same features are evident in the modulus of the lensing potential, where in particular the effect caused by CDM filaments is the most predominant feature in the observed pattern.

It would be premature here to characterize the statistical distribution of the observed structure. We expect a strongly non-Gaussian bias, probably dominating on the angular scales corresponding to the filaments or less, imprinting the corresponding distortion to the CMB anisotropies, which however needs to be investigated in forthcoming and dedicated works.

After the map-making process, by means of the routine ANAFAST of the HEALPix

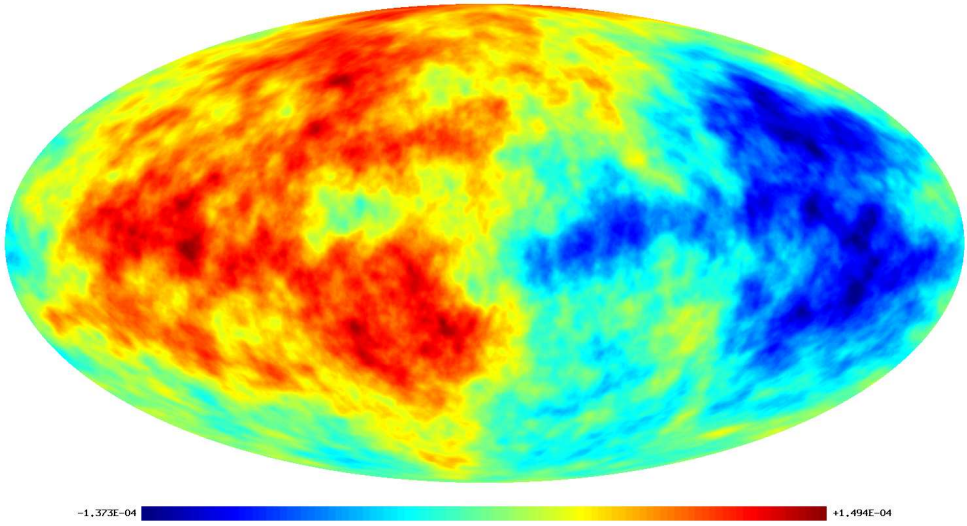

Figure 5.4: *The simulated all-sky map of the lensing potential computed with the map-making procedure described in the text.*

package, we have calculated the lensing–potential and deflection–angle power spectra independently, *i.e.* without exploiting the relation between the two quantities, which holds in the spherical harmonic domain.
We have compared the simulated lensing–potential $C_l^{\Psi\Psi}$, with the corresponding power spectrum obtained as output from the CAMB code[6], fixed with the same MS cosmological parameters and turned on with the HALOFIT non-linear matter power spectrum.

The top panel of Fig. 5.7 shows this comparison. The difference of $\sim$ 1 order of magnitude on low multipoles ℓ is evident and due to the lack of power on scales larger than the simulation box. This difference decreases with ℓ, and at very high multipoles, $\ell \lesssim 2000$, it starts to possess an opposite behavior, due to the MS matter power on small scales, which results to be greater than the corresponding CAMB output. Our current interpretation is that this rise at smaller scales is a new feature corresponding to the better mapping of the non-linear power by the MS, with respect to the ordinary semi-analytic approaches. We will further investigate this effect on small scales by increasing the resolution of the map-making procedure.

In the same way, we have computed the power spectrum $C_l^{\alpha\alpha}$ of the deflection–angle module obtained with our map-making procedure.
In order to compare this result with the CAMB expectations, we have carried out a syn-

[6] http://camb.info

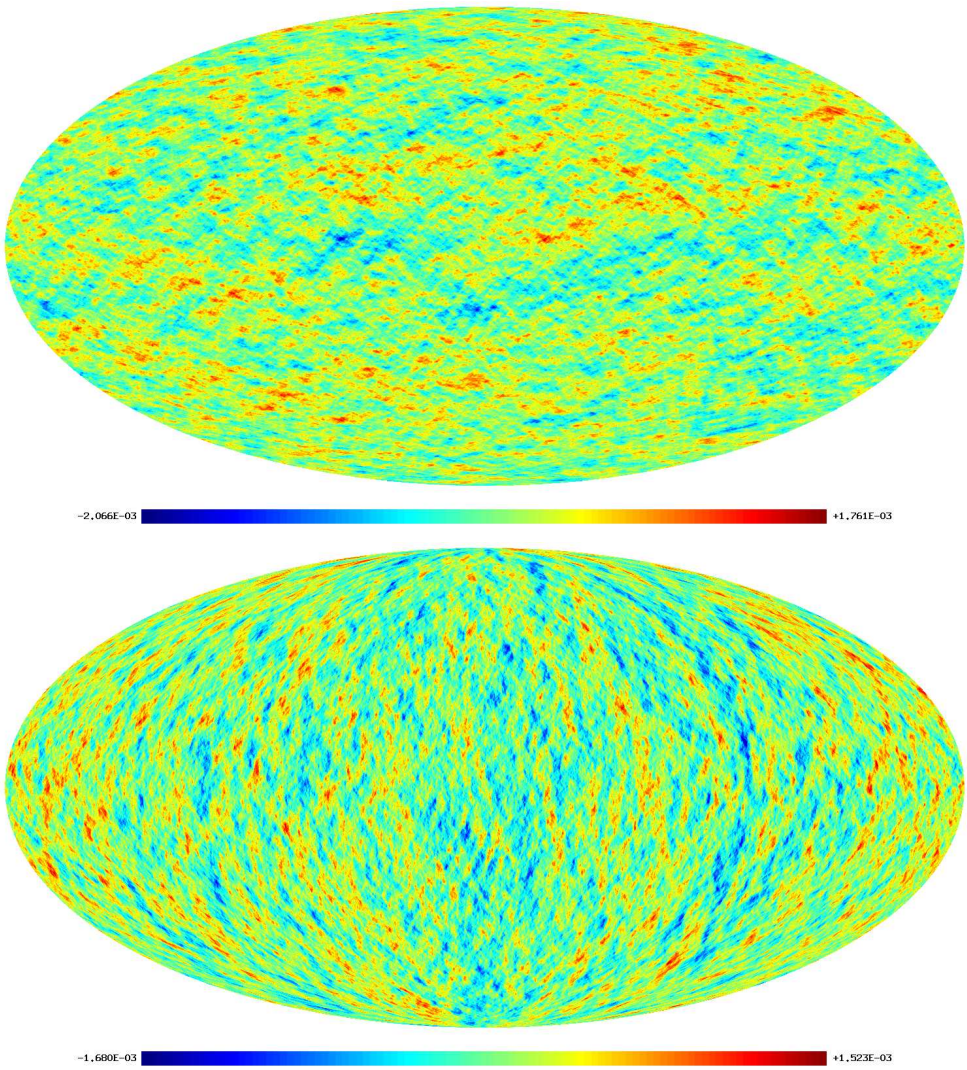

Figure 5.5: *Top: simulated all-sky map of the deflection angle component along the ϑ direction, in radiant units. Bottom: simulated all-sky map of the deflection angle component along the φ direction in radiant units.*

thetic map of the deflection angle module, using the CAMB power, $C_l^{\Psi\Psi}$, as input to the SYNFAST routine of the HEALPix package. This map is shown in the lower panel of Fig. 5.6; its mean value and rms are $2.4'$ and $1.27'$, respectively. The lack of large scale power of the MS result, shown in the upper panel of the same Figure, with respect to the CAMB simulation is evident. On the other hand, the synthetic map possesses a purely Gaussian distribution of the deflection angle, while the MS comes from simulated CDM structures. Once again, the morphological differences, characterizing the deviation from Gaussianity in the MS result, will be studied in dedicated works. We have then com-

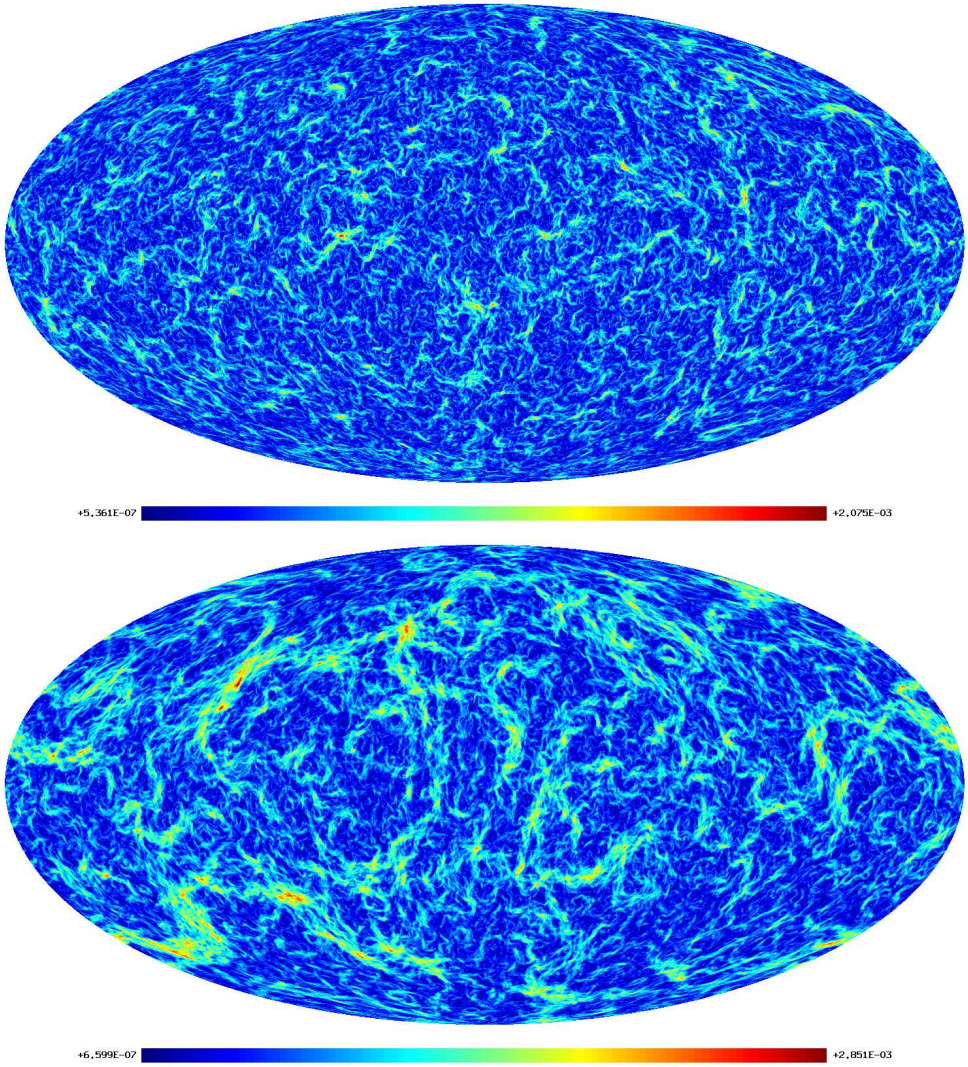

Figure 5.6: *Top: Simulated all-sky map of the deflection-angle module 2D-field (radiants) obtained with the map-making procedure described in the text. Bottom: Synthetic map of the deflection angle module 2D-field (radiants) obtained as the angular gradient of the synthetic map of the CAMB non-linear lensing potential power spectrum.*

puted, with the same routine operating in the harmonic domain, the angular derivatives, with respect to the directions ϑ and φ, of the obtained lensing–potential synthetic map. The power spectrum of the module of the resulting deflection–angle vector, computed with ANAFAST as well, is shown in the lower panel of Fig. 5.7, together with our findings.

On low ℓ the same gap in power as for the lensing potential is clearly visible. As already mentioned, the current interpretation is that the lack of power of MS with respect

to the semi-analytically calculated power spectrum is responsible for the lower standard deviation of the MS deflection angle with respect to the expectation. On larger ℓ, instead, we may observe an increased difference with respect to the lensing–potential case. This is due to the computation of the CAMB deflection angle as derivative of the lensing potential in the harmonic domain: as previously introduced, from a numerical point of view, the integral and derivative operators do not commute in Eq. (5.5), even if on an analytical side they do. From Fig. 5.7 the information gain on the smallest scales due to our approach is evident, as a consequence of the more accurate mapping of the non-linear power in the our simulation.

In the very near future, we will exploit the deflection–angle map to make lensed T-, E- and B-mode maps, according to the remapping procedure described in Sec. 4.3.

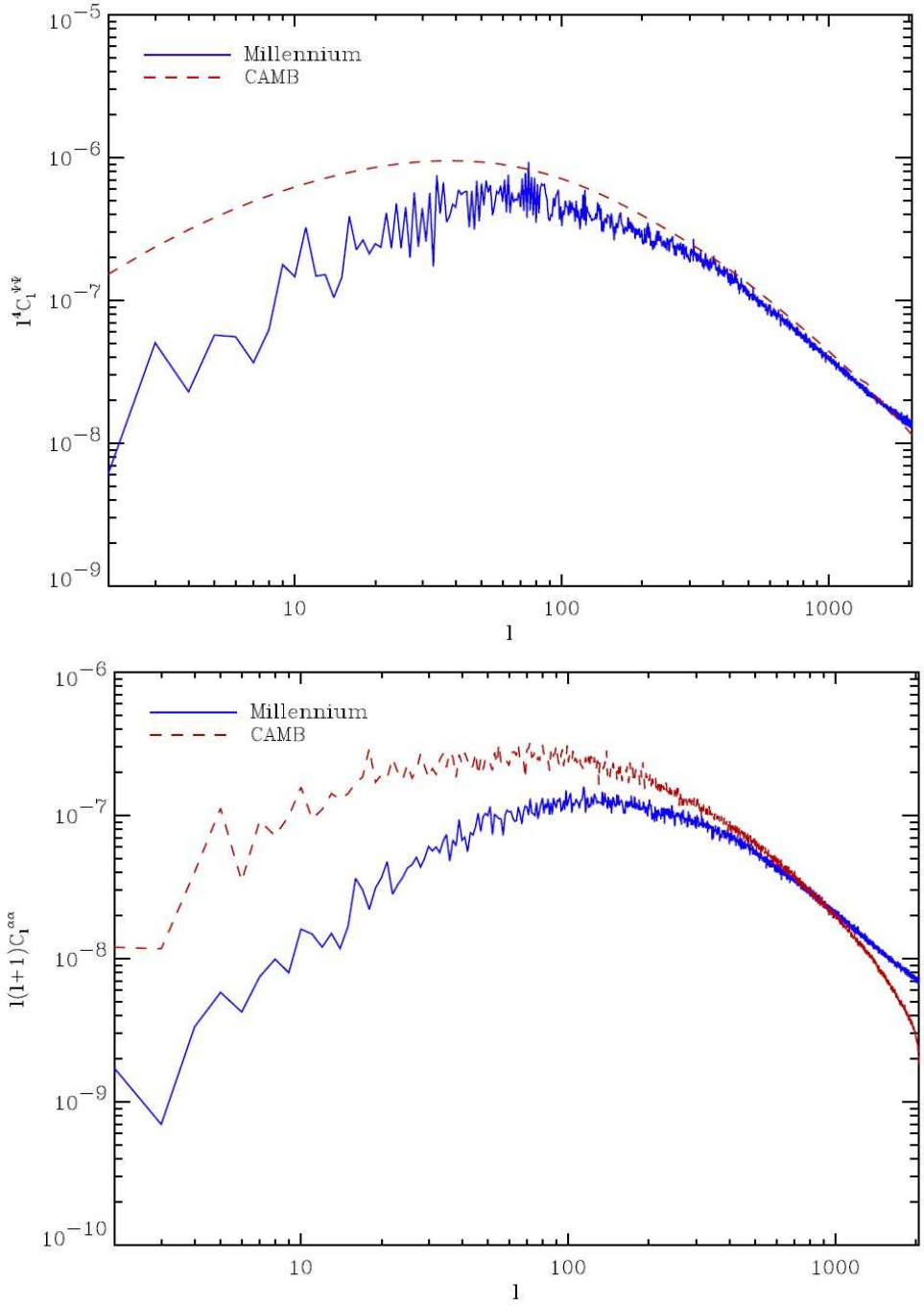

Figure 5.7: *Top: the power spectrum of the lensing potential mapped in Fig. 5.4, compared with the power spectrum of the lensing potential obtained with the CAMB code, including the semi-analytic non-linear evolution computed via the HALOFIT routine. Bottom: the power spectrum (square radiants) of the deflection angle module mapped in the upper panel of Fig. 5.6, compared with the power spectrum of the deflection angle module mapped in the lower panel of the same Figure.*

Conclusions and look at the future

In this thesis I presented the work done during my PhD. In the framework of linear and non-linear structure formation processes in cosmology, I focused on processes which are of interest on their own for our understanding of the recent cosmological evolution, as well as in relation to the forthcoming probes of CMB anisotropies. Among these processes, I considered the GWs emitted by non-linear forming cosmological structures, which might compete against the imprint of cosmological GWs in the curl mode of CMB polarization. Moreover, I started a systematic study of the weak gravitational lensing effect from large cosmological structures using the N-body simulations instead of semi-analytic approaches. The latter study is relevant in a number of contexts, i.e. the comprehension of the structure formation itself, the investigation of the onset of cosmic acceleration, as well as the measurement of the B (curl) mode in the CMB polarization from cosmological GWs, which need to be distinguished from the one induced by lensing. This work is in collaboration with my supervisors as well as Prof. Matthias Bartelmann from the Institute of Theoretical Astrophysics in Heidelberg, Dr. Volker Springel and Prof. Simon White from the Max Planck Institute in Garching, Germany.

Concerning the first issue, I have developed a mathematical formalism to describe scalar, vector and tensor metric perturbations generated by the strongly non-linear evolution of matter structures treated my means of a pressureless fluid corresponding to forming CDM structures.

More specifically, I have shown that, in the case of vector and tensor metric modes, their sources obey the Newtonian dynamics on all the cosmologically relevant scales. These

sources are intended to be typical CDM haloes obeying the Newtonian continuity, Euler and Poisson equations during all the stage of their evolution, from the linear to the highly non-linear level.
Moreover, the amount of the stochastic GW background, produced by these structures, has been evaluated. To this purpose, the CDM haloes have been schematized as collapsing homogeneous ellipsoids, since the experimental evidence, together with the numerical N-body simulations, seem to infer that CDM haloes are characterized by a triaxial structure. Indeed, it is their anisotropic form, together with their peculiar velocities, which allows this objects to be good candidates for the generation of gravitational waves of non-primordial origin.
Bounded to be a cosmological process, the halo-induced GW background possesses a very low frequency, of the order of $\approx 10^{-18}$ Hz, due to the cosmological time-scale of the source evolution, and by an energy density $h^2\Omega_{\rm GW}(\nu) \approx 10^{-20}$, comparable to the energy density associated with the stochastic background induced by primordial GWs on the same frequency range, if the energy scale of inflation is $V^{1/4} \approx 1 - 2 \times 10^{15}$GeV. This last point is very interesting, since, at very low frequencies, the secondary signal could be in competition with a primordial one, as the future CMB observations will clarify.

The weak lensing of background light from forming cosmological structures is one of the most promising cosmological probes. In fact, not only it allows to investigate and understand the process of cosmological structure formation and the CDM properties, but it gains even more attention due to the discovery of cosmic acceleration, which may be investigated optimally by lensing, as the two processes overlap in time. Moreover, exploiting one of the basic geometric lensing properties saying that the lensing cross section peaks quite sharply half way between source and observer, the structure formation may be probed via a tomography, dividing in redshift shells the background light. This represents a unique feature which might be exploited to perform a tomography of the structure formation process and the onset of cosmic acceleration. In addition, the lensing has a number of effect on the CMB. As we discussed extensively in this thesis, CMB anisotropies consist in T, E and B modes describing anisotropies in the total intensity, gradient and curl modes of the linear polarization. The lensing correlate different scales, causing a smearing of the acoustic features impressed at last scattering, and causes a leakage on small angular scales, few arcminutes or less, where the primordial power would die otherwise because of diffusion processes at last scattering. Moreover,

it causes an effective leakage of E modes into B, peaking at the characteristic scale of a few arcminutes, representing the main known cosmological competitor of the signal from primordial gravitational waves. So far the weak lensing on CMB has been evaluated semi-analytically, exploiting the two point correlation function. Little is known on the statistics of this process beyond that order, and consequently, on the non-Gaussian distortion induced on the CMB anisotropies.
For all these reasons, we constructed a machinery capable of calculating the lensing deflection angle starting from the Millennium Run N-body simulation, which we are preparing to exploit for lensing the CMB. We faced and solved the relative computational issues as well as the map-making consisting in the stacking of the MR box in order to reproduce a pattern of structures which is large enough to simulate the wanted deflection angle. As expected, the power spectrum of the lensing potential matches with good accuracy the existing semi-analytic expectations on the scales where the MR reproduces faithfully a portion of the Universe; on larger angular scales, a power decrease is observed, due to the replication of the MR structures in the stacking processes. On the other hand an excess of power in the map obtained from the MR is observed, as a result of a more detailed description on the small scale non-linear power in the N-body with respect to the semi-analytic approach. These and other more CMB oriented studies are being carried out and published in forthcoming papers.

Indeed, in the near future we intend to re-map the primordial CMB field by mean of the simulated all-sky maps of the deflection angle and make a statistical analysis of the obtained signal. Moreover we will look at the cross-correlation of the lensed CMB maps with all-sky maps of the ISW/Rees-Sciama effects and of foreground galaxies from the Millennium Simulation.

Future developments of my research could also include constrained simulations and reference sky for future CMB probes.
In fact, the construction of lensed CMB maps can be improved via the use of constrained N-body simulations, *i.e.* simulations which have initial conditions built up by means of constrained realizations of random Gaussian fields, and which, therefore, reproduce density and velocity fields in agreement both with the observed structures and the assumed theoretical model.

This will produce not only lensing maps that mimic direct observations, but it might make also possible to subtract the lensing signal from the forthcoming CMB total intensity and polarization maps. This will facilitate the analysis of the primordial non-

Gaussianity as well of the B modes from cosmological gravitational waves.

Most importantly, on the dark energy side, in view of the forthcoming large area weak-lensing surveys, a future step of my work would be to apply our developed numerical machinery to N-body simulations in dark energy cosmologies. This would result to be extremely useful to assess the lensing relevance in constraining different dark energy models.

Bibliography

[1] A. Einstein (1917), English translation in **The Principle of Relativity**, H. A. Lorentz, A. Einstein, H. Minkowski, and H. Weyl (Dover, New York, 1952).

[2] E. W. Kolb and M. S. Turner, *The Early Universe*, Addison-Wesley (Redwood City, 1990).

[3] A. R. Liddle and D. H. Lyth, *Cosmological Inflation and Large-Scale Structure*, (Cambridge University Press, 2000).

[4] O. Lahav and A. Liddle, Journal of Physics **G33**, 1 (2006).

[5] G. Hinshaw *et al.*, Astrophys. J. Suppl. **170**, 288 (2007).

[6] D. N. Spergel *et al.*, Astrophys. J. Supp. **170**, 377 (2007).

[7] B. D. Field and S. Sarkar, J. Phys. G **33**, 220 (2006).

[8] R. H. Cyburt, Phys. Rev. D **70**, 023505 (2004).

[9] G. Steigman, Int. J. Mod. Phys. E **15**, 1 (2006).

[10] J. C. Mather *et al.*, Astrophys. J. **512**, 511 (1999).

[11] P. Astier et al., Astron. Astrophys. **447**, 31 (2006).

[12] J. R. Mould et al., Astrophys. J. **529**, 786 (2000).

[13] A. G. Riess *et al.*, Astron. J. **116**, 1009 (1998).

[14] P. Garnavich *et al.*, Astrophys. J. **509**, 74 (1998).

[15] S. Perlmutter *et al.*, Astrophys. J. **517**, 565 (1999).

[16] R. A. Knop *et al.*, Astrophys. J. **598**,102 (2003).

[17] A. Refregier *et al.*, Proceedings of the SPIE **6265**, 62651Y (2006).

[18] D. N. Spergel *et al.*, Atrophys. J. Supp. **148**, 175 (2003).

[19] S. W. Allen *et al.*, Mont. Not. Roy. Atr. Soc. **342**, 287 (2003).

[20] B. Chaboyer and L. M. Krauss, Science **299**, 65 (2003).

[21] R. Cayrel *et al.*, Nature **409**, 691 (2001).

[22] J. K. Adekman-McCarthy *et al.*, Astrophys. J. Supp. **162**, 38 (2006).

[23] M. Tegmark *et al.*, Phys. Rev. D **74**, 123507 (2006).

[24] C. L. Bennett *et al.*, Astrophys. J. Suppl. **148**, 1 (2003).

[25] K. M. Górski *et al.*, Astrophys. J. Suppl. **114**, 1 (1998).

[26] E. Komatsu *et al.*, Astrophys. J. Suppl. **148**, 119 (2003).

[27] J. M. Kovac, *et al.*, Nature **420**, 772 (2002).

[28] L. Page *et al.*, Astrophys. J. Suppl. **170**, 335 (2007).

[29] P. Oxley *et al.*, Proc. SPIE Int. Soc. Opt. Eng. **5543**, 320 (2004).

[30] S. Cole *et al.*, Mon. Not. Roy. Astr. Soc. **362**, 505 (2005).

[31] M. Tegmark *et al.*, Astrophys. J. **606**, 702 (2004).

[32] D. Eisenstein *et al.*, Astrophys. J. **633**, 560 (2005).

[33] M. Oguri *et al.*, arXiv:0708.0825 [astro-ph].

[34] A. F. Heavens, T. D. Kitching and A. N. Taylor, Mon. Not. R. Astron. Soc. **373**, 105 (2006).

[35] D. Munshi *et al.*, [arXiv:astro-ph/0703496]

[36] A. Refregier Annu. Rev. Astron. Astrophys. **41**, 645 (2003).

[37] J. M. Bardeen, Phys. Rev. D **22**, 1882 (1980).

[38] P. J. E. Peebles, *The Large–Scale Structure of the Universe*, Princeton University Press, Princeton (1980).

[39] K. Tomita, Prog. Theor. Phys. **79**, 258 (1988).

[40] K. Tomita, Prog. Theor. Phys. **85**, 1041 (1991).

[41] M. Shibata, H. Asada, Prog. Theor. Phys. **94**, 11 (1995).

[42] S. Matarrese and D. Terranova, Mon. Not. Roy. Astron. Soc. **289**, 100 (1997).

[43] E. Bertschinger, in *Cosmology and Large Scale Structure*, Proceedings of the Les Houches School, edited by R. Shaeffer, J. Silk, M. Spiro, and V. Zinn-Justin (Elsevier, Netherland, 1996).

[44] T. Pyne and S. Carroll, Phys. Rev. D **53**, 2920 (1996).

[45] S. Mollerach and S. Matarrese, Phys. Rev. D **56**, 4494 (1997).

[46] S. Mollerach, D. Harari and S. Matarrese, Phys. Rev. D **69**, 063002 (2004).

[47] N. Bartolo, S. Matarrese and A. Riotto, in Lectures given by S. M. at Les Houches Summer School- Session 86: *Particle Physics and Cosmology: The Fabric of Spacetime*, Les Houches, France, 31 Jul–25 Aug 2006. [arXiv:astro-ph/0703496]

[48] K. Tomita, Prog. Theor. Phys. **37**, 331 (1967)

[49] S. Matarrese, O. Pantano and D. Saez, Phys. Rev. Lett. **72**, 320 (1994).

[50] K. Tomita, Prog. Theor. Phys. **45**, 1747 (1967); **47**, 416 (1972).

[51] S. Matarrese, S. Mollerach and M. Bruni, Phys. Rev. D **58**, 043504 (1998).

[52] C. P. Ma, E. Bertschinger, Astrophys. J. **455**, 7 (1995).

[53] C. Carbone and S. Matarrese, Phys. Rev. D **71**, 043508-1 (2005).

[54] V. Acquaviva, N. Bartolo, S. Matarrese and A. Riotto, Nucl. Phys. B **667**, 119 (2003).

[55] H. Noh and J. c. Hwang, Phys. Rev. D **69**, 104011 (2004).

[56] C. Carbone, C. Baccigalupi and S. Matarrese, Phys. Rev. D **73**, 063503 (2006).

[57] S. Chandrasekhar, Astrophys. J. **142**, 1488 (1965).

[58] S. Chandrasekhar, Astrophys. J. **158**, 45 (1969).

[59] S. Chandrasekhar, Astrophys. J. **160**, 153 (1970).

[60] C. W. Misner, K. S. Thorne and j. A. Wheeler, *Gravitation*, W. H. Freeman and Company, San Francisco (1973).

[61] V. F. Mukhanov, H. A. Feldman and R. H. Brandenberger, Phys. Rept. **215**, 203 (1992).

[62] H. Kodama, M. Sasaki, Prog. Theor. Phys. **78**, 1 (1984); **47**, 416 (1972).

[63] F. C. Mena, R. Tavakol and M. Bruni, Int. J. Mod. Phys. A **17**, 4239 (2002).

[64] S. Weinberg, *Gravitation and cosmology*, Wiley, New York, (1973).

[65] L. D. Landau and E. M. Lifshitz, *The classical theory of fields*, Pergamon Press, New York, (1975)

[66] V. Quilis, J. M. Ibanez and D. Saez, Astrophys. J. **501**, 21 (1998).

[67] V. Quilis, J. M. Ibanez and D. Saez, Astron. Astrophys. **353**, 435 (2000).

[68] S. Matarrese and S. Mollerach, "The stochastic gravitational-wave background produced by non-linear cosmological perturbations", in Proc. "Some topics on General Relativity and Gravitational Radiation", p.87, edited by J. A. Miralles, J. A. Morales, D. Saez, Editions Frontires, Paris, 1997, [arXiv:astro-ph/9705168].

[69] M. Maggiore, Phys. Rep. **331**, 283 (2000).

[70] T. L. Smith, E. Pierpaoli and M. Kamionkowski, Phys. Rev. Lett. **97**, 021301 (2006).

[71] `http://www.ligo.caltech.edu`

[72] T. L. Smith, M. Kamionkowski and A. Cooray, Phys. Rev. D **73**, 023504 (2006)

[73] V. Ferrari, S. Matarrese, R. Schneider, Mon. Not. Roy. Astron. Soc. **303**, 258 (1999).

[74] K. A. Postnov, in Proc. "Particles and Cosmology", 9th International Baksan School, 1997, [arXiv:astro-ph/9706053].

[75] D. I. Kosenko and K. A. Postnov, Astron. Astrophys. **336**, 786 (1998).

[76] R. Schneider, A. Ferrara, V. Ferrari, S. Matarrese, Mon. Not. Roy. Astron. Soc. **317**, 385 (2000).

[77] R. Schneider, V. Ferrari, S. Matarrese, S. F. Portegies Zwart, Mon. Not. Roy. Astron. Soc. **324**, 797 (2001).

[78] A. J. Farmer and E. S. Phinney, Mon. Not. Roy. Astron. Soc. **346**, 1197 (2003).

[79] L. P. Grishchuk, [arXiv:gr-qc/0305051].

[80] W. Hu, U. Seljak, M. White, M. Zaldarriaga, Phys. Rev. D **57**, 3290 (1998).

[81] M. Kamionkowski and A. Kosowsky, Ann. Rev. Nucl. Part. Sci. **49**, 77 (1999); W. Hu and S. Dodelson, Ann. Rev. Astron. Astrophys. **40**, 171 (2002).

[82] S. Dodelson, *Modern Cosmology* (Academic Press, 2003); A. Liddle and D. H. Lyth, *Cosmological Inflation and Large-Scale Structure* (Cambridge University Press, 2000).

[83] J. Pritchard and M. Kamionkowski, Annals Phys. **318**, 2 (2005).

[84] M. Kamionkowski, A. Kosowsky, A. Stebbins, Phys. Rev. D **55**, 7368 (1997).

[85] M. Zaldarriaga and U. Seljak, Phys. Rev. D **55**, 1830 (1997).

[86] U. Seljak and M. Zaldarriaga, Phys. Rev. Lett. **78**, 2054 (1997).

[87] M. Zaldarriaga and U. Seljak, Phys. Rev. D **58**, 023003 (1998).

[88] U. Seljak and C. M. Hirata, Phys. Rev. D **69**, 043005 (2004).

[89] P. Cabella and M. Kamionkowski, Lectures given at the 2003 Villa Mondragone School of Gravitation and Cosmology: "The Polarization of the Cosmic Microwave Background," Rome, Italy, September 6–11, 2003, [arXiv:astro-ph/0403392].

[90] N. Turok, U. L. Pen, U. Seljak, Phys. Rev. D **58**, 023506 (1998).

[91] M. Tegmark et al., Phys. Rev. D **69**, 103501 (2004).

[92] D. N. Spergel et al., Astrophys. J. Suppl. **148**, 175 (2003).

[93] Y. P. Jing and Y. Suto, Astrophys. J. **529**, L69 (2000).

[94] M. J. West, Astrophys. J. **347**, 610 (1989).

[95] M. Plionis, J. D. Barrow, C. S. Frenk, Mon. Not. Roy. Astron. Soc. **249**, 662 (1991).

[96] J. R. Bond and S. T. Myers, Astrophys. J. Suppl. Series **103**, 1 (1996).

[97] S. Chandrasekhar, *Ellipsoidal Figures Equilibrium*, Yale Univ. Press, New Haven, (1969).

[98] J. Binney and S. Tremaine, *Galactic Dynamics*, Princeton Univ. Press, Princeton, (1987).

[99] S. D. White and J. Silk, Astrophys. J. **231**, 1 (1979).

[100] R. K. Sheth, H. J. Mo, G. Tormen, Mon. Not. Roy. Astron. Soc. **323**, 1 (2001).

[101] R. K. Sheth and G. Tormen, Mon. Not. Roy. Astron. Soc. **329**, 61 (2002).

[102] R. K. Sheth and G. Tormen, Mon. Not. Roy. Astron. Soc. **308**, 119 (1999).

[103] J. R. Bond, S. Cole, G. Efstathiou, N. Kaiser, Astrophys. J. **379**, 440 (1991).

[104] T. Kitayama and Y. Suto, Astrophys. J. **469**, 480 (1996).

[105] J. A. Peacock and S. J. Dodds, Mon. Not. Roy. Astron. Soc. **267**, 1020 (1994).

[106] N. Sugiyiama, Astrophys. J. Suppl. Series **100**, 281 (1995).

[107] S. M. Carroll, W. H. Press, E. L. Turner, Annu. Rev. Astron. Astrophys. **30**, 499 (1992).

[108] G. Kauffmann, M. J. Colberg, A. Diaferio, S. D. M. White, Mon. Not. Roy. Astron. Soc. **303**, 188 (1999).

[109] A. Jenkins, C. S. Frenk, F. R. Pearce, P. A. Thomas, M. J. Colberg, S. D. M. White, H. M. P. Couchman, J. A. Peacock, G. Efstathiou, A. H. Nelson, Astrophys. J. **499**, 20 (1998).

[110] O. Lahav, P. B. Lilje, J. R. Primack, M. Rees, Mon. Not. Roy. Astron. Soc. **251**, 128 (1991).

[111] H. Goldstein, *Classical Mechanics*, Addison-Wesley, Cambridge, Mass., (1956).

[112] R. L. Forward, Phys. Rev. D **17**, 379 (1978).

[113] V. Quilis, J. M. Ibanez and D. Saez, Astrophys. J. **501**, L21 (1998).

[114] V. Quilis, J. M. Ibanez and D. Saez, Astron. Astrophys. **353**, 435 (2000).

[115] S. L. Shapiro and S. A. Teukolsky, *Black Holes, White Dwarfs ans Neutron Stars*, John Wiley, New York, (1983).

[116] G. C. Liu, A. da Silva, N. Aghanim, Astrophys. J. **621**, 15 (2005).

[117] A. A. Penzias and R. W. Wilson, Astrophys. J. **142**, 419 (1965).

[118] A. McKellar, Publ. Dominion Astrophys. Obs. **7**, 251 (1941).

[119] E. A. Ohm, Bell Syst. Tech. J. **40**, 1065-1094 (1961).

[120] G. Gamow, Phys. Rev. **74**, 505 (1948).

[121] R. A. Alpher, Phys. Rev. **74**, 1577 (1948).

[122] R. H. Dicke, P. J. E. Peebles, P. G. Roll, and D. T. Wilkinson, Astrophys. J. **142**, 414 (1965).

[123] G. F. Smoot, et al., Astrophys. J. Lett. **396**, L1 (1992).

[124] A. Dekel, Ann. Rev. Astron. Astrophys. **32**, 371 (1994).

[125] M. Zaldarriaga and U. Seljak, Phys. Rev. D **55**, 1830 (1997).

[126] J. N. Gpldberg *et al.*, J. Math. Phys. **8**, 2155 (1967).

[127] E. Newman and R. Penrose, J. Math. Phys. **7**, 863 (1966).

[128] M. Kamionkowski, A. Kosowsky and A. Stebbins, Phys. Rev. D **55**, 7368 (1997).

[129] W. Hu and M. White, Phys. Rev. D **56**, 596 (1997).

[130] J. R. Bond and G. Efstathiou, Astrophys. J. **285**, L45 (1984).

[131] J. R. Bond & G. Efstathiou, Mon. Not. R. Astron. Soc. **226**, 655 (1987).

[132] M. L. Wilson & J. Silk, Astrophys. J. **243**, 14 (1981).

[133] J. R. Bond & G. Efstathiou, Astrophys. J. **285**, L45 (1984).

[134] C. -P. Ma & E. Bertschinger Astrophys. J. **455**, 7 (1995).

[135] R. Crittenden *et al.*, Phys. Rev. Lett. **69**, 1856 (1993).

[136] M. Zaldarriaga & D. Harari Phys. Rev. D **52**, 3276 (1995).

[137] L. F.Abbott and R. K. Schaefer, Astrophys. J. **308**, 546 (1986).

[138] U. Seljak and M. Zaldarriaga, Astrophys. J. **469**, 437 (1996).

[139] J. Peacock, *Cosmological Physics*, Cambridge UP, (1999).

[140] P. J. E. Peebles and J. T. Yu, Astrophys. J. **162**, 815 (1970).

[141] R. K. Sachs and A. M. Wolfe, Astrophys. J. **147**, 73 (1967) .

[142] J. Peacock, Mon. Not. R. Astron. Soc. **253**, 1P (1991).

[143] J. Silk, Astrophys. J. **151**, 459 (1968).

[144] G. Efstathiou and J. R. Bond, Mon. Not. R. Astron. Soc. **227**, 33P (1987).

[145] M. J. Rees, Astrophys. J. **153**, L1 (1968).

[146] J. R. Bond and G. Efstathiou, Mon. Not. R. Astron. Soc. **226**, 655 (1987).

[147] N. Kaiser, Mon. Not. R. Astron. Soc. **202**, 1169 (1983).

[148] C. Hogan, N. Kaiser, M.J. Rees, Phil. Trans. R. Soc. Lon. Ser. A **307**, 97 (1982).

[149] R. Crittenden, R. Davis, and P. Steinhardt, Astrophys. J. **417**, L13 (1993).

[150] R. G. Crittenden, D. Coulson, and N. G. Turok, Phys. Rev. D **52**, 5402 (1995).

[151] W. Hu, D. Spergel, and M. White, Phys. Rev. D **55**, 3288 (1997).

[152] D. N. Spergel and M. Zaldarriaga, Phys. Rev. Lett. **79**, 2180 (1997).

[153] U. Seljak, Astrophys. J. **482**, 6 (1997).

[154] M. Zaldarriaga, D. N. Spergel, and U. Seljak, Astrophys. J. **488**, 1 (1997).

[155] D. J. Eisenstein, W. Hu, and M. Tegmark, Astrophys. J. Lett. **504**, L57 (1998).

[156] G. Efstathiou and J. R. Bond, Mon. Not. R. Astron. Soc. **304**, 75 (1999).

[157] M. J. Rees & D. W. Sciama, Nature **217**, 511 (1968).

[158] M. Bruscoli *et al.*, Mon. Not. R. Astron. Soc. **318**, 1068 (2000).

[159] A. J. Benson *et al.*, Mon. Not. R. Astron. Soc. **320**, 153 (2001).

[160] N. Y. Gnedin, A. H. Jaffe, Astrophys. J. **551**, 3 (2001).

[161] R. A. Sunyaev & I. B. Zeldovich, Astron. Astrophys. **20**, 189 (1972).

[162] R. A. Sunyaev & I. B. Zel'dovich, Ann. Rev. Astron. & Astrophys. **18**, 537 (1980).

[163] J. P. Ostriker & E. T. Vishniac, E. T. Astrophys. J. Lett. **306**, L51 (1986).

[164] E. Komatsu & T. Kitayama Astrophys. J. **526**, L1 (1999).

[165] G. Holder & J. Carlstrom, in *Microwave Foregrounds*, ed. A. de Oliveira-Costa and M. Tegmark, ASP Conference Series, San Francisco, 199 (1999).

[166] A. Cooray Phys. Rev. D **62**, 103506 (2000).

[167] S. M. Molnar and M. Birkinshaw Astrophys. J. **537**, 542 (2000).

[168] P. Zhang, U.-L. Pen, Astrophys. J. **577**, 555 (2002).

[169] A. C. da Silva *et al.*, Mon. Not. R. Astron. Soc. **317**, 37 (2000).

[170] A. Refregier *et al.*, Phys. Rev. D **61**, 123001 (2000).

[171] U. Seljak, J. Burwell, U.-L. Pen, Phys. Rev. D **63**, 063001 (2001).

[172] V. Springel, M. White, L. Hernquist, Astrophys. J. **549**, 681 (2001).

[173] A. C. da Silva *et al.*, Mon. Not. R. Astron. Soc. **326**, 155 (2001).

[174] O. Zahn *et al.*, Astrophys. J. **630**, 657 (2005).

[175] A. Lewis and A. Challinor, Phys. Rept. **429**, 1 (2006).

[176] A. Einstein, Science **84**, 506 (1936).

[177] R. Jrgen, T. Sauer and J. Stachel, Science **275**, 184 (1997).

[178] O. Chwolson, Astronomische Nachrichten **221**, 329 (1924).

[179] F. Zwicky, Astrophys. J. **86**, 217 (1937).

[180] S. Dye and S. Warren, in *Dark Galaxies and Lost Baryons*, Proceedings of the IAU Symposium 244, 25th-29th June 2007.

[181] M. Bartelmann and P. Schneider, Phys. Rept. **340**, 291 (2001).

[182] N. Kaiser, Astrophys. J. **498**, 26 (1998).

[183] W. Hu, Phys. Rev. D **62**, 043007-1 (2000).

[184] F. Bernardeau, Astron. Astrophys. **338**, 767 (1998).

[185] L. V. van Waerbeke, F. Bernardeau and K. Benabed, Astrophys. J. **540**, 14 (2000).

[186] M. Takada, E. Komatsu and T. Futamase, Astrophys. J. **533**, L83 (2000).

[187] M. Takada, Astrophys. J. **558**, 29 (2001).

[188] B. Jain, U. Seljak and S. D. M. White, Astrophys. J. **530**, 547 (2000).

[189] C. M. Hirata and U. Seljak, Phys. Rev. D **67**, 043001 (2003).

[190] A. Challinor and G. Chon, Phys. Rev. D **66**, 127301 (2002).

[191] A. Lewis, Phys. Rev. D **71**, 083008 (2005).

[192] A. Challinor and A. Lewis, Phys. Rev. D **71**, 103010 (2005).

[193] S. Cole & G. Efstathiou, Mon. Not. R. Astron. Soc. **239**, 195 (1989).

[194] E. V. Linder, Mon. Not. R. Astron. Soc. **243**, 353L (1990).

[195] E. V. Linder, Mon. Not. R. Astron. Soc. **243**, 362L (1990).

[196] L. Cayon, E. Martinez-Gonzalez, and J. L. Sanz, Astrophys. J. **403**, 471 (1993).

[197] L. Cayon, E. Martinez-Gonzalez, J. L. Sanz, Astrophys. J. **413**, 10 (1993).

[198] U. Seljak, Astrophys. J. **463**, 1 (1996).

[199] R. B. Metcalf & J. Silk, Astrophys. J. **489**, 1 (1997).

[200] M. Zaldarriaga and U. Seljak, Phys. Rev. D **58**, 023003 (1998).

[201] A. Lewis, A. Challinor and N. Turok, Phys. Rev. D **65**, 023505 (2002).

[202] M. Kesden, A. Cooray and M. Kamionkowski, Phys. Rev. Lett. **89**, 011304 (2002).

[203] L. Knox and Y. S. Song, Phys. Rev. Lett. **89**, 011303 (2002).

[204] M. Kesden, A. Cooray, and M. Kamionkowski, Phys. Rev Lett. **89**, 011304 (2003).

[205] V. Acquaviva and C. Baccigalupi Phys. Rev. D **74**, 103510 (2006).

[206] W. Hu, D. Huterer and K. M. Smith Astrophys. J. **650**, L13 (2006).

[207] U. Seljak and M. Zaldarriaga, Phys. Rev. D **60**, 043504 (1999).

[208] D. M. Goldberg and D. N. Spergel, Phys. Rev. D **59**, 103002 (1999).

[209] W. Hu, Phys. Rev. D **65**, 023003 (2002).

[210] F. Giovi, C. Baccigalupi and F. Perrotta, Phys. Rev. D **68**, 123002 (2003).

[211] B. Gold, Phys. Rev. D **71**, 063522 (2005).

[212] R. Stompor and G. Efstathiou, Mon. Not. R. Astron. Soc. **302**, 735 (1999).

[213] W. H. Press & P. Schechter, Astrophys. J. **187**, 425 (1974).

[214] C. Lacey & S. Cole, Mon. Not. R. Astron. Soc. **262**, 627 (1993).

[215] F. Zwicky, Helvetica Physica Acta **6**, 110 (1933). An English translation should appear in Gen. Relativ. Gravit. in 2008.

[216] S. Smith, Astrophys. J. **83**, 23 (1936).

[217] H. W. Babcock, Lick Obs. Bull. **19**, 41 (1939).

[218] J. P. Ostriker and P. J. E. Peebles, Astrophys. J. **186**, 467 (1973).

[219] J. Lesgourgues and S. Pastor, Phys. Rept. **429**, 307 (2006).

[220] S. Tremaine and J. E. Gunn, Phys. Rev. Lett. **42**, 407 (1979). J. J. Dalcanton and C. J. Hogan, Astrophys. J. **561**, 35 (2001).

[221] G. Jungman, M. Kamionkowski and K. Griest, Phys. Rept. **267**, 195 (1996).

[222] L. Bergstrom, Rept. Prog. Phys. **63**, 793 (2000).

[223] G. Bertone, D. Hooper and J. Silk, Phys. Rept. **405**, 279 (2005).

[224] For reviews, see, e.g., M. S. Turner, Phys. Rept. **197**, 67 (1990). G. G. Raffelt, Phys. Rept. **198**, 1 (1990). G. G. Raffelt, *Stars as Laboratories for Fundamental Physics* (University of Chicago Press, Chicago, 1996); L. J. Rosenberg and K. A. van Bibber, Phys. Rept. **325**, 1 (2000).

[225] J. R. Ellis, J. S. Hagelin, D. V. Nanopoulos, K. A. Olive and M. Srednicki, Nucl. Phys. B **238**, 453 (1984). K. Griest, M. Kamionkowski and M. S. Turner, Phys. Rev. D **41**, 3565 (1990). K. A. Olive and M. Srednicki, Phys. Lett. B **230**, 78 (1989). K. A. Olive and M. Srednicki, Nucl. Phys. B **355**, 208 (1991).

[226] M. Kamionkowski, arXiv:0706.2986 [astro-ph]

[227] E. Bertschinger, Annu. Rev. Astron. Astrophys. **36**, 599 (1998).

[228] M. Davis, G. Efstathiou, C. S. Frenk, and S. D. M. White, Astrophys. J. **292**, 371 (1985).

[229] N. Y. Gnedin and X. Fan, Astrophys. J. **648**, 1 (2006).

[230] M. J. Berger and B. Collela, J. Comp. Phys. **82**, 64 (1989).

[231] A. V. Kravtsov, A. A. Klypin, and A. M. Khokhlov, Astrophys. J. Suppl. **111**, 73 (1997).

[232] M. L. Norman and G. L. Bryan, in **Numerical Astrophysics**, edited by S. M. Miyama, K. Tomisaka, and T. Hanawa (Kluwer, Boston, 1999), 19.

[233] J. Barnes and P. Hut, Nature **324**, 446-449 (1986).

[234] W. H. Zurek, P. J. Quinn, J. K. Salmon, and M. S. Warren, Astrophys. J. **431**, 559 (1994).

[235] P. Bode, J. P. Ostriker, and G. Xu, Astrophys. J. Suppl. **128**, 561 (2000).

[236] V. Springel *et al.*, Nature **435**, 629 (2005).

[237] V. Springel, C. S. Frenk, and S. D. M. White, Nature **1137**, 440 (2006).

[238] J. M. Colberg *et al.*, Mon. Not. R. Astron. Soc. **319**, 209 (2000).

[239] A. E. Evrard *et al.*, Astrophys. J. **573**, 7 (2002).

[240] J. Wambsganss, P. Bode & J. P. Ostriker, Astrophys. J. Lett. **606**, L93 (2004).

[241] V. Springel, N. Yoshida & S. D. M. White, New Astronomy **6**, 79 (2001).

[242] G. Xu, Astrophys. J. Suppl. **98**, 355 (1995).

[243] J. Barnes & P. Hut, Nature **324**, 446 (1986).

[244] R. W. Hockney & J. W. Eastwood, New York: McGraw-Hill, (1981).

[245] M. Colless *et al.*, Mon. Not. R. Astron. Soc. **328**, 1039 (2001).

[246] S. D. M. White *Formation and evolution of galaxies: Les houches lectures*, in R. Schaefer, J. Silk, M. Spiro, & J. Zinn-Justin (eds.) *Cosmology and Large-Scale Structure*, Dordrecht: Elsevier, (1996).

[247] U. Seljak & M. Zaldarriaga, Astrophys. J. **469**, 437 (1996).

[248] Ya. B. Zel'dovich, Astron. Astrophys. **5**, 84 (1970).

[249] M. J. Duncan, H. F. Levison, & M. H. Lee, Astron. J. **116**, 2067 (1998).

[250] V. Springel, S. D. M. White, G. Tormen & G. Kauffmann, Mon. Not. R. Astron. Soc. bf 328, 726 (2001).

[251] G. Kauffmann, & M. Haehnelt, Mon. Not. R. Astron. Soc. **311**, 576 (2000).

[252] M. J. Geller & J. P. Huchra, Science **246**, 897 (1989).

[253] J. R. I. Gott *et al.*, Astrophys. J. **624**, 463 (2005).

[254] W. Hu and T. Okamoto, Phys. Rev. D **69**, 043004 (2004).

[255] M. Kaplinghat, L. Knox and Y. S. Song, Phys. Rev. Lett. **91**, 241301 (2003).

[256] J. Lesgourgues *et al.*, Phys. Rev. D **73**, 045021 (2006).

[257] The Virgo Consortium, R.E. Smith et al., Mon. Not. Roy. Astron. Soc. **341**, 1311 (2003).

[258] M. Zaldarriaga and U. Seljak, Phys. Rev. D **59**, 123507 (1999).

[259] W. Hu, Astrophys. J. **557**, L79 (2001).

[260] C. M. Hirata and U. Seljak, Phys. Rev. D **68**, 083002 (2003).

[261] C. Shapiro and A. Cooray, JCAP **0603**, 007 (2006).

[262] K. M. Gorski, Astrophys. J. **622**, 759 (2005).